

DESIGN, CONTROL, MODELING, AND GAIT ANALYSIS IN MINIATURE FOLDABLE ROBOTICS

A THESIS SUBMITTED TO
THE GRADUATE SCHOOL OF ENGINEERING AND SCIENCE
OF BILKENT UNIVERSITY
IN PARTIAL FULFILLMENT OF THE REQUIREMENTS FOR
THE DEGREE OF
MASTER OF SCIENCE
IN
MECHANICAL ENGINEERING

By
Mohammad Askari
September 2018

DESIGN, CONTROL, MODELING, AND GAIT ANALYSIS IN
MINIATURE FOLDABLE ROBOTICS

By Mohammad Askari

September 2018

We certify that we have read this thesis and that in our opinion it is fully adequate,
in scope and in quality, as a thesis for the degree of Master of Science.

Onur Özcan(Advisor)

Melih Çakmakcı

Mustafa Mert Ankaralı

Approved for the Graduate School of Engineering and Science:

Ezhan Karaşan
Director of the Graduate School

ABSTRACT

DESIGN, CONTROL, MODELING, AND GAIT ANALYSIS IN MINIATURE FOLDABLE ROBOTICS

Mohammad Askari

M.S. in Mechanical Engineering

Advisor: Onur Özcan

September 2018

Miniature or micro robotic platforms are perfect candidates for accomplishing tasks such as inspection, surveillance, and hazardous environment exploration where conventional macro robots fail to serve. Such applications require these robots to potentially traverse uneven terrain, implying legged locomotion to be suitable for their design. However, despite the recent advances in the nascent field of miniature robotics, the design and capabilities of these robots are very limited as roboticists favor legged morphologies with low degrees of freedom. This limits small robots to work with a single gait set during the design phase, as opposed to legged creatures which benefit from efficient gait modification during locomotion. MinIAQ, a 23 g origami-inspired miniature foldable quadruped with individually actuated legs, is designed to address such limitations. The design of the robot is unique in which a high structural integrity is achieved by transforming a single flexible thin sheet into a rigid mechanical system through folding. MinIAQ's design novelties help modulate and extend the design standards of origami robots.

The actuation independency of MinIAQ enables gait modification and exhibits maneuvering capabilities which is another novel quality for a robot at this scale. The design of the compliant four-bar legs is optimized for better foot trajectory in a newer version of the robot, MinIAQ-II, through dimensional synthesis of mechanisms. The resulting robot demonstrates significant improvements over its predecessor. For characterization and synchronization of the motors, custom encoders are designed to estimate speed and phase of each leg. Accordingly, a closed-loop feedback control algorithm is applied to follow an envisioned gait pattern. Towards understanding these gaits in robots with passive closed-chain legs, a comprehensive mathematical model is developed to describe the 6-DOF rigid body dynamics of MinIAQ. The proposed dynamics employs a nonlinear

viscoelastic spring-damper model to estimate the feet-ground interactions. An interactive GUI is developed based on the model in MATLAB to simultaneously visualize the effects of design parameters on performance. 3D simulation results closely match with the experiments and effectively predict locomotion trends on flat terrain. Since there is no control on foot placement in such underactuated robots, the model has given an insight into analyzing how close the actual locomotion is to the envisioned gait. This suggests that a comprehensive locomotion study with the model can lead to optimizing the gait and improve performance of miniature legged robots.

Keywords: miniature robotics, origami-inspired robotics, foldable robotics, actuation mechanism optimization, dynamics simulation, quadruped gait analysis.

ÖZET

KATLANABİLİR MİNYATÜR ROBOTLARDA TASARIM, KONTROL, MODELLEME VE ADIMLAMA ANALİZİ

Mohammad Askari

Makine Mühendisliği, Yüksek Lisans

Tez Danışmanı: Onur Özcan

Eylül 2018

Minyatür ya da mikro boyuttaki robotlar, geleneksel büyük robotların başarmakta zorlandığı denetleme, gözetleme ve tehlikeli ortamların keşfedilmesi gibi uygulamalar için çok uygun adaylardır. Bu tarz uygulamalar robotların düz olmayan yüzeylerde hareket etmesini gerektirir, dolayısıyla robot tasarımının bacaklı hareket için yapılması gerekir. Ancak, kısmen bakir olan minyatür robotik alanındaki güncel gelişmelere rağmen, robotik araştırmacılarının düşük hareket dereceli bacak yapılarını tercih etmeleri sebebiyle minyatür robotların tasarım ve yetenekleri oldukça sınırlı kalmıştır. Düşük hareket dereceli bacaklı minyatür robotlar, adımlamalarını hareket esnasında etkin bir şekilde değiştirebilen bacaklı canlıların aksine, tasarım aşamasında ayarlanan sabit bir adımlama stratejisine sahiptirler. Bu tezin konusu olan 23 g ağırlığındaki origamiden esinlenilmiş tekniklerle üretilen minyatür katlanabilir robot MinIAQ, bu sınırlamayı aşabilmek adına her bacağın birer eyleyici ile ayrı ayrı sürüldüğü bir yapıya sahiptir. Robot, tek bir ince ve esnek tabakanın kesilip katlanarak yüksek yapısal sağlamlığa sahip bir mekanik sisteme dönüştüğü, özgün bir tasarıma sahiptir. MinIAQ'ın tasarımında kullanılan özgün stratejiler, literatürdeki katlanabilir robotların tasarım standartlarını çoğaltmak ve geliştirmek için, başka robotlara da uygulanabilir.

MinIAQ'ın bacaklarının her birinin ayrı motorlarla sürülüyor olması bu boyuttaki robotlarda olmayan özgün adımlama stratejisi değişimlerini ve manevra kabiliyetini beraberinde getirir. Robotun hareket mekanizmasını oluşturan esnek dört çubuk mekanizması boyutsal sentez teknikleri kullanılarak optimize edilmiş ve ayak yörüngesinin daha iyi olduğu MinIAQ-II versiyonunu ortaya çıkarmıştır. Ortaya çıkan yeni versiyon robotun hareket kabiliyetlerinde, ilk versiyona kıyasla

oldukça yüksek miktarda artış gözlenmiştir. Motorların karakterizasyonu ve senkronizasyonu için, laboratuvarında üretilen kendi tasarımımız olan optik kodlayıcı tasarlanmış ve bacakların hız ve birbirleri arasındaki faz farkı tahminleri için bu kodlayıcılar kullanılmıştır. Bu aşamadan sonra, kapalı döngü denetim algoritması ile robotun belli bir adımlama stratejisi ile yürümesi sağlanmıştır. Adımlama stratejisinin pasif eklemli kapalı zincir bacak mekanizmasına sahip robotun hareketine olan etkisinin incelenmesi için robotun altı serbestlik derecesine sahip gövde dinamikleri kapsamlı bir şekilde modellenmiştir. Dinamik model, ayakların yerle etkileşimlerini doğrusal olmayan viskoelastik yay ve sönümlendirici şeklinde modeller ve ayaklara uygulanan kuvvetleri tahmin eder. MATLAB’da geliştirilen bu modele, tasarım ve operasyon parametrelerinin hareket üzerindeki etkilerini görselleştirebilmek ve parametreleri değiştirebilmek için etkileşimli bir kullanıcı arayüzü eklenmiştir. Üç boyutlu simülasyon sonuçları deney sonuçları ile yakın bir şekilde örtüşmekte ve robotun düz yüzey üzerindeki hareketini tahmin edebilmektedir. Tezde bahsedilen ve bunlara benzer diğer minyatür robotlarda ayak yerleştirme sensörleri ve adımlama denetleyicileri olmadığından, geliştirilen model istenilen adımlama stratejisi ile gerçekleşen adımlama arasındaki farkları ortaya koymuştur. Bu model kullanılarak yapılacak detaylı bir adımlama analizi bacaklı minyatür robotlarda adımlama optimizasyonu ve genel performans iyileştirmeleri yapabilmemizi sağlayacaktır.

Anahtar sözcükler: minyatür robotlar, origamiden esinlenilmiş robot üretimi, katlanabilir robotlar, eyleyici mekanizma optimizasyonu, dinamik simülasyon, dört bacaklı adımlama analizi.

Acknowledgement

I would like to take this opportunity and express my sincere appreciation to every individual who contributed in some way to the work presented herein. First and foremost, I thank my academic adviser, Professor Onur Özcan, for giving me the opportunity to do research in my primary field of interest. His vision, sincerity, and never ending encouragement have been a source of inspiration to me throughout these years. I am extremely grateful for his patience and belief in my work, giving me intellectual freedom to steer my research towards the subjects I liked the most. He has not only been a great mentor to me, but also a friend with his kind attitude and endless sense of humor. Working under his supervision was a great privilege and honor to me.

I am also thankful to the departmental staff, especially Dr. Şakir Baytaroğlu and Şakir Duman, who deserve credit for their assistance in establishing and maintaining our lab as well as offering immediate support for manufacturing related tasks.

Every result presented in this thesis could not be accomplished without the help of my fellow labmates. Above all, I would like to extend my deepest gratitude to my dear friend Cem Karakadioğlu whose help was invaluable with in and off laboratory tasks. Being the first two members of the Miniature Robotics Research Group, every tiring task of setting up and tuning devices, investigating optimal manufacturing recipes, and preparing the ground and foundation for future work was made enjoyable with his ability to put complex ideas into simple solutions. I was also fortunate to have the chance to work alongside Nima Mahkam, Didem Fatma Demir, Levent Dilaveroğlu, Tamer Taşkiran, Ahmet Furkan Güç, Cem Aygül, Mert Ali İhsan Kalm, and Furkan Ayhan. I am grateful for the memories we share together and I wish every one of you the best of luck in your brilliant and inspiring careers. I am certain that with your collaboration, you will extend our work in the best possible manner and explore new avenues of research to achieve far more than we ever could do alone.

I am forever indebted to my best friend in life, Aminreza Shiri, whom I consider as family. Thank you for shining light and giving meaning to my life that no matter how dark and lonely the world around us got, you made living abroad feel like home. This long journey would have not been possible without your presence, and I dedicate this milestone to you.

Last but not least, my deepest and most heartfelt thanks goes to my family and friends. Words can not express how grateful I am to my parents, sister, brother-in-law, and my beloved newborn niece. I truly missed every one of you over these years and I am very thankful to God for having you all in my life. Thank you for your love, support, caring, understanding, and for enduring my absence. Your prayers and belief in me were what sustained me thus far.

Finally, I would like to acknowledge the Scientific and Technological Research Council of Turkey, TÜBİTAK, for financially supporting this research under Grant No. 116E177.

Contents

- 1 Introduction** **1**
 - 1.1 Motivation 1
 - 1.2 Research Aims and Objectives 2
 - 1.3 Structure of the Thesis 3

- 2 Design and Fabrication** **5**
 - 2.1 Miniature Foldable Robotics Literature 5
 - 2.2 Design of MinIAQ-I 7
 - 2.2.1 Material Selection 8
 - 2.2.2 Actuation Mechanism Design 9
 - 2.2.3 Rigid Frame Design 11
 - 2.2.4 Circuitry and PCB Design 15
 - 2.3 Fabrication and Assembly 16
 - 2.3.1 PCB Fabrication 16

2.3.2	Robot Fabrication and Assembly	17
2.4	Design of MinIAQ-II	19
2.4.1	Actuation Mechanism Optimization	21
2.4.2	Foldable Design of Fixed-Angle Joints	28
3	Control and Operation	30
3.1	Control Problem Definition	30
3.2	Control Strategy	31
3.2.1	Custom Encoder Design Evolution	31
3.2.2	Signal Processing	34
3.2.3	Controller Design	36
3.2.4	Controller Performance	38
3.3	Performance of MinIAQ	41
3.3.1	Basic Motion Simulation	41
3.3.2	Operation and Experiments	42
4	Dynamic Modeling	45
4.1	Robotics Modeling Literature	45
4.2	Assumptions	47
4.3	Kinematic Analysis of a Leg	49

4.3.1	Position Analysis	49
4.3.2	Velocity and Acceleration Analyses	55
4.4	Dynamic Analysis	57
4.4.1	Translational Equations of Motion	59
4.4.2	Rotational Equations of Motion	60
4.4.3	Position and Orientation Equations	61
4.5	Estimation of Ground Reaction Forces	64
4.5.1	Contact Mechanics Literature	64
4.5.2	Foot Contact Determination	66
4.5.3	Impact Force Model	67
4.5.4	Pseudo-Coulomb Friction Model	69
4.5.5	Net Force and Moment Calculation	70
4.6	Solving the System of Stiff ODEs	72
5	Model Verification	75
5.1	Simulation GUI and Experimentation	75
5.2	Verification of Trot Gait Locomotion	77
5.2.1	Roll, Pitch, and COG Trajectory Verification	77
5.2.2	Effect of Imbalance Verification	81
5.3	Verification of In-Place Turning	83

5.3.1 COG Tracking and Turning Speed Verification 83

6 Gait Analysis **86**

6.1 The Gait Coordination Problem 86

6.2 Envisioned Gait Performance 87

6.3 Quadrupedal Gaits Comparison 91

7 Conclusion and Future Work **94**

Bibliography **107**

A Geometrical Considerations in Foldable Mechanism Design **108**

A.1 Ideal Mechanism to Foldable Leg Design 110

A.2 Mechanism Modeling from a Foldable Leg 111

List of Figures

2.1	MinIAQ-I: The original foldable miniature quadruped robot. . . .	8
2.2	Various colors of 100 μm thick A4-sized PET sheets used as structural material of MinIAQ.	9
2.3	Static trajectory of the four-bar mechanism with a detail view of the fundamental linkage and joint design in foldable robots. Inset shows hollow triangular beams with flexure joints.	10
2.4	(a) Unfolded crease pattern of two parallel T-shaped folds (green) with embedded U-shaped fasteners (red). The black dashed lines represent the folding lines. (b) Folded structure of T-folds with their U-shaped extension tabs fastened into a common slot in between. (c) Side view of the folded structure showing how the fasteners pass underneath the T-folds and lock into the slot from below.	12
2.5	Sectional view of MinIAQ's main frame showing T-folds (green) with motor and sensor housings, a pair of U-shaped fasteners for locking T-folds (red), U-shaped fasteners (blue) and tight fit extension tab-and-slots (yellow) for top cover enclosure, and the bottom hatch door opening (magenta) for replacement of the battery (brown).	13

2.6	(a) Unfolded structure of two T-folds with motor and sensor housings. The black dashed lines represent the folding lines. (b) Folded structure of T-folds with motor and sensor in place.	14
2.7	Autodesk EAGLE drawing of the PCBs used in MinIAQ: (a) Inner flexible PCB with sensor connections, and power regulation. (b) Main controller PCB with microcontroller and actuator drivers. Red lines show traces on the top layer and blue lines show traces on the bottom layer. The labeled numbers indicate the placement of components on board, that are described in text.	15
2.8	(a) PCB without any components soldered. (b) PCB with the motor drivers, IR reflectance sensors, on-off switch, and FFC/FPC connector soldered. (c) Final form of MinIAQ's circuit board after soldering all components and cutting it into inner flexible PCB and outer main controller PCB.	17
2.9	The 2D unfolded technical drawing file used for laser cutting where dashed red lines represent the folding edges and continuous blue lines show full cuts. The labeled parts are explained in detail in the text.	18
2.10	MinIAQ-II: The latest version of foldable miniature quadruped robot, with improved leg design.	20
2.11	A schematic of the generalized modified four-bar leg mechanism considered in the design of MinIAQ-II locomotion. The red dashed lines indicate the nodal design constraints and the blue dashed curve represents the target trajectory used in the optimization algorithm.	22
2.12	(a) Non-optimized mechanism of MinIAQ-I. (b) Leg design of MinIAQ-II with optimized trajectory.	26

2.13	Variations of estimated flexure joint bending angles in MinIAQ–I and MinIAQ–II for (a) joint <i>A</i> and (b) joint <i>C</i>	27
2.14	A schematic representation of the folding procedure for the new leg design. The knee shaped triangular beam link consists of two triangular beams and a fixed-angle joint that is locked in place with the help of the inclined fastener.	28
3.1	(a) Single black band cam shaft encoder. (b) 3D multi-stripe cam shaft encoder. (c) Multi-stripe cam shaft encoder with one thinner black band.	32
3.2	A 3D encoder analog output signal with 28 sample points per cycle, detected by threshold crossing method, for the controller input.	34
3.3	MinIAQ’s closed loop control algorithm block diagram.	36
3.4	Time response of two motors to the controller.	38
3.5	Absolute value of phase offset of one motor with respect to another.	39
3.6	Synchronization of two motor signals with respect to each other with zero phase difference, corresponding to 180° phase offset on actual legs.	40
3.7	Snapshots of the controlled trot gait synchronization of MinIAQ–I over one period at 3 Hz running frequency.	40
3.8	Front leg trajectory of MinIAQ–I for an ideal trot gait simulation.	41
3.9	Forward velocity of MinIAQ–I for a 3 Hz trot gait simulation	42
3.10	Comparison between front legs stride trajectories of MinIAQ–II (top) and MinIAQ (bottom), in an ideal 3 Hz trot gait simulation.	42

3.11 Variations of pitch and roll angles estimates from 3 Hz trot gait simulation for both versions of MinIAQ. The snapshots on the right show the maximum recorded pitch and roll from actual tests. 44

3.12 Snapshots of MinIAQ-II’s improved maneuverability during a zero-radius in-position turning test at 3 Hz stride frequency. . . . 44

4.1 (a) A representation of the actual folded leg shape of MinIAQ-II. (b) A schematic diagram of MinIAQ’s generalized four-bar leg mechanism with geometrical consideration for the coupler link. . . 50

4.2 Trajectory of the foot with and without geometrical considerations for the knee-shaped link, shown by black solid and red dashed lines, respectively, for (a) MinIAQ-I and (b) MinIAQ-II. 51

4.3 A schematic representation of the 3D model of MinIAQ-II, showing the body-fixed reference frame and a position vector to the tip of the right foreleg (leg 1). This is in fact the leg whose kinematic analysis is presented in this section. 54

4.4 A schematic representation of the **B**ody-attached and the **I**nertial (global or world) reference frames used in deriving the dynamic equations. Unless otherwise stated, subscripts B and I are used throughout the text to emphasize the variables being measured with respect to these coordinate frames. The vectors shown are described in detail throughout this section. 58

4.5 A schematic of the position \mathbf{P}_I and orientation $\mathbf{\Gamma}$ definitions: roll (ϕ), pitch (θ), and yaw (ψ) axes on the robot. The rotational speed of the body is also represented by (p, q, r) , as discussed in the previous section. 62

4.6	Close-up schematic of the interpenetration between a foot and the ground during contact. Analysis of the impact must be done in the inertial axis, leading to the estimation of the normal force along Z_I , and analysis of the friction is done in $X_I Y_I$ plane.	67
4.7	(a) Variation of the impact force model with nonlinear exponent and penetration depth and (b) the displacement based damping.	69
4.8	Pseudo-Coulomb dry friction model.	70
5.1	An interactive GUI designed for simulating MinIAQ in MATLAB with four control panel toolbars. The 3D view figure control widget is used to interact with the simulation window and modify plot settings. The initial states and dynamic parameters panel is used to select the robot version, adjust gaits and motor frequency, modify the initial state or dynamic variables, and to run, pause or terminate the simulation. The results panel prints the dynamic properties of the system as well as the solution to the current state variables at every successful iteration in time. Finally, the export toolbar enables video recording, screen capturing, and saving the solution or loading an existing model for post processing.	76
5.2	Trot gait roll angle verification for MinIAQ-I at 3 Hz.	78
5.3	Trot gait roll angle verification for MinIAQ-II at 2.5 Hz.	78
5.4	Trot gait pitch angle verification for MinIAQ-I at 3 Hz.	79
5.5	Trot gait pitch angle verification for MinIAQ-II at 2.5 Hz.	80
5.6	Trot gait position trajectory verification for MinIAQ-I at 3 Hz.	81
5.7	Trot gait position trajectory verification for MinIAQ-II at 2.5 Hz.	81
5.8	A top view schematic of the shift in the COG of MinIAQ-I.	82

5.9	Trot gait roll angle for imbalanced MinIAQ-I at 3 Hz.	82
5.10	Trot gait pitch angle for imbalanced MinIAQ-I at 3 Hz.	83
5.11	Trot gait position trajectory for imbalanced MinIAQ-I at 3 Hz. . .	83
5.12	In-place turning trajectory verification for MinIAQ-I at 2.5 Hz. . .	84
5.13	In-place turning trajectory verification for MinIAQ-II at 2.5 Hz. .	84
5.14	Yaw angle variation during in-place turning for MinIAQ-I at 2.5 Hz.	85
5.15	Yaw angle variation during in-place turning for MinIAQ-II at 2.5 Hz.	85
6.1	A schematic showing the convention used in labeling the legs. <i>R</i> , <i>L</i> , <i>F</i> , and <i>H</i> are abbreviations for Right, Left, Foreleg and Hind leg, respectively.	88
6.2	A complete trot gait diagram for MinIAQ-II, for a simulation of five seconds at 2.5 Hz, equivalent to 12.5 stride cycles. Since the actual gait is symmetric and periodic in time, representation of a single cycle would be enough.	88
6.3	A single cycle trot gait diagram for MinIAQ-II, simulated at a motor speed of 2.5 Hz.	89
6.4	A single cycle turning gait diagram for MinIAQ-II, simulated at a motor speed of 2.5 Hz.	90
6.5	Trot gait simulation samples. Data shown is the center of gravity of the robot recorded from a top view at (a) 2.5 Hz and (b) 11.5 Hz motor speeds.	91
6.6	MinIAQ-II's simulated locomotion performance on flat terrain for different intended quadrupedal gaits at different motor speeds. . .	92

A.1 (a) Unfolded MinIAQ–II compliant mechanism where link lengths are measured between the midpoints of the flexure joints (b) Assembled leg. 109

A.2 Schematic diagram of a fully assembled leg with detail analysis of the non-straight knee-shaped link geometry. $ABCD$ is the actual actuating four-bar. Point E , which is fixed to the coupler link CD (link 3), is the tip of the foot whose trajectory is optimized for proper walking. The knee-shaped link is not drawn to scale for better visualization. 109

List of Tables

4.1	Constant kinematic parameters for MinIAQ-I and MinIAQ-II. . .	51
4.2	Constant dynamic parameters used in simulation of MinIAQ for the impact and friction force models.	70
6.1	Motor Phases for Intended Quadrupedal Gaits of MinIAQ-II. . .	91

Chapter 1

Introduction

1.1 Motivation

With a past characterized by industrial revolution and a future pictured by an automation revolution, the proliferation of robotics in life is inevitable. Some may embrace the idea and go with the flow and some choose to stand against it, but personally, I would rather be the flow itself. That is to be one who has full understanding and control over how the world is changing, and not just be an observer.

From a robotics standpoint, attaining tasks in industrial environment which are inherently highly predictable, programmable, and require rigid interactions are significantly easier than attaining tasks in real world environment which require creativity, adaptation, and soft interactions. That is the reason an automotive assembly line is fully automated with precise robotic arms, and, yet, a robot feeding a baby cannot be found. Current technological limitations and design difficulties dictate roboticists to opt for designing target-specific robots rather than versatile robots. This specialization and unpredictability of the working environment requires robotic platforms to be highly flexible, modular, robust, easily programmable, safe to interact with, and yet remain very cost effective.

This has made research on miniature and micro robotics field very appealing as it is arguably easier to achieve many of these properties with small scale robots than it is with larger ones.

Applications such as inspection, surveillance, exploring hazardous environments, and search and rescue missions further promote utilization of miniature robots in life. Such working environments require these robots to potentially traverse uneven terrain, implying legged designs to be appropriate for their locomotion. Inspired by the locomotion capabilities of animals, miniature legged robots can additionally give better insight into study of efficient gaits used by small biological creatures.

1.2 Research Aims and Objectives

While conventional manufacturing methods for bulky and heavy components of large robots are well established, design and fabrication techniques practiced for miniature and micro robots are relatively limited. There is a need for significant advances in both optimization of existing methods as well as seeking alternative novel techniques for the fabrication of the components for the next generations of miniature robots. Furthermore, limited research has been conducted on gait modification of these robots due to lack of proper actuation sensing and power limitations in miniature scale. Robots with higher number of active degrees of freedom can enable gait adjustment but are often avoided in small scale systems to minimize cost and complexity. Study of locomotion in biological legged-creatures have proven that gait modification is crucial as gaits that are efficient in walking become extremely inefficient for running and vice versa. Animals modify their gaits with respect to their locomotion speeds or terrain characteristics, whereas robots, especially small ones, tend to work with a single gait set during the design phase. The main reason why robots do not modify gaits similar to animals is that it is not known exactly which gait is optimum under different scenarios. These are primarily the key issues that this research work aims to address.

This work primarily contributes to the fabrication methods for miniature robots by utilizing the less common foldable or origami-inspired technique. To exhibit the potential areas of research in this field, a unique complex foldable quadruped, MinIAQ, is designed. As opposed to most miniature robots that are made from multi-layer composite structures, MinIAQ is made of a single-layer flexible sheet. Yet, the final folded structure of the robot has very high structural integrity. With an aim to perform gait studies in miniature robots, MinIAQ is designed to have independent leg actuation. The four-bar compliant leg mechanism of the first version robot, MinIAQ-I, is optimized for better foot trajectory in MinIAQ-II. Each of the four legs is actuated by a separate DC motor and custom encoders are built to characterize the motors for use in gait synchronization control.

The foremost contribution of this thesis is the insight it gives into understanding how locomotion studies should be performed in the absence of foot placement control in small scale robots. Towards analyzing how an envisioned gait performs in an underactuated miniature robot, a 3D 6-DOF rigid body dynamic model is developed to predict the locomotion of MinIAQ. The proposed dynamic model employs nonlinear contact theories to estimate the ground reaction forces. The validity of the model is confirmed by observing good agreement between the simulation results and the existing experimental data. The resulting simulation interface predicts locomotion trends on flat terrain and can help visualize how close the actual motion is to the envisioned gait. It is believed that the presented model can be utilized to understand the underlying factors that can contribute to gait planning and optimizing locomotion in robots with lower degrees of freedom and lack of control on feet placement.

1.3 Structure of the Thesis

The work done in this thesis is organized as follows.

Chapter 2 guides through the origami-inspired design of MinIAQ, followed by detailed information on fabrication and assembly of the robot. MinIAQ's design

enhancements and certain guidelines in making the crease pattern of a foldable robot for high structural integrity are presented in depth. In addition to the design novelties, an optimization method is presented that can be employed for optimizing the design of compliant leg mechanisms, as used in MinIAQ-II.

Chapter 3 presents the control strategy and basic operation of MinIAQ-I and MinIAQ-II. The design of custom encoders for characterization of position and speed of the encoder-less motors is given. The strategy in synchronizing a desired gait in miniature robotics application is explained in detail.

Chapter 4 formulates a 3D 6-DOF rigid body dynamic model to describe the motion of MinIAQ. It is developed in a manner that can predict locomotion in an underactuated robot with passive closed-chain leg kinematics. The proposed model can help visualize how close a robot with these specifications can follow an envisioned input gait.

Chapter 5 explains how the dynamic model is verified. The existing experimental data for trot gait locomotion and in-place turning are extracted from actual test videos and are compared with the simulation results to verify the model's validity. It is observed that the simulations successfully predict the trends in locomotion on flat terrain and track 3D body movements.

Chapter 6 gives an insight into how this dynamic model can be used to identify the missing elements of a gait analysis in small scale robots. Comparison between the achieved gaits in MinIAQ and the corresponding ideal input gaits helps clarify the point. A variety of existing quadrupedal gaits are also simulated and analyzed over a wide range of motor speeds.

Chapter 2

Design and Fabrication

This chapter presents the evolution of **MinIAQ**, a **Miniature Independently Actuated-legged Quadruped**, explaining in detail the design, fabrication, and assembly of its body and electronics. MinIAQ is originally inspired by origami art, the traditional Japanese art of subsequent folding of a 2D sheet into a 3D functional structure. Each leg of the robot is actuated separately with an aim to perform gait studies in miniature robots. Discussion on control, operation, modeling, and gait analysis is given in the following chapters. The content of this chapter is published in [1] and [2].

2.1 Miniature Foldable Robotics Literature

Miniature robotics offer solutions to overcome impediments in conventional macro robotic systems. Constraints such as low cost, rapid and batch fabrication, customizability, and modularity make small scale robots potential candidates for many applications. The agility, silent operation, high maneuverability, and lightweight structures of miniature robots make them capable of performing tasks such as inspection, surveillance, exploration, and search and rescue missions in confined spaces or hazardous environments [3]. Such robots have also recently

become indispensable part of research, education, and swarm studies due to their inexpensive yet rapid prototyping [4]. However, the main challenges in miniature robotics lie in the manufacturing, actuation and control at small scale. It is thus very critical to find solutions for the limitations in design, locomotion, traction, and fatigue failure of flexure joints in such robots.

One of the original solutions in fabrication of small scale robots is the Smart Composite Manufacturing (SCM) method developed in UC Berkeley [5], which has yielded many successful early miniature robots such as DASH [6], HAMR [7], and family of RoACH robots [8,9]. In later years, some other fabrication methods are born out of SCM, such as PC-MEMS [10] and pop-up MEMS [11]. Some other techniques include, but are not limited to, Inverse-Flow Injection (IFI) and Dip-Cure-Repeat (DCR) [12], photolithography [13], and 3D printing as in [14].

Kirigami, a subset of origami involving out-of-plane cuts [15], inspired developing a new planar fabrication process for micro-robotic systems which is often referred to as printable, foldable, or print-and-fold robotics [16]. In this context, the term printing corresponds to engraving cut and fold patterns on sheets by utilizing a laser cutter or even by patterning 2D printable layers using 3D printers [17]. Then, the final robot is obtained by successive folding over the crease pattern. One of the advantages of printable or foldable robotics is that all transmission, flexure joints, and customizations can be embedded into a single 2D design, which not only is cheap and time-saving, but also eases the fabrication, assembly, and future design enhancements. Following the early works reported in [18], this technology was first developed by researchers in Harvard University and MIT [16] and was later adapted by many researchers in designing their miniature grasping [19,20], flying [21], and worm type robots [22,23] as well as some enhanced legged versions [24–26]. The method was further developed in [27] by embedding circuitry into planar designs through shape-memory composite structures to enable self-folding of the robots. Despite the recent advancements in foldable robotics, it is not extensively utilized in engineering fields due to its limiting factors such as planar design constraints, material selection limitations, and relatively complex folding and assembly tasks involved.

There is still a need for improvement in both modulating and standardizing the primitive folding elements of origami-inspired robots to obtain high structural integrity and rigidity. There does not exist many examples of complex foldable structures and most of the works rely on rather simple designs [28]. Consequently, in design of MinIAQ it was aimed to show the capability of this fabrication method for making complex robots and set a paradigm for designing complicated foldable frameworks with higher structural integrity.

2.2 Design of MinIAQ–I

There are very few studies on miniature or micro robot locomotion and gait planning [14]. The main reason is the actuation challenge of these robots. Since most miniature scale actuators do not have absolute encoders, it is very hard to adjust and control gaits at this scale. Therefore, a certain locomotion and gait is often initially optimized and is mechanically locked into the robot’s mechanism design such as in [25]. While these robots function perfectly, they cannot change gait and thus cannot be used for gait studies in small scale. Due to the lack of gait studies for miniature robots, it is not known if modifying gait under certain environmental factors would improve the locomotion. As a result, MinIAQ is originally designed with independent leg actuation to answer this need.

MinIAQ is a quadruped foldable legged robot made from a single sheet of thin A4-sized PET film. The stiffening structures used in its platform and the overall unfolded design of the robot are quite unique, and thus can contribute to the design of better origami-inspired robots. Its legs are designed based on a simple four-bar locomotion mechanism that is embedded into its planar design and each leg is actuated separately by a small DC motor. This is different from most miniature robots where one or two actuators are shared between legs to provide easier synchronous leg motion. Despite higher power consumption and greater challenge in phase synchronization control at such small scale, this enables gait adjustment to achieve better maneuverability, perform in-place sharp turning, conduct locomotion studies, and have better control over robot’s overall motion.

The main reason in designing a robot with individually actuated legs is not to claim that it is better or easier to control than miniature robots with coupled actuation but to facilitate gait modification during locomotion. Even though MinIAQ itself is a quadruped, the robot can be modified to have ‘n’ legs, if ‘n’ of these individually actuated legs are put together on a single body or attached through a number of modules.

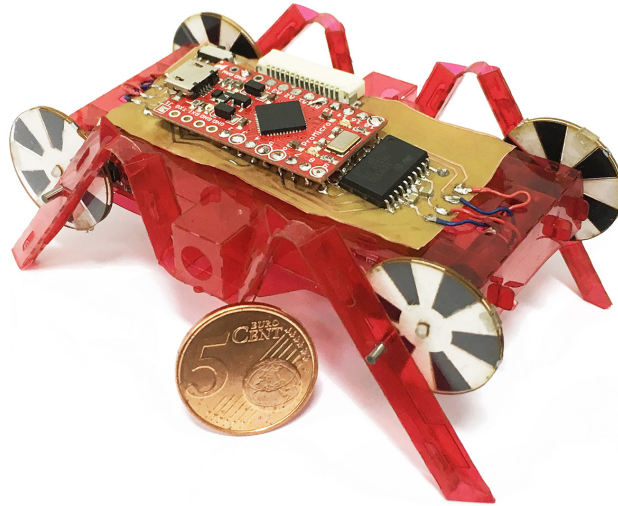


Figure 2.1: MinIAQ-I: The original foldable miniature quadruped robot.

The initial version of the robot (Figure 2.1) takes less than two hours to be cut and assembled and weighs about 23 g where 3.5 g is the weight of its body, 7.5 g is its motors and encoders, 5 g is its battery, and about 7 g is its on-board electronics and sensors. The robot is capable of running about 30 minutes on a single fully charged 150 mA h single cell LiPo battery. Further information on operation of the robot is given in Chapter 3.

2.2.1 Material Selection

In designing MinIAQ, the aim was to make an embedded single-piece crease pattern for ease of manufacturing. In order to select a proper material in terms of flexibility, rigidity, and joint durability, 100, 250 and 500 micrometer thick PET sheets were selected as possible candidates (Figure 2.2). During fabrication

of the robot, it was observed that the thinner sheets were easier to cut, fold and assemble. Despite the fact that rigidity increases with film thickness, it becomes harder to make folds and shape corners, especially by scaling down to smaller scale folds. In addition, the thicker sheets had lower joint performance since the joints made of thicker sheets would plastically deform and break much sooner than the thin sheets. Alternative structural materials such as Kapton[®] can also be used to achieve enhanced mechanical properties such as increased stiffness or higher joint cycle life.



Figure 2.2: Various colors of 100 μm thick A4-sized PET sheets used as structural material of MinIAQ.

2.2.2 Actuation Mechanism Design

Design of actuation mechanism and power transmission in miniature or micro robots is not as straightforward as it is in macro scale robotics. By scaling down, frictional losses become more dominant as the ratio of surface area, A , relative to volume, V , increases ($A \propto L^2$, $V \propto L^3$). Accordingly, utilizing revolute pin joints and other rotational components created by macro scale is not advisable at small scales as they become very inefficient. In miniature robotics, flexure joints are often preferred as deformation rather than pure sliding, as in pin joints, has comparably less frictional losses [29].

In MinIAQ, rigid triangular beams and compliant flexure joints are used as the primitive components of the four-bar actuation mechanism. Rigid links are achieved by folding the sheets and locking into triangular prism shape. In this configuration, the beam's rigidity is dependent on its length, width, thickness and Young's modulus of material used [30]. Flexure joints, which act as revolute pin joints in the four-bar compliant mechanism, allow one degree of freedom rotation between two rigid triangular links with the help of sheet flexibility. The inset view of Figure 2.3 clearly shows such foldable linkage structure. Even though flexure joints are very useful components for small scale compliant mechanisms, they often suffer from fatigue failure [31]. By optimizing the joint width, length, thickness, and maximum deflection angle, fatigue life cycle of the flexure joints can be increased further by distributing the load more uniformly and reducing the stress at the joints. For the early versions of MinIAQ, the design of flexure joints was not optimized and this was later investigated by another researcher in the lab.

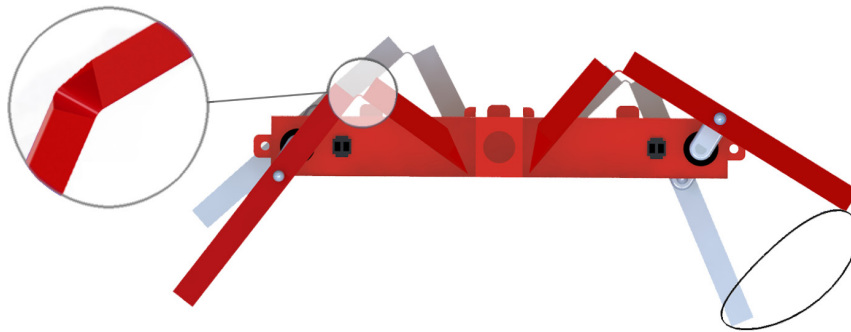


Figure 2.3: Static trajectory of the four-bar mechanism with a detail view of the fundamental linkage and joint design in foldable robots. Inset shows hollow triangular beams with flexure joints.

The first step towards a legged robot design and perhaps the foremost important stage is the design of its actuation mechanism. In foldable robotics context, it is quite challenging to integrate a mechanism into the design which has good locomotion trajectory while having simple unfolded form. The flexure joints in foldable designs have limited degree of rotation, meaning that the links should not be bent very large with respect to each other so as to prevent shear at the joints [32]. This issue further aggregates the challenge in mechanism selection.

For MinIAQ-I’s legs, a simple four-bar cam-driven mechanism was designed and synthesized by altering the dimension of the leg, position of the joints and radius of the cam (input crank link) in order to obtain an acceptable trajectory as shown in Figure 2.3. Note that apart from the input crank link which is made of a separate part to enable 360° rotation in plane, the rest of the linkage links incorporate the foldable rigid triangular beam with flexure joint structure. The selected four-bar is not optimal performance-wise; it has relatively poor trajectory and stride length for a legged robot. However, its simplicity was favored over complexity for the initial MinIAQ version due to ease of planar design and assembly. In the improved version of MinIAQ, a more optimal actuation mechanism is used, which is discussed in detail in Section 2.4 of this chapter.

2.2.3 Rigid Frame Design

This section presents the novel design of MinIAQ’s main frame with discussion on primitive folding elements that can be utilized in origami-inspired robots. These components can act as subsets of any complex structure. It is believed that MinIAQ sets a paradigm for designing more complicated foldable robotic platforms with high structural integrity and rigidity.

The high integrity of the frame and the leg linkages has an important role in increasing the payload capacity of a foldable robot. Due to having a thin flexible sheet as the base material, these primitive folding patterns are required to make the frame and linkages hold their shapes. As discussed earlier, the design of the legs are based on the combination of hollow triangular links and perforated flexure joint structures studied in the literature by [4, 24, 30, 33].

The fundamental stiffening element of the frame is achieved through a simple, yet, novel folding technique called “T-shaped folds” (as we named it). Sufficient number of T-folds, as shown by green color in Figures 2.4 to 2.6, can remarkably contribute to high structural integrity of a folded structure. The crease pattern of a T-fold consists of three equally spaced parallel lines on the main frame. When the three lines are folded 90° inwards, 180° outwards, and 90° inwards

consecutively, they form a T-shaped out of plane extension from the base surface. To lock the T-folds in place, gluing or stitching can be a solution, but they are practically hard to implement for small parts and tiny extensions. The better approach is to utilize tab-and-slot fasteners to tightly lock the folded parts into each other.

In MinIAQ’s frame design, the locking mechanism of T-folds consists of certain tabs that are placed on one face of the T-folds and lock into respective slots after folding. To firmly fix the position of a pair of T-folds and hold them in place, the tabs on each T-fold can be fastened into a single common slot placed in between them (see Figure 2.4(a)). The tip of a locking tab incorporates perforated sides that are bent into a U-shape to achieve proper locking after the tab is inserted through the slot (Figure 2.4(b)). Once T-folds are folded and locked, these fasteners prevent them from opening. Note that a total of three equally spaced fasteners are used for each T-fold on the main frame of MinIAQ, as shown by red color in Figures 2.4 and 2.5. By using such fasteners, T-fold assemblies can be completed in minutes without needing any extra effort or hand skill.

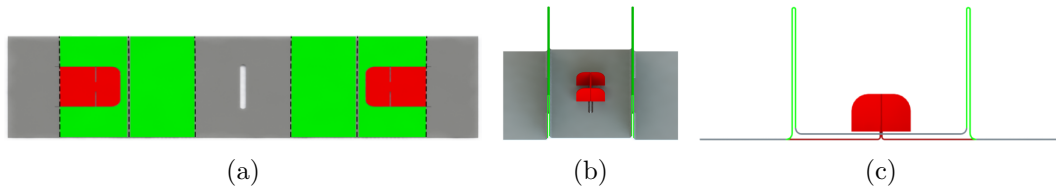


Figure 2.4: (a) Unfolded crease pattern of two parallel T-shaped folds (green) with embedded U-shaped fasteners (red). The black dashed lines represent the folding lines. (b) Folded structure of T-folds with their U-shaped extension tabs fastened into a common slot in between. (c) Side view of the folded structure showing how the fasteners pass underneath the T-folds and lock into the slot from below.

Extension tabs at the ends of T-folds (shown by yellow in Figure 2.5) are tightly fitted through slots in the front and rear frame enclosures. These tabs limit robot frame’s twisting under torsion and prevent unwanted dislocations. The friction between the tight-fit extension tab-and-slot has enough locking force to prevent sliding of T-fold or any undesired movement along the transverse plane.

To further improve the bending stiffness of the body, the T-folds located on the bottom surface of the main frame are locked into the enclosing top surface. This is done through embedding tabs on the upper side of the T-folds and carefully placing respective slots on the top cover which encloses the body. Once folded and fastened, buckling, transverse bending, and dislocation of T-folds within the body are prevented. The locking mechanisms can either be of U-shaped fastener type or the tight-fit extension tab-and-slot type, shown by blue and yellow colors in Figure 2.5, respectively. The sectional view of MinIAQ's body given below illustrates the aforementioned primitive folding elements in different colors.

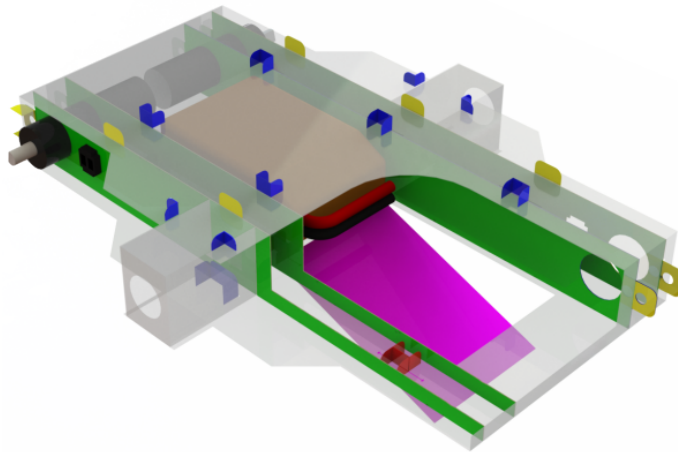


Figure 2.5: Sectional view of MinIAQ's main frame showing T-folds (green) with motor and sensor housings, a pair of U-shaped fasteners for locking T-folds (red), U-shaped fasteners (blue) and tight fit extension tab-and-slots (yellow) for top cover enclosure, and the bottom hatch door opening (magenta) for replacement of the battery (brown).

If T-folds are correctly utilized in conjunction with tight-fit tab-and-slots and U-fasteners, the T-folds become like I-beam structures. Accordingly, the main body frame enclosure becomes very rigid and does not easily bend, twist, or buckle under considerable loading. Therefore, by using 'n' number of T-folds within a structure, with proper locking mechanisms, the frame technically becomes a rigid body supported by 'n' number of I-beams.

Another challenging stage in the design of MinIAQ's body was to find a folded structure to tightly hold the DC motors and sensors in place within the frame. The rotational motion of the motors was transmitted to the legs with a cam

shaft made of a thicker sheet film. Note that since the cam shaft, i.e. the crank link of the four-bar, has to rotate 360° in plane, it is very hard and complex, if not impossible, to achieve this with an origami flexure joint structure. Thus, the cam shafts were made and assembled from separate sheets and pins. These elements on the MinIAQ are the only mechanical parts on the robot that have to be manufactured separately. The cam shafts also serve as elements used in control and synchronization of the robot legs via IR sensors which are explained in detail in Chapter 3.

While using separate external housings for motors or sensors could be a solution, in foldable robotics the aim is to avoid using multiple parts or materials as much as possible and restrain the design to a single uniform crease pattern. This was solved by using two pairs of parallel T-folds, one on each side of the main frame. Creating two inline tight circular openings through each pair enables firmly holding a DC motor inside the body. The IR sensor circuit board is inserted through the outer T-folds with a small opening made for its emitter and receiver (see Figure 2.6). This small rectangular sensor opening also helps holding the sensor in place by preventing it from sliding within the T-fold faces. Thus, due to their out-of-plane structure, T-folds are very suitable for making housings such that any type of motor or electrical component can be properly mounted onto the frame by a pair of parallel T-folds. Part of the large gap in between the inner T-folds is used for battery placement as can be seen in Figure 2.5. The battery can easily be accessed, removed for charging or replaced using the frame's bottom hatch door. The remaining space inside the body can potentially be used for any additional component to be added in the future versions.

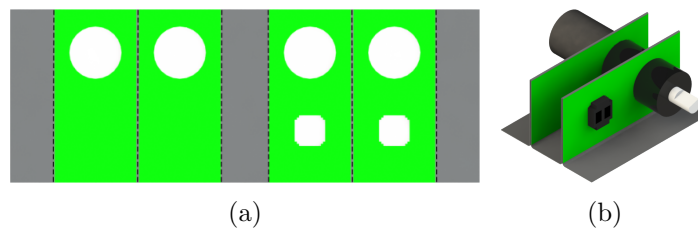


Figure 2.6: (a) Unfolded structure of two T-folds with motor and sensor housings. The black dashed lines represent the folding lines. (b) Folded structure of T-folds with motor and sensor in place.

2.2.4 Circuitry and PCB Design

With the intention of having independent leg actuation, MinIAQ consists of four very small and lightweight (approximately 1.25 g each) motors (Pololu, Sub-Micro Plastic Planetary Gearmotor). The major drawback of using these motors is the lack of any type of built-in encoders. For this reason, it is necessary to design feedback sensing for each motor to properly adjust the speed and position of each leg. Hence, small reflectance IR sensors are selected to house next to the motors to estimate speed and position through custom cam encoders with black and white stripes. An in-depth discussion on custom encoders design, feedback signal, and leg synchronization control is given in Chapter 3.

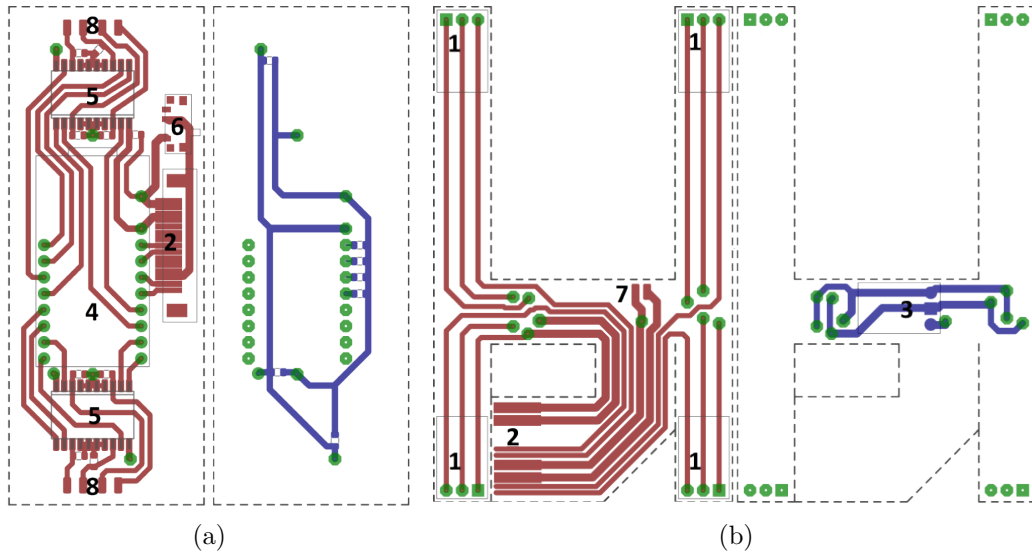


Figure 2.7: Autodesk EAGLE drawing of the PCBs used in MinIAQ: (a) Inner flexible PCB with sensor connections, and power regulation. (b) Main controller PCB with microcontroller and actuator drivers. Red lines show traces on the top layer and blue lines show traces on the bottom layer. The labeled numbers indicate the placement of components on board, that are described in text.

Since the motors and sensors are located towards the four corners of the body, a flexible PCB is designed that is placed inside the main frame and extends to the sensors. This inner flexible board (Figure 2.7(a)) powers every sensor and transfers the signals to the microcontroller on the main outer PCB (Figure 2.7(b)). To enable folding of the boards, they are made out of copper clad polyimide

flexible sheets (Dupont, Pyralux). The two sides of the inner flexible PCB, which contain a pair of sensors each (labeled as ‘1’ on Figure 2.7), are folded by 90° to accommodate sensor placement within the T-folds. Signal and power traces of the inner PCB are combined and bundled in a foldable extension that comes out of the top frame and connects to the main controller PCB, which is located on top of the robot, through a socket (labeled as ‘2’ on Figure 2.7).

To run the robot, a single cell 3.7 V, 150 mA h LiPo battery is used and its voltage is boosted to 5 V with a step-up regulator located on the inner flexible PCB (Figure 2.7-3) to power the sensors, the motor drivers, and the microcontroller. The Arduino Pro Micro microcontroller (Figure 2.7-4) is placed on the main controller PCB located on top of the robot, along with two L293DD H-bridge motor drivers (Figure 2.7-5), 16 SMT capacitors, an on-off switch (Figure 2.7-6) and an FFC/FPC socket (Figure 2.7-2) for connecting the inner flexible PCB to the main controller PCB. The battery is connected to the inner flexible PCB and the motors are soldered to the main board, via the pads labeled by ‘7’ and ‘8’ on Figure 2.7, respectively.

2.3 Fabrication and Assembly

2.3.1 PCB Fabrication

Before starting the assembly process of MinIAQ, the electronic boards introduced in previous section must be fabricated. The PCBs are manufactured by coating a masking material on Pyralux, ablating the coated layer with a laser engraver (Universal Laser Systems, VLS 6.60) to create an appropriate mask over pads and traces, and etching of copper at the unmasked locations. Since Pyralux is a thin flexible sheet, it must be flattened and bound perfectly to a flat rigid surface to prevent from forming of wrinkles during ablation process.

Prior to coating the mask material, the surface is cleaned from dust and oils. After initial cleaning, the surface is coated by using a dark, varnish-based paint.

Afterwards, the mask material is ablated with a laser engraver to form a positive mask. Unmasked copper regions are then etched using HCl solvent and the PCB traces remain with mask material on them. The remaining mask material is cleaned with acetone and finally components are soldered to the boards using solder paste and a heat gun. The whole process takes about 4 to 5 hours due to the slow speed of laser raster, relative complexity of the circuits, and high number of vias and components that needs to be hand soldered, see Figure 2.8.

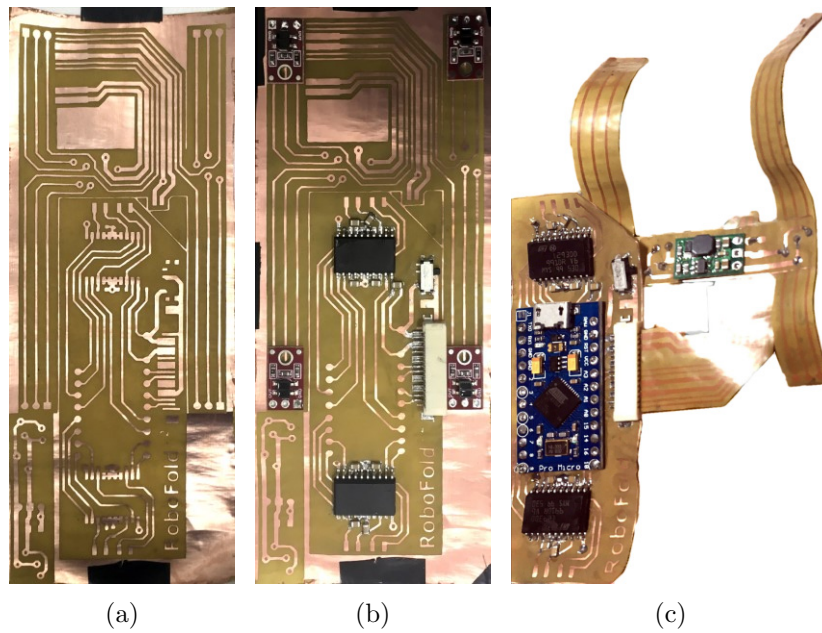


Figure 2.8: (a) PCB without any components soldered. (b) PCB with the motor drivers, IR reflectance sensors, on-off switch, and FFC/FPC connector soldered. (c) Final form of MinIAQ’s circuit board after soldering all components and cutting it into inner flexible PCB and outer main controller PCB.

2.3.2 Robot Fabrication and Assembly

This section explains the manufacturing of MinIAQ from scratch which takes less than two hours to cut, fold, and assemble. The design of MinIAQ was done in AutoCAD and its unfolded cut file is shown in Figure 2.9. The fabrication process begins with laser cutting of the crease pattern, using the aforementioned laser machine, from thin PET sheets which takes about 20 minutes.

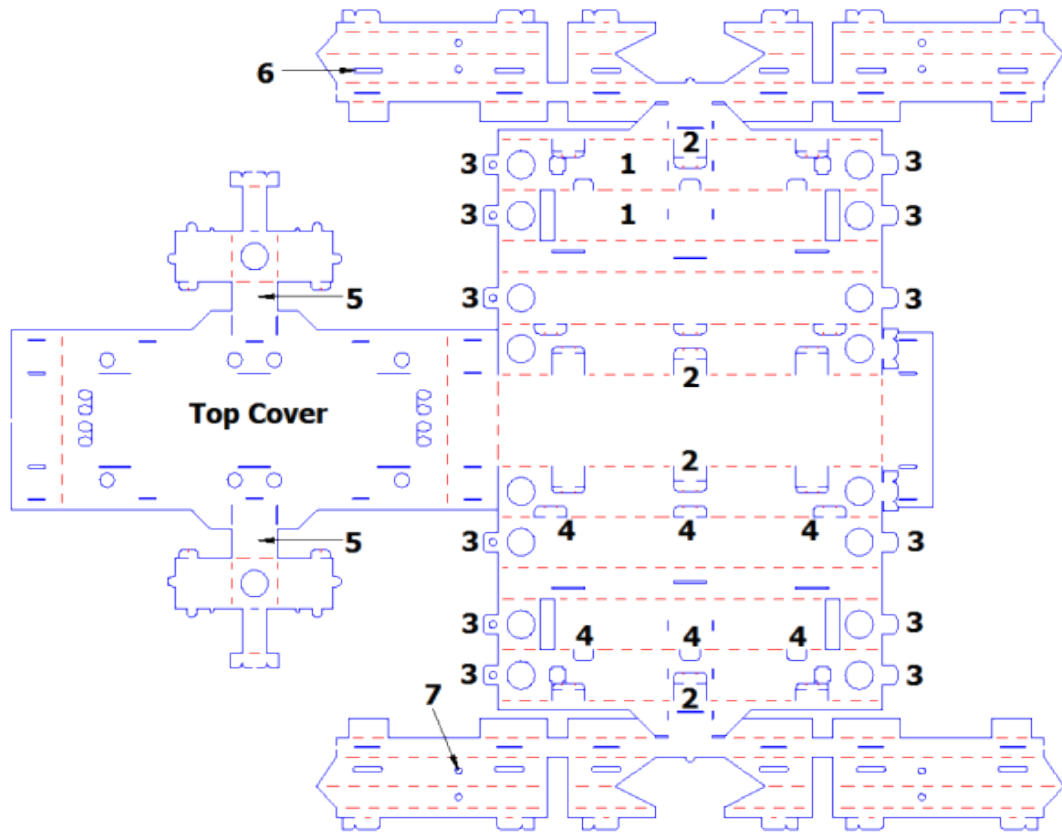


Figure 2.9: The 2D unfolded technical drawing file used for laser cutting where dashed red lines represent the folding edges and continuous blue lines show full cuts. The labeled parts are explained in detail in the text.

The first step in assembling MinIAQ is folding of the T-shaped folds that are labeled as ‘1’ in Figure 2.9. Once all four T-folds are folded, the IR sensors that are soldered onto the inner flexible PCB are placed into their housings within the outer T-folds. Next, the T-folds are fastened by using double-sided tab and slot fasteners (Figure 2.9-2) explained in Section 2.2.3 of this chapter. Afterwards, motors are fitted through the circular housings that are located towards the ends of the T-folds. Then, the extension tabs, labeled as ‘3’ in Figure 2.9, are attached to the front and back of the main frame and are temporarily locked in place with small pins. The top cover of the frame is folded next and locked onto the T-folds by using the U-shaped fasteners existing on top of the T-folds (Figure 2.9-4). Once the main body frame is enclosed, the supports for leg assembly, labeled as ‘5’ in Figure 2.9, are assembled for increased rigidity. These supports consist

of the same previously explained tab-and-slot locking mechanisms introduced in Section 2.2.3.

The assembly of the body can be completed by folding the legs but it is better to keep legs unfolded until the last stage in order to avoid harming the flexure joints. Prior to leg assembly, the battery is placed inside the body and the outer main PCB must be mounted on the top of the frame and be connected to the inner flexible sensor PCB. Then, the legs are folded and their fasteners are locked to form the rigid triangular links. During the assembly process, positioning some of the interior extensions and locking U-shaped fasteners can be challenging. Introducing some slots such as the one labeled as 6 in Figure 2.9 can help overcome this problem. With the help of these slots, one can access the fasteners easily with tweezers or a similar hand tool. Finally, the cams (crank links) are attached to the DC motors' shafts and the legs and cams are connected by inserting a pin through the pin holes (Figure 2.9-7).

The assembled MinIAQ-I is approximately 6 cm wide, 12 cm long from leg-to-leg, and has a maximum height of 4.3 cm. In the absence of any electrical components, the folded body weighs only 3.5 g. The DC motors add a total of 5 g and the PCB, electronic components, battery, and encoders add an extra 14.5 g to the platform making the weight of MinIAQ approximately 23 g.

2.4 Design of MinIAQ-II

The actual running and turning tests of MinIAQ-I [1], presented in Chapter 3, showed that the original robot is relatively slow and cannot maneuver properly due to the poor trajectory of its easy-to-make leg mechanism. Through designing the first version robot, the experience gained on design of foldable actuation mechanisms have been used to create an improved four-bar for higher traction and better stability. The improved mechanism requires links that are not flat, essentially joints that are fixed to a specific angle. In this section, the new version of the robot, named MinIAQ-II, and its design enhancements are presented [2].

A contribution of MinIAQ-II to the design of foldable structures is the use of an alternative approach to optimizing easy-to-fold four-bar leg designs. Furthermore, a systematic approach to creating crease pattern of foldable non-straight rigid links, links with fixed-angle joints in the middle, is introduced. It is believed that the novelties in the design of foldable structures in the original and the new version robots can be applied to similar foldable mechanisms.

Like its predecessor, MinIAQ-II (see Figure 2.10) weighs 23 g, is 12 cm in length, 6 cm in width, 4.5 cm in height, and can walk forward at a faster rate with higher stability (discussed in detail in Chapter 3). Having optimized the actuation mechanism trajectory and observed comparable performance improvements of MinIAQ-II over MinIAQ-I, this robot can be used to perform gait studies in miniature scale robots.

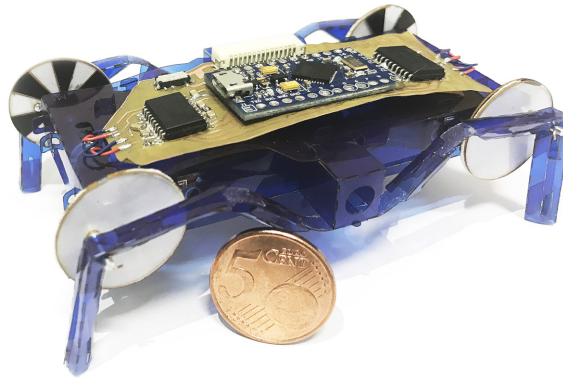


Figure 2.10: MinIAQ-II: The latest version of foldable miniature quadruped robot, with improved leg design.

In fabrication of MinIAQ-II, the same structural material as in the original MinIAQ-I is used, which is 100 μm thick PET sheets. The design of its crease pattern is essentially the same for the main frame enclosure and the only part that is changed is its unfolded four-bar leg design. The leg kinematic chain design follows the same principle of having compliant flexure joints with rigid triangular beams. However, the original straight coupler link is altered into a non-straight link design to resemble a folded knee shape. Further details on the actuation mechanism optimization and its crease pattern design are provided in Sections 2.4.1 and 2.4.2, respectively.

2.4.1 Actuation Mechanism Optimization

The original easy-to-fold four-bar leg design in MinIAQ-I (see Figure 2.3) has a relatively poor trajectory, and in the actual experiments, the robot was found to be quite bouncy and slow relative to its size. Essentially, a flatter and more elliptical trajectory can indeed help maximize the stride length during ground contact and stabilize the body motions. Altering the straight coupler link into a knee-shaped link, as can be observed in many animals, can shift the elliptic trajectory of the foot to be more inline with the ground. But this alteration is not straight-forward due to restrictions of the manufacturing process and 2D unfolded design complexities. Thus, the simplest solution to tackle a non-straight rigid link design is to incorporate a fixed-angle locking joint into the coupler link unfolded design.

Optimizing MinIAQ's leg design for better foot trajectory resembles the case of dimensional synthesis of a four-bar mechanism with path generation constraint. Dimensional synthesis of a mechanism is the technique used in determining a set of appropriate link lengths to achieve a prescribed target trajectory. This target for MinIAQ is to find a point (tip of the foot) connected to the coupler link such that it generates a desirable coupler curve (foot trajectory) [34, 35]. While in MinIAQ-I the tip of the foot is basically just a point along the extension of the coupler link, in the optimized mechanism this point can be anywhere on the planar space of the four-bar, resulting in a non-straight coupler link shape. Prior to synthesis and optimization, kinematic analysis of the leg must be done.

2.4.1.1 Position Analysis of the Four-bar Leg Mechanism

Even though the folded leg of MinIAQ is a flexure based compliant mechanism, in the kinematic analysis of the four-bar outlined below, it is assumed that all joints are ideal revolute joints. Kinematic analysis of compliant mechanisms require nonlinear large deflection beam theories with elliptic integral solutions which are relatively complicated and computationally heavy to solve, making

them not efficient for basic optimization problems [36–38]. The position analysis of MinIAQ’s leg initiates with the assumption that the planar coordinates of the node A (point connected to the robot’s frame) and node B (motor position within the frame) are fixed and the input crank angle, ϕ , is known. Thus, the unknowns become the coordinates of the nodes C , D , and E (Figure 2.11). Note that the actual four-bar mechanism is $ABCD$ and node E is the tip of the foot, making the coupler, CDE , resemble a knee-shaped non-straight link.

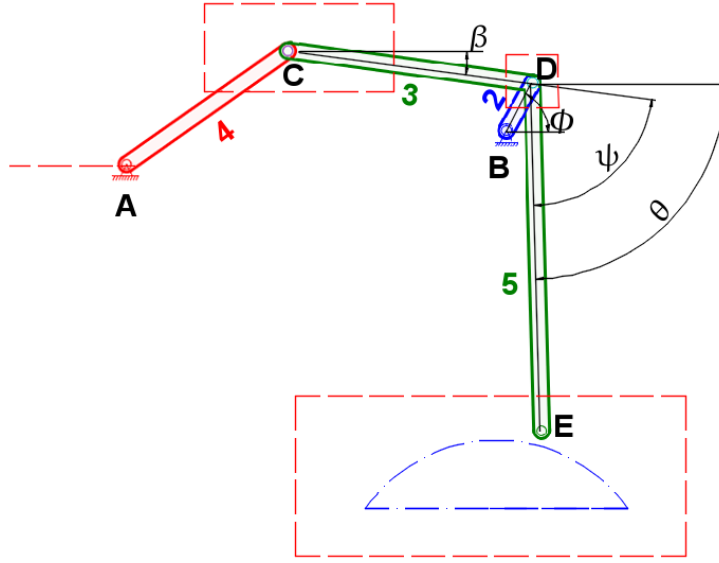


Figure 2.11: A schematic of the generalized modified four-bar leg mechanism considered in the design of MinIAQ-II locomotion. The red dashed lines indicate the nodal design constraints and the blue dashed curve represents the target trajectory used in the optimization algorithm.

Since the length of the cam shaft encoder (link 2) is known, the exact coordinates of node D can be determined by

$$x_D = x_B + l_2 \cos(\phi) \quad (2.1)$$

$$y_D = y_B + l_2 \sin(\phi) \quad (2.2)$$

where l_k is the length of the k^{th} link and x_j and y_j are the planar coordinates of node j . The unknown coordinates of node C can be found using the Pythagorean theorem and the fact that links 3 and 4 have fixed lengths.

$$(x_C - x_A)^2 + (y_C - y_A)^2 = l_4^2 \quad (2.3)$$

$$(x_C - x_D)^2 + (y_C - y_D)^2 = l_3^2 \quad (2.4)$$

Equations (2.3) and (2.4) are nonlinear and should be solved by an analytical or numerical nonlinear method, after substituting the known link lengths and coordinates of A . This is expected from kinematic analysis of a four-bar where velocity and acceleration constraints are linear equations but position constraints are nonlinear [35]. Since the equations are quadratic, solving the nonlinear system for x_C and y_C yields two sets of solution for each unknown. From Figure 2.11, it can be clearly seen that the x-coordinate of node C must satisfy $x_C > x_A$ condition. The ambiguity in selection of correct y_C solution arises from the fact that the mechanism has two closures. Note that the solution with higher y_C value which corresponds to the open assembly configuration is selected over the crossed assembly configuration.

Lastly, the tip of the foot unknown coordinates, x_E and y_E , can be found by considering the fact that links 3 and 5 are technically one link, fixed to each other with a constant positive angle of ψ in between, making them practically one rigid link. Note that, an angle of $\psi = 0$ essentially gives the kinematics of MinIAQ-I. The angle of link 3, β needs to be determined first by

$$\beta = \arctan\left(\frac{y_D - y_C}{x_D - x_C}\right) \quad (2.5)$$

and the angle of link 5 and consequently coordinates of point E can be found.

$$\theta = \beta - \psi \quad (2.6)$$

$$x_E = x_D + l_5 \cos(\theta) \quad (2.7)$$

$$y_E = y_D + l_5 \sin(\theta) \quad (2.8)$$

2.4.1.2 Position-based Trajectory Optimization

The kinematic analysis outlined above provides the basis of the position-based optimization methodology that is employed to determine a set of dimensional parameters giving a desirable target foot trajectory. The utilized optimization technique is based on dimensional synthesis of mechanism with Genetic algorithm approach. Unlike classical deterministic optimization methods which often end up with a local minimum solution, Genetic algorithm has a probability of attaining

the global optimum in the exploration space. It is also simpler to implement with less computational complexities for optimization problems [39–41].

In optimizing MinIAQ’s mechanism, a nodal-constrained single-cost-function multi-parameter approach is taken. In simple terms, the technique is to carefully define constraint regions for placement of each individual node in planar space to form a four-bar leg design whose resulting foot trajectory is as close as possible to a predefined target trajectory. The nodal constraints are shown with red dashed regions on Figure 2.11. The desirable trajectory, which is defined by a straight line stance phase and a short lift swing curve, is also shown with blue dashed line. Even though such target trajectory may be achievable by some well-known linkages such as Chebyshev’s parallel motion [42] or Klann mechanism [43, 44], most of them require either higher number of links or having joints with rotations beyond what a flexure foldable joint offers. Since fabrication of such mechanisms can be very challenging using foldable techniques, the optimization is based upon the initial easier-to-fold MinIAQ–I four-bar linkage.

Selection of the constraint regions are not done arbitrarily to avoid unnecessary customization of the original robot’s crease pattern. The coordinates of the motor, i.e. node B , is fixed at its location. Node A , which connects to the bottom surface of robot’s main frame is restricted to be shifted only along x-direction and away from the other links, at most by a few millimeters (to keep the robot length nearly constant). This constraint on x_A allows a less stressed flexure joint bending (smaller maximum bending angle between links 3 and 4) which has been the primary cause of robot’s failure due to joint fatigue. Similarly, the constraint region for node C , which correlates with the link lengths l_3 and l_4 , is selected relatively wider along horizontal direction to eliminate possible undesired solutions with highly bent flexure joints. The constraint on node D is defined as a relatively small region to ensure that the length of the input crank links, which also serve as encoders for the motors, are neither too small nor too large. Lastly, a relatively large region is defined for the coordinates of the coupler point or tip of the foot, node E , which in other words is equivalent to changing the fixed-angle ψ lock and l_5 link length.

The design input variables for optimization are therefore: x_A , x_C , y_C , x_D , y_D , x_E , and y_E , which are all bounded to aforementioned constraint regions. Given an initial four-bar topology as the starting configuration (such as the one shown in Figure 2.11), the optimization algorithm varies, at each iteration, the input parameters within their bounds and connects the joint positions to form a new four-bar linkage. The resulting four-bar should satisfy the Grashof's mechanism condition [35] which is defined by

$$(L + S) < (P + Q) \quad (2.9)$$

where L and S are lengths of the shortest and longest links, respectively, and P and Q are the lengths of the other two links. When a four-bar is of Grashof's mechanism type, it is ensured that its shortest link (crank) can make a full 360° rotation. This is a must condition for MinIAQ's actuation as the legs are driven by DC motors. For the Grashofs' solutions, the trajectory of the foot is generated for a full turn of crank link.

The last design constraint which is imposed at this point is related with flexure joint limitations. In the actual robot, joints A and C are compliant flexure joints that have limited fatigue lifetime under cyclic loading. Based on observations of MinIAQ-I, the failure primarily occurred at joint C which was undergoing a higher maximum flexure joint bending ($\sim 115^\circ$) than joint A ($\sim 75^\circ$). Due to this reason, a maximum allowable 90° bending is imposed on these two flexure joints. Moreover, in an early iteration of the optimized design, a single foldable compliant leg was made in which the flexure joint at node C had a lower bound of about 10° bending value. In other words, at this respective configuration, links 3 and 4 were becoming nearly inline with each other; where it was observed that by applying a tiny force at the foot or directly on the flexure joint C , the mechanism could very easily switch to its closed assembly configuration which is totally undesired. This surely does not occur in four-bar mechanisms with ideal pin joints but can easily happen in compliant mechanisms. Consequently, a minimum allowable bending of 20° constraint is imposed on node C to prevent such issues. In optimization process, if an assembly satisfies the Grashof's condition but not the joint bending angles constraints, the solution is skipped to the next iteration.

For the solutions satisfying all above-mentioned conditions, the optimization cost function is evaluated as follows:

$$RMS = \sqrt{\frac{\sum_{k=1}^N \min(E_k - T)^2}{N}} \quad (2.10)$$

where N is the number of discrete points at which trajectory is calculated, $\min(E_k - T)$ is the shortest distance from point E to the ideal target curve for the k^{th} discrete point, and RMS is the root mean square error between the ideal and actual trajectories. Thus, the goal is to minimize the cost function by changing the geometry of the mechanism within the pre-defined ranges. This is done in MATLAB environment where the entire parameter space is first explored globally for a solution using *Genetic Algorithm Toolbox*. Once a nearly optimum solution is found, a further localized optimization is carried out with a smaller parameter range centered around the selected solution using `fmincon` function of MATLAB which is essentially a constrained nonlinear multivariable minimizing function based on Interior-Point optimization technique [45].

Figure 2.12 illustrates the trajectories of the optimized mechanism and that of original MinIAQ-I's. With the resulting optimized leg design, it is clear that MinIAQ-II benefits from a longer stride length, improved locomotion stability, improved lateral ground contact, smaller leg lift (less bounciness), and less flexure joint bending.

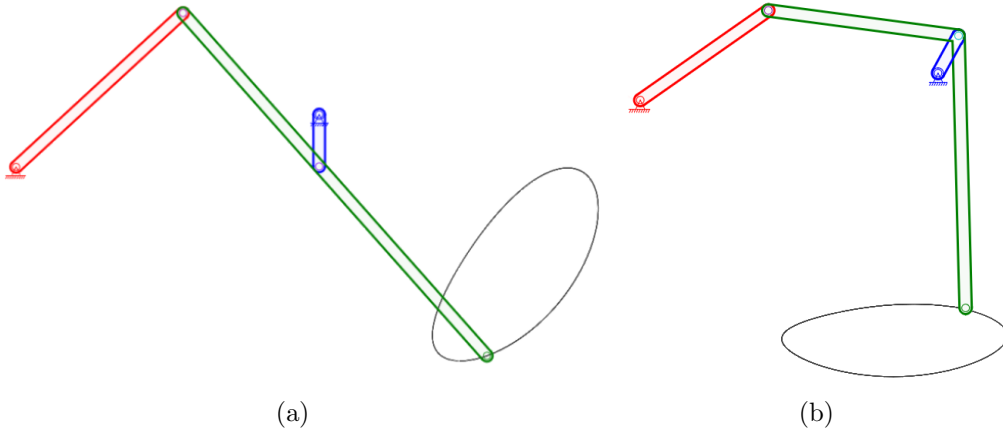
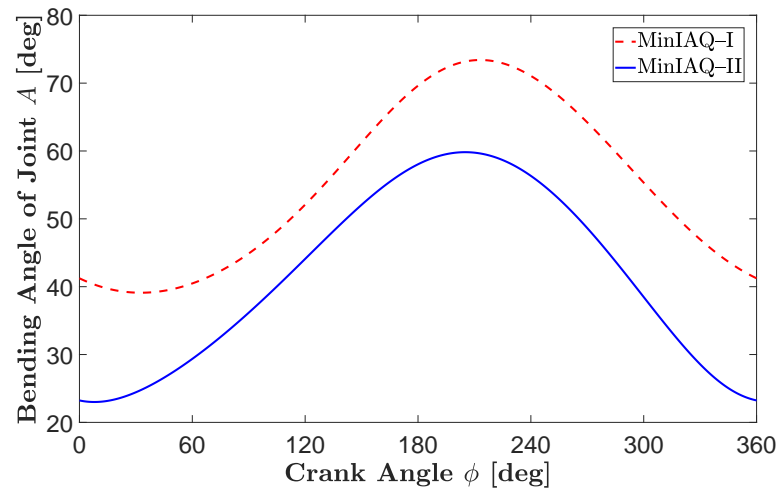
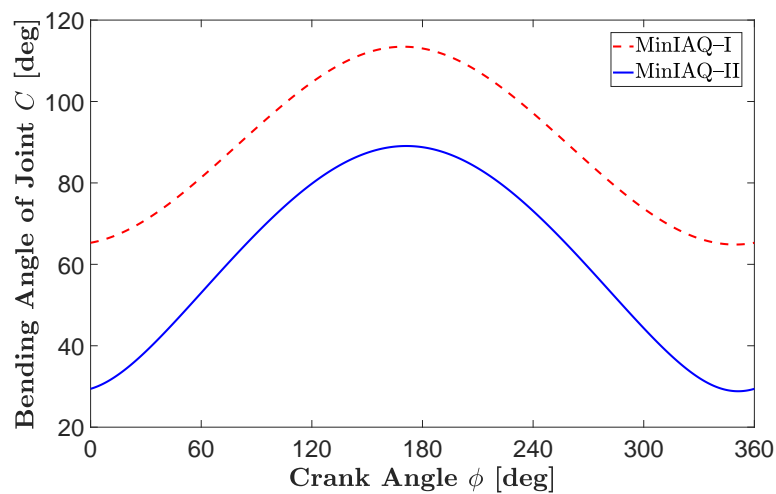


Figure 2.12: (a) Non-optimized mechanism of MinIAQ-I. (b) Leg design of MinIAQ-II with optimized trajectory.

Figure 2.13 shows the variations in bending angles of joints A and C , for a full turn of the crank. It is clearly seen that in the optimized mechanism, stresses on the flexure joints are reduced due to the decrease in joint bending angles. If the bending angle is denoted by β , the imposed constraints of $\beta_A < 90^\circ$ and $20^\circ < \beta_C < 90^\circ$ are satisfied by the optimized solution in which joint A varies between 23° and 60° and joint C between 29° and 89° , approximately.



(a)



(b)

Figure 2.13: Variations of estimated flexure joint bending angles in MinIAQ-I and MinIAQ-II for (a) joint A and (b) joint C .

2.4.2 Foldable Design of Fixed-Angle Joints

The integration of the optimized linkage into MinIAQ's crease pattern requires designing a locking mechanism to precisely obtain a fixed-angle joint between two triangular rigid beams. There are examples of non-straight members such as in gripping mechanism of [24] in literature. However, to the best of author's knowledge, no detail is given on how to systemically design and control the locking angle of such rigid bent links. Many design iterations are done for MinIAQ-II to get a rigid-enough fastener design for its knee-shaped coupler. This section contributes to the design of foldable compliant mechanisms with non-straight rigid links.

The majority of the changes in MinIAQ-II design, compared to the original MinIAQ, comes from its optimized leg mechanism. The final foldable design of its mechanism is shown in Figure 2.14 which illustrates how a single leg is folded in two main steps. The proposed design for the knee-shaped link consists of two regular triangular beams connected by a short flexure joint with an inclined fixed-angle tab-and-fastener locking mechanism.

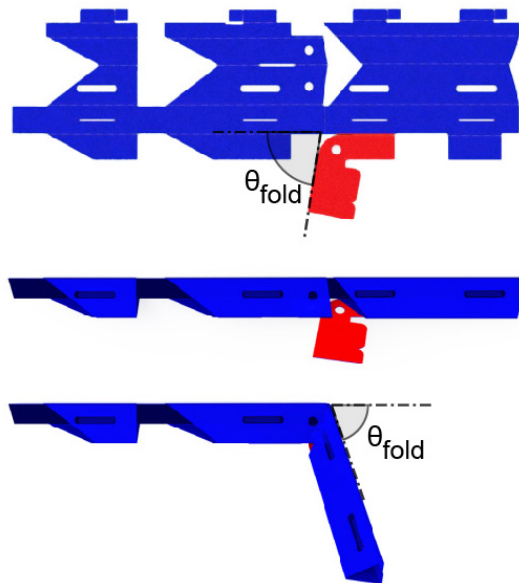


Figure 2.14: A schematic representation of the folding procedure for the new leg design. The knee shaped triangular beam link consists of two triangular beams and a fixed-angle joint that is locked in place with the help of the inclined fastener.

The determination of the fixed-lock angle, θ_{fold} , requires careful consideration of the crease pattern geometry. An optimum solution obtained in Section 2.4.1 is defined by a set of link lengths: l_2, l_3, l_4, l_5 , and the fixed angle between links 3 and 5, ψ (see Figure 2.11). The procedure to transform the optimized four-bar with ideal pin joints into an unfolded compliant mechanism is explicitly described in Appendix A.1. Note that the fixed angle between links 3 and 5 that is shown by ψ here is denoted by θ_{35} in Appendix A.

With the proposed design, any two triangular beams can potentially be locked together at any desired acute or obtuse angles. In MinIAQ–I, the triangular rigid beam are originally folded on top of the flexure joints line, exactly in the opposite sense of MinIAQ–II as shown on Figure 2.14. Folding the links downwards enables achieving a fixed-lock angle of $\theta_{fold} < 90^\circ$. By folding the beams upwards, one will end up having the coupler point (tip of the foot) aiming towards the air at the same locking angle. Hence, it can be inferred that any non-straight rigid link configuration can possibly be achieved by controlling the angle of the fixed-lock together with the folding direction.

Chapter 3

Control and Operation

3.1 Control Problem Definition

Due in part to the fact that efficiency of motors drop by scaling down as well as difficulties arising in control and weight optimization, researchers tend to use the least possible number of actuators in miniature robots. Despite its ease of control and lightweight design, this restricts having freedom on gait control and modification. With an aim to perform gait study in miniature robots, MinIAQ is intentionally designed to run with four independent actuators, one per each leg.

Considering the choice of having four actuators, one of the smallest, cheapest, and lightest commercial DC motors (Pololu, Sub-Micro Plastic Planetary Gearmotor) was selected as its actuation type. However, these motors, like many other tiny actuators, lack internal shaft extensions for encoder use. Difficult tasks of motor characterization and synchronization, as well as lack of actuation sensing in small scale robots are often what aggregates the challenge in control. This chapter gives an insight into how these issues are addressed in MinIAQ. It presents the control strategy for leg synchronization, evolution of custom encoders design, and comparison of both MinIAQ versions performance [1, 2].

Inspired by quadrupedalism [46], terrestrial locomotion of four-legged animals, low-speed trot gait is selected as MinIAQ’s primary form of locomotion for the basis of its control algorithm development. Trotting is a form of movement where each diagonal pair of legs move together and the adjacent legs have 180° phase difference with respect to each other. Thus, the control problem boils down to leg synchronization. In the actual tests, the leg synchronization and gait control is observed to be very crucial for proper walking motion. Therefore, not only the speeds of individual motors have to be matched, but also the relative phase between the legs have to be controlled so that the robot can time its steps based on a selected gait.

3.2 Control Strategy

3.2.1 Custom Encoder Design Evolution

As discussed in Section 2.2.4, four small analog IR sensors (Pololu Reflectance Sensor, QTR-1A) are placed within the frame, next to the actuators, to enable motor characterization via custom made encoders. The encoders, which also serve as the input crank links for the legs, are mounted onto the motor shafts. Many design iterations have been done on these encoders to optimize the generated signal by the optical sensors. Since the control problem requires estimation of both motor speed and absolute leg position, the encoders must be designed such that the phase and speed can be estimated from the feedback signals.

The initial design of the custom absolute encoders resembles that of a single black band on a white circular sheet (Figure 3.1(a)). Each leg is connected to the encoder through a small pin hole whose distance to the center of the cam is equal to the length of the crank link. The output analog signal of this cam is analogous to a periodic signal with single peak per motor rotation. Lower output voltage in the signal is an indication of greater reflection (white surface) and a peak implies detection of a black band (higher absorption). Out of the materials

used to make the encoders, rubbery matte-black electrical tape best absorbed infrared light and white paper or cardboard sheets were reflective enough.

For MinIAQ that is generally run at a nominal frequency of about 2.5 to 3.0 Hz, this cam shaft does not provide more than a few usable discrete inputs to the controller at each second. In simple terms, estimation of motor speed requires two consecutive peaks (obtained after one full cycle) and the position of the leg can only be known when the peak is detected. Thus, during walking trials, it was observed that the speed of the synchronization control loop, which was executed once per each motor rotation, was insufficient to compensate for the highly varying loads on the legs.

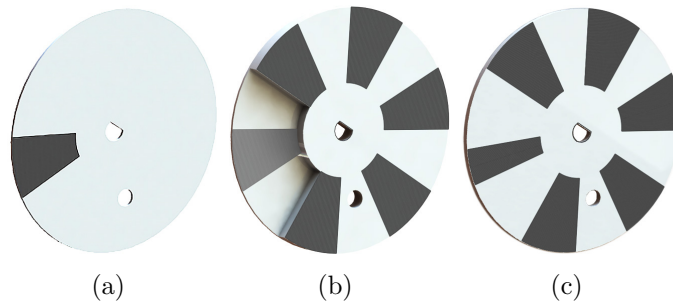


Figure 3.1: (a) Single black band cam shaft encoder. (b) 3D multi-stripe cam shaft encoder. (c) Multi-stripe cam shaft encoder with one thinner black band.

The second design iteration of the custom encoders aimed to address the low number of data inputs and poor speed of the controller. Since a reflectance sensor carries an infrared LED and phototransistor pair, it is expected that its output voltage highly depends on the encoder distance, surface reflectance, and field of view of the emitter and receiver. By taking advantage of the distance sensitivity, a 3D encoder cam, shown in Figure 3.1(b), is designed. In the feedback of the 3D encoders, the gray band that is placed on the back layer generates a relatively lower peak voltage. Hence, the overall signal resembles a periodic multi-peak signal with the amplitude of the peak corresponding to the gray band being noticeably smaller than those of the black stripes on the front layer. This smaller peak serves as a reference to identify the absolute leg position. By this means, the position of the legs over the entire cycle can be estimated based on the number of peaks counted after the reference point.

The selection of the number of black stripes is not arbitrary. In theory, increasing the number of black bands means increasing the peak sampling rate and control loop speed; however, there is a trade-off between this and the reliability of the feedback signal. This is due to the fact that the reflectance sensors have a specific spectral field of view which make them work optimally at a very specific distance, analogous to an optical device working better at its focal point. Moreover, the emitted IR rays are reflected back from a finite region on the surface, and not from a single point. This means that the wider the black stripes (up to a certain limit), the more the absorbed IR rays and, accordingly, the larger the amplitude of the output voltage.

It can be inferred that there is an inverse relation between the amplitude of the output peak voltage and the number of encoder black stripes. In a foldable compliant structure like MinIAQ, it is extremely difficult to obtain the ideal distance between two moving parts such as motor and leg pair. Thinning the width of the black bands much, on top of the further distance of the back layer to the sensor, can cause the amplitude of the smaller peak to be very low and undetectable. A reasonable number of black stripes generating a robust and reliable signal is about 6 to 7, as can be seen on Figure 3.1(b).

While the 3D encoders' feedback signals have the desirable shape we aimed for, they are prone to many issues regarding their severe sensitivity to distance. A little shift in the encoder's position with respect to the sensor results in complete disappearance of the small reference peak and this commonly happens by itself when the robot is running. In order to increase feedback signal robustness, the encoder design is modified to give a more reliable signal, but of exactly the same form. In this manner, the original control algorithm developed for 3D encoders can be used with minimal modifications. The final cam design is a single-layer multi-stripe encoder that incorporates one relatively thinner black band, in place of the 3D gray band (Figure 3.1(c)). This encoder benefits from the IR reflectance field of view sensitivity, instead of distance sensitivity, and generates a more reliable and nearly identical signal to the 3D encoders.

3.2.2 Signal Processing

Figure 3.2 represents the analog feedback signal for a 3D cam encoder, which is very much alike that of a thin band encoder's. As discussed, the signal gives multiple number of high amplitude peaks along with a reference lower peak per each cycle, which helps identify the absolute position of a leg. In order to obtain cleaner signals for control, hardware and software measures are taken. A passive RC low pass filter is designed and integrated into the sensor circuitry which helps reduce unwanted high frequency noise [47]. Moreover, at the software level, a first order Exponential Moving Average (EMA) smoothing technique is used. EMA is a discrete low-pass filter whose output is a weighted sum of the current raw sensor reading and the previous filtered value,

$$A_{filt} = \alpha \cdot A_{raw} + (1 - \alpha) \cdot A_{filt,old} \quad (3.1)$$

where A is the sensor reading and $\alpha \in [0, 1]$ is the filter coefficient controlling how much smoothing is applied. By decreasing α , signal noise and jitter are reduced, but lag is increased in the filtered output as it responds more slowly to input changes. Yet, an EMA filter has less lag than a simple (n-term) moving average filter [48]. Prior to any data filtering, a calibration function is executed to initiate data characterization by analyzing the readings for a full motor rotation and identifying the voltage readings range and initial leg position.

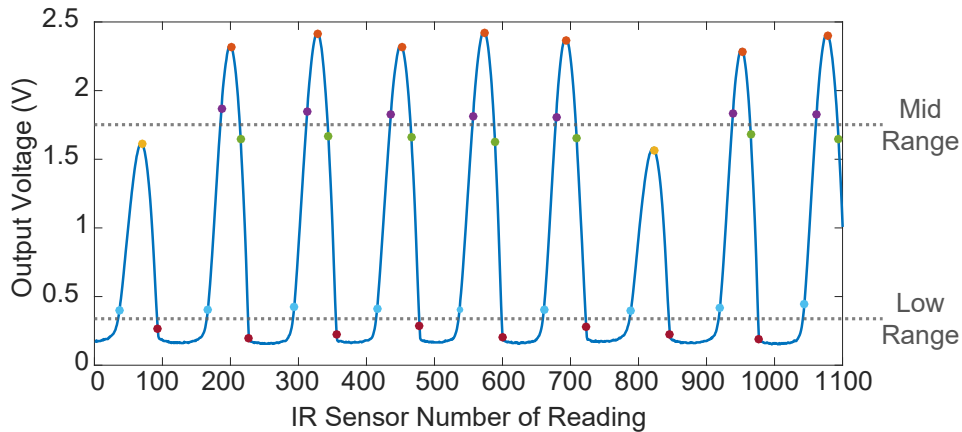


Figure 3.2: A 3D encoder analog output signal with 28 sample points per cycle, detected by threshold crossing method, for the controller input.

While it is possible to generate a control reference input to track the shape of the signal in Figure 3.2, such as a sinusoidal function or fourier transform, it is found to be very difficult in case of MinIAQ. As the whole sensing architecture is custom made, there are many uncertainties that can result in outputting an improper signal. For example shifting in the distance of encoders to the motors is unavoidable during operation and this significantly deteriorates the overall shape of the signal such that reference tracking becomes impractical. In such cases, for a more robust control performance, it is preferred to employ a sampling process that is signal shape invariant.

One of the simplest and most popular shape independent sampling techniques is threshold crossing. Apart from the peaks, whose detections are easy but their number of occurrence over a period is insufficient for a fast controller response, two threshold ranges are set to increase the number of data points (Figure 3.2). Sample values are obtained from the signal at the time instants it crosses the constant-level thresholds, labeled as low and mid signal ranges. These threshold levels are defined automatically by the aforementioned calibration function to detect rise and fall times. A tolerance band is defined around each threshold level to prevent false detection of more than one rise or fall time per each encoder black stripe due to signal oscillation and bouncing. Obviously, any plausible signal deterioration would not affect the threshold crossing criterion as the signal changes below and above the threshold levels are not reflected [49]. Further logical conditions are also implemented into the code to ensure reliable control input data characterization.

In particular, this technique is very convenient for cases where the parameters to be estimated are independent of the signal amplitude such as in phase angle estimation and frequency measurement in MinIAQ [49]. Note that for an encoder with 6 black stripes, 28 discrete points are sampled as shown in Figure 3.2. Every two consecutive data points of the same color correspond to a phase sweep of 60° or 120° , which can be used to approximately estimate the motor rotation speed and determine the relative phase of the signal (leg position) with respect to the small peak reference. These discrete sampled points are used as the controller's input data.

3.2.3 Controller Design

For an armature-controlled DC motor, the transfer function between the applied voltage and output rotational speed is of first order, whereas the transfer function is of second order for motor position. Since DC motors are Linear Time-Invariant (LTI) systems, having constant dynamical behavior defined by linear differential equations, utilizing a linear closed loop feedback control scheme such as PID is a reasonable choice [50, 51]. Figure 3.3 shows the block diagram of the control scheme implemented into MinIAQ. It consists of two interrelated control loops which are fed with the information extracted from the IR sensor signals. In the early control algorithms, the selected controller type for position and frequency was PD. Note that an integral (I) term is often used to increase the type number of a system and eliminate the steady state error; however, generally speaking, an integral action reduces the controller response time and a derivative term can increase it [50]. Since the encoders are custom built, presence of measurement error in frequency and position estimates is inevitable. The accumulation of the integrated errors can grow constantly and cause windup issues and actuator saturation. Accordingly, using integral term in MinIAQ's controller was found to be unnecessary as the system's type number is zero, corresponding to technically no steady state error. It may even degrade the performance due to windup and adversely affect the controller response time which is a crucial factor in a walking dynamic system.

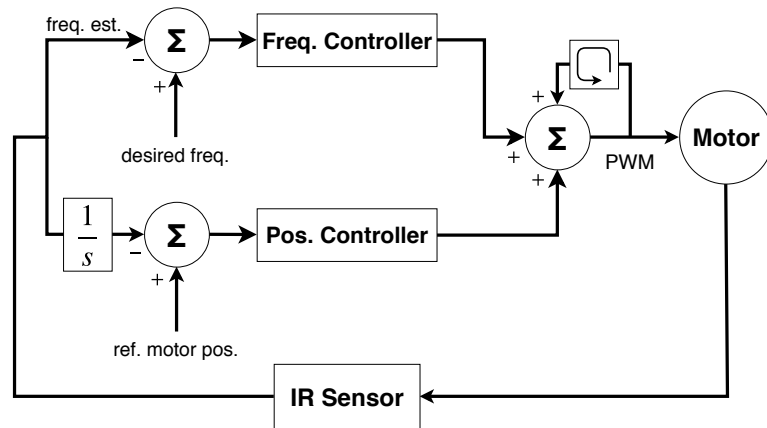


Figure 3.3: MinIAQ's closed loop control algorithm block diagram.

The applied voltage, actuating input, to the motors is controlled via PWM (Pulse Width Modulation) channels of the microcontroller. Since controlling both motor speed and phase relate to the PWM, selection of proper gains is very crucial. To achieve gait synchronization, the idea is to have frequency control loop to dominate primarily in order to adjust the speed of all motors to a relatively similar desired frequency. Once motor speeds are reasonably close, the position synchronization control loop must have the dominance effect such that phase correction is made to reach the desired gait. This is essentially done by carefully selecting the relative order of the frequency gains to the phase control gains.

While PD was originally used in the early versions of the controller design, a lead compensator was favored over it. The control law of a PD implies that when error becomes zero, the controller input is also zero. In case of using directly PWM as the direct control input, a zero PWM means stopping the motors, whereas ideally, the PWM (voltage to the motors) shall remain unchanged. Thus, a modified lead compensator which has a PWM dependent time history term in its control law is utilized. It should also be noted that the time history term acts as an integral action which lessens the sensitivity of the system to the gain changes. This used to be an issue with the derivative action in the presence of high estimation errors. The discrete control law for MinIAQ is defined as,

$$\begin{aligned}
 PWM^i = \alpha PWM^{i-1} + Kp_{freq} \cdot E_{freq}^i + Kd_{freq} \cdot (E_{freq}^i - E_{freq}^{i-1}) \\
 + Kp_{pos} \cdot E_{pos}^i + Kd_{pos} \cdot (E_{pos}^i - E_{pos}^{i-1})
 \end{aligned} \tag{3.2}$$

where E is the error, Kp is the proportional gain, Kd is the derivative gain, and α is a gain dependent constant. The superscripts i and $i - 1$ correspond to the current and previous step values, and the subscripts pos and $freq$ denote position and frequency related parameters. The frequency error is the difference between the estimated frequency and the desired motor speed. As discussed, the speed of each motor is estimated using two consecutive data points of the same color (Figure 3.2). Since encoders are custom made and prone to errors, using data points of different colors for the estimation of frequency introduces higher measurement errors as the exact phase traveled in between them is unknown. The phase error is also estimated by measuring the smallest phase offset (leading or lagging) from the corresponding phase of a reference motor.

The tuning of the proportional and derivative gains of the control law is done experimentally by observing the time response to different set of gains. However this is not arbitrarily done and certain criteria are considered. The range of E_{freq} and E_{pos} are initially observed to have a physical sense of how large the magnitudes of the errors can get. The update rate of the PWM function (28 times per motor revolution) is also taken into account so that the gains are neither selected too small nor too high to prevent actuator saturation. By definition of the selected control law (Equation (3.2)), the derivative of the error is a much smaller quantity than the error itself. This implies that Kd values should be substantially larger than their respective Kp values in order have a meaningful contribution. Last but not least, the previous discussion on the dominating principle of each control loop is taken into account.

3.2.4 Controller Performance

Figures 3.4 and 3.5 represent the time responses of frequency and phase control, respectively. Motor 1 is an arbitrarily selected reference motor where its speed is only controlled and motor 2 corresponds to another motor that does simultaneous speed and phase control with respect to the signal from motor 1. The data is collected through serial communication from an actual robot.

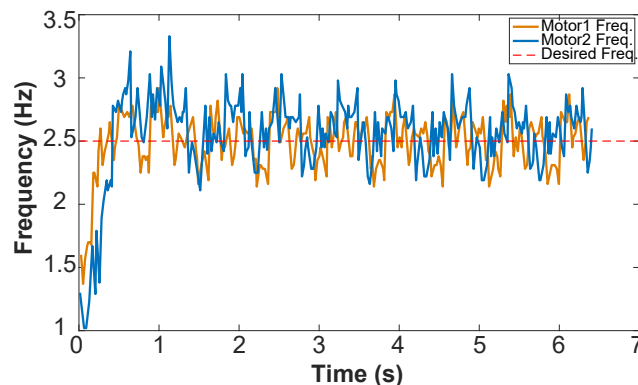


Figure 3.4: Time response of two motors to the controller.

As can be seen from the time responses, the high uncertainty in the estimates is unavoidable due to measurement errors and signal noise. As mentioned, the

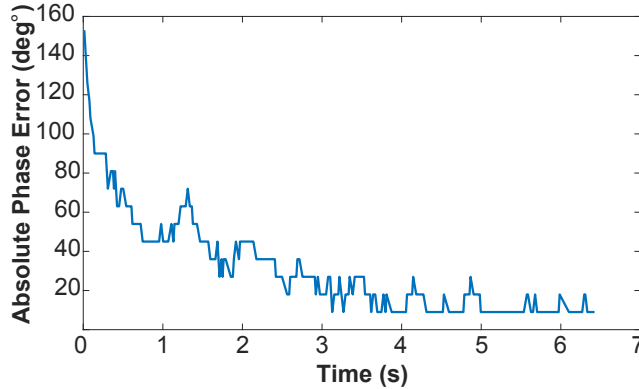


Figure 3.5: Absolute value of phase offset of one motor with respect to another.

performance of the controller explicitly depends on the gains and implicitly on the update rate. On top of tuning the gains, increasing signal sampling rate is also investigated to enhance the response time of the control system. It was observed that increasing the number of sampled data points and update rate of the control system can even adversely affect the controller’s performance in presence of high uncertainty in estimated values. Regardless of controller’s performance, increasing the sampling rate makes the controller more sensitive to rate of error change and can even result in instability issues, especially due to existence of derivative term in the control law [51]. This behavior was clearly seen when controller’s performance started degrading, due to higher oscillations, by adding more discrete data inputs beyond some point.

In regard to Figure 3.5, it should be noted that the error is originally measured by the absolute time difference between the two signals in milliseconds. Conversion of this to an approximated absolute phase offset causes low resolution of the results. Nevertheless, the idea is to highlight that, when MinIAQ is running, the legs are constantly under disturbance caused by touchdown moments impacts. This generates a non uniform momentarily high disturbance to the controller and is relatively difficult to fully recover from. Thus, as can be seen, the phase of motor 2 leads or lags the phase of motor 1 by about 20° which is acceptable to assume that they are nearly synchronized.

There are two factors that can be controlled to synchronize gaits: the relative phase offset between the feedback signals and the relative position of the crank

link pin holes on the encoders. The latter is primarily favored over the former to simplify programming and visualize the results more clearly. Recall that for low speed locomotion, trotting is selected as MinIAQ’s primary gait. In trot gait, the aim is to have diagonal legs be in phase and the adjacent ones be out of phase by 180° . This is achieved by placing the crank pin holes with a relative offset of 180° on each pair of adjacent encoders. Thus, by controlling the feedback signals of all four motors to have zero phase offset with respect to each other, it is ensured that 180° phase difference is attained on adjacent legs, resembling ideal trot gait.

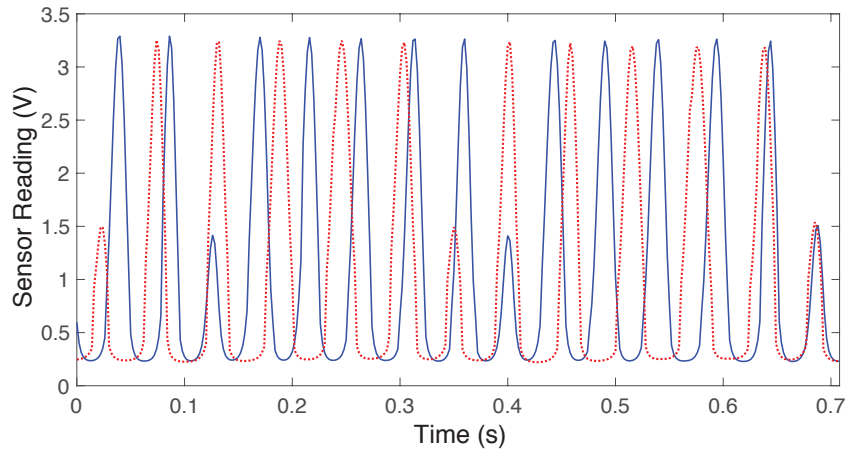


Figure 3.6: Synchronization of two motor signals with respect to each other with zero phase difference, corresponding to 180° phase offset on actual legs.

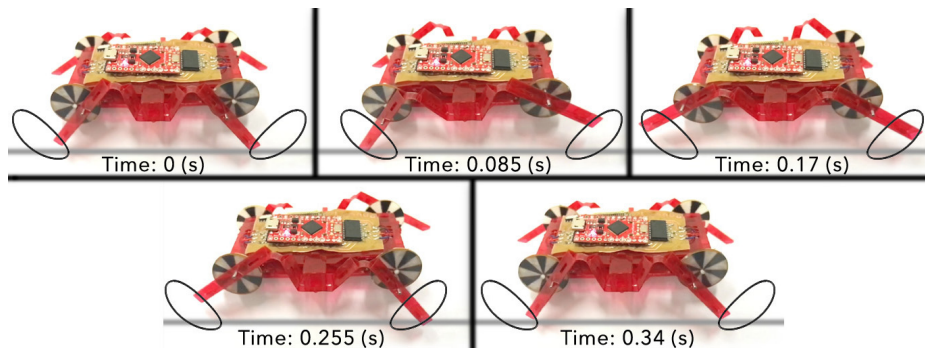


Figure 3.7: Snapshots of the controlled trot gait synchronization of MinIAQ-I over one period at 3 Hz running frequency.

Trot gait synchronization between two motor signals is shown on Creffig:Control Synchronization where the frequencies and position of the motors are controlled such that they are brought into the same phase. This is also shown on the actual

robot by snapshots from a video in Figure 3.7 for one motor period. In a trot gait, the moment of touch-down of one leg should be more or less in sync with the lift-off of its adjacent legs from the ground and vice versa.

3.3 Performance of MinIAQ

3.3.1 Basic Motion Simulation

A 3D CAD model of MinIAQ-I with correct physical and material properties is developed in SolidWorks environment and simulation is done using its Motion Analysis module. The simulation helped better visualize the walking motion of the robot with the selected trot gait, prior to programming the control algorithm. Its results signified the importance of motor speed, surface friction, and contact forces at the legs on MinIAQ's stability and forward motion. A slight decrease in the friction coefficient of the simulation interface results in noticeable slipping of the feet and adversely affects the walking. Figure 3.8 illustrates the trajectory of the front legs for an ideal, reasonably high friction, trot gait locomotion and Figure 3.9 presents the corresponding instantaneous and average forward speed of the robot for a motor speed of 3 Hz. The plots imply that MinIAQ-I can ideally perform trotting with an average speed of 12 cm, or approximately one body length per second, if run at 3 Hz.

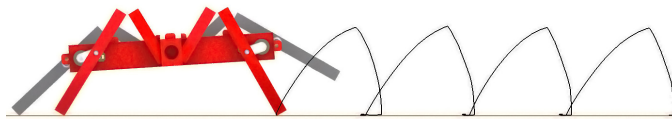


Figure 3.8: Front leg trajectory of MinIAQ-I for an ideal trot gait simulation.

After optimizing the actuation mechanism design of MinIAQ, the CAD model was updated for MinIAQ-II and a similar simulation is done (Figure 3.10). Simulation results verify the new version's superiority over the original robot. It is clearly seen from the trajectories of the front legs that it takes MinIAQ-II three strides to travel the same distance that MinIAQ-I covers in four strides. As expected,

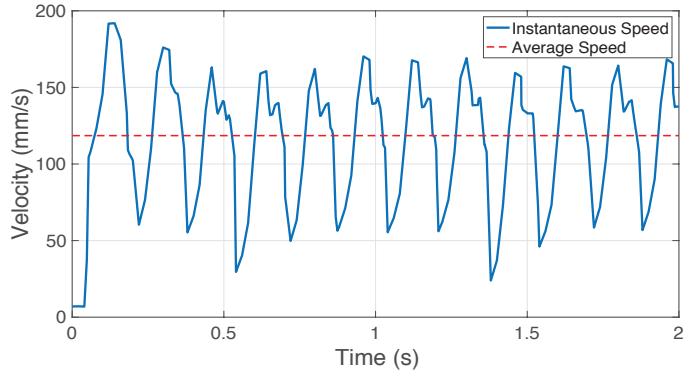


Figure 3.9: Forward velocity of MinIAQ-I for a 3 Hz trot gait simulation .

the trajectories also show smaller leg lifts and longer strides for MinIAQ-II which imply a faster and smoother running performance. While both robots have shown successful performance at different stride frequencies, they are generally run at 2.5 to 3 Hz for tests and simulations because they achieve a more natural and stable quadrupedalism behavior at these speeds.

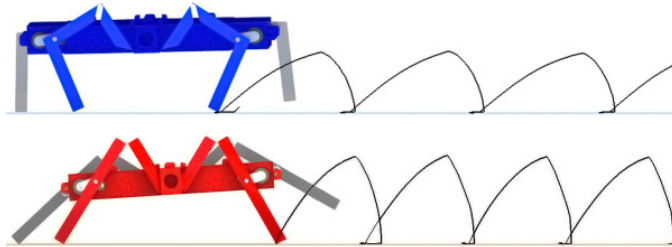


Figure 3.10: Comparison between front legs stride trajectories of MinIAQ-II (top) and MinIAQ (bottom), in an ideal 3 Hz trot gait simulation.

3.3.2 Operation and Experiments

Both versions of MinIAQ are powered by a single-cell 3.7 V 150 mA h LiPo battery. A fully charged battery is capable of running the robots for roughly 30 minutes at normal motor speeds, before battery replacement or recharging is required. The life of the robots are limited by fatigue failure in the flexure joints of the legs. MinIAQ-I generally lasts for less than an hour of constant operation, whereas MinIAQ-II, which has an optimized actuating mechanism for better lifespan, lasts for at least a few hours.

The performance of both robots are tested by several trot gait straight walking and in-place turning experiments and the results are compared against each other. The resulting forward speed of trot gait locomotion is approximately 0.65 body lengths per second (7.5 cm/s) for MinIAQ-I, from more than ten experiments at 3 Hz. On the other hand, MinIAQ-II is capable of trotting at a faster speed of 0.8 body lengths per second (9.7 cm/s) at the same stride frequency. Comparing the ideal simulation with the actual results suggest that simulations considerably overestimate the speed of the robots. This is due to the fact that in actual walking trials, there are non-ideal conditions such as errors in gait control, improper contact between the feet and the ground, less friction, and lower traction which often cause the feet to slip and slide on the ground.

In regard to the body rotations and walking stability, the pitch and roll angles are compared. In contrast to MinIAQ-II, the front legs in MinIAQ-I lift to a level higher than its nominal hip height in the simulations (Figure 3.10) which suggests undergoing relatively larger body rotations. MinIAQ-I's body is observed to be very unsteady in the actual tests, having $\pm 21^\circ$ of body roll and 0° to 11° variation in pitch angle, at 3 Hz trotting. Due to the improved mechanism, MinIAQ-II has a steadier walk compared to its predecessor with significantly less body roll of $\pm 9^\circ$ and pitch of 0° - 7° . Figure 3.11 shows the simulation results of pitch and roll angle variations at 3 Hz, together with snapshots of experimental results corresponding to maximum pitch and roll. The results indicate that there is a good agreement between the experiments and the simulation estimates.

Independent leg actuation of MinIAQ enables better maneuverability such as performing in position zero-radius turning. This is achieved by alternating the directions of motors on different sides such that one side rotates in an opposing manner to the other side. MinIAQ-I performs quite poorly in this task by turning at an average rate of $20^\circ/\text{s}$ for a motor speed of 3 Hz. It is observed that its feet cannot keep traction properly due to the varied load distribution and ends up having inconsistent angular speed and low success rate in turning. However, the relatively better stabilization and balance in locomotion of MinIAQ-II helps the robot have improved maneuverability. Figure 3.12 shows the capability of MinIAQ-II to turn in-place with a speed of $60^\circ/\text{s}$ at 3 Hz.

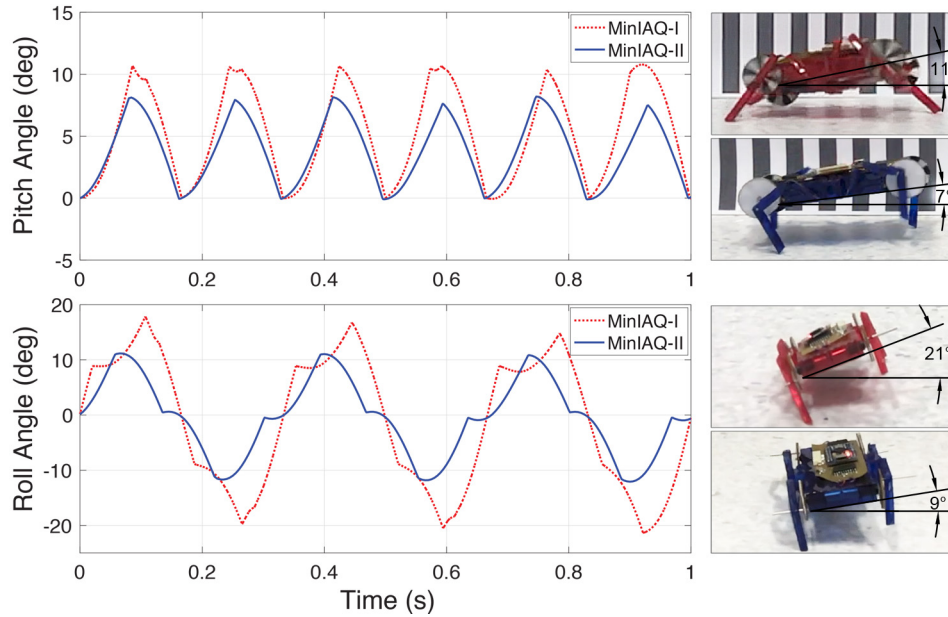


Figure 3.11: Variations of pitch and roll angles estimates from 3Hz trot gait simulation for both versions of MinIAQ. The snapshots on the right show the maximum recorded pitch and roll from actual tests.

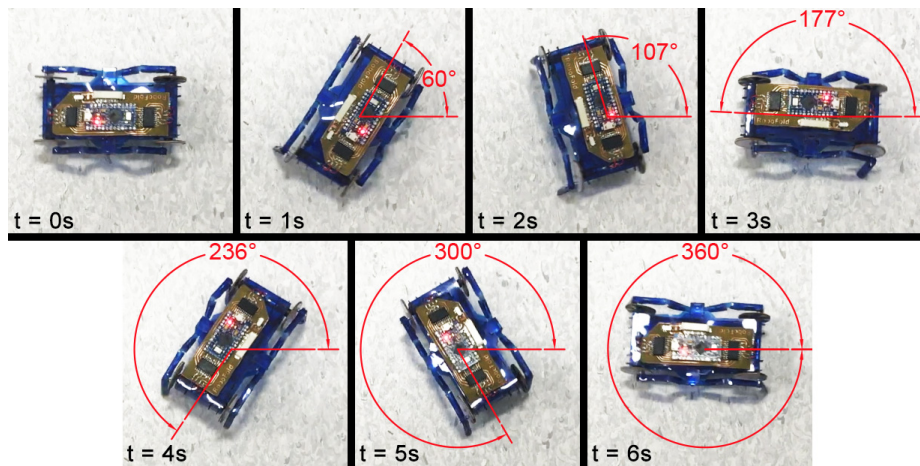


Figure 3.12: Snapshots of MinIAQ-II's improved maneuverability during a zero-radius in-position turning test at 3 Hz stride frequency.

Chapter 4

Dynamic Modeling

4.1 Robotics Modeling Literature

To study MinIAQ's locomotion, determine efficient gaits, and investigate the importance of design parameters on its performance, a 3D full body dynamic model of the robot is required. MinIAQ, like many other legged robots, is an underactuated system as it has six degrees of freedom (6-DOF) in spatial space but is actuated by four actuators, each driving a closed-chain 1-DOF four-bar mechanism with passive joints. Thus, a kinematic model is insufficient to predict the motion of MinIAQ in the configuration space.

While dynamic models of large-scale robots and bio-inspired creatures have been studied extensively, the study of small-scale robotics is an open research field. Many researchers have investigated the underlying dynamics in different kinds of animals and insects [52–61], and many others have been exploiting their findings to design respective bio-inspired walking [3,6,8], crawling [22,23], climbing [62,63], flying [64], and water-striding [65,66] miniature robots.

Most of the aforementioned works are templates to predict dynamic behavior of simple modules of particular robot types, and less describe the full body dynamics

with a more complete realistic model [52]. Furthermore, for the sake of simplicity, many of the existing models describe the dynamics in sagittal- or horizontal-plane and avoid complex 3D kinematics and transformations. Examples of such models are that of a simple 2D sagittal-plane rover model of a quadruped [67] or that of a more complex centipede-inspired many-legged segmented robot with backbone, defined in 2D horizontal-plane [10, 29]. However, for a robot with independent leg actuation and an aim for performing gait analysis, a comprehensive 3D model can give better insight into body rotations and out-of-plane locomotion.

The first and foremost step in dynamic modeling of a legged robot is to develop a mathematical model to predict its legs dynamics. One of the most famous leg models is the Spring Loaded Inverted Pendulum (SLIP) leg template. The SLIP model milestone was first established by [68] to describe the motion of a hopping robot. It has inspired many researchers to develop modified SLIP models, such as in [69] or AKH (Ankle-Knee-Hip) template [70], to better predict the dynamic behavior of different, yet similar, leg structures. Over the past 30 years, from two (or slightly more) DOF hopping and running simple robots [6, 71–75] to as high as a 20-DOF complex robot [76] are modeled and controlled by SLIP.

The SLIP leg template is originally defined by having 2-DOF translation in the sagittal plane [71]. Accordingly, it can best describe planar open-loop legs with active joints or single-link direct-drive legs as in a miniature robot like DASH [6] or in a large-scale robot like RHex [72]. However, for a robot leg with kinematic constraints as in MinIAQ that is driven by 1-DOF four-bar legs with passive joints, SLIP model is relatively difficult to implement. It is very challenging to model the four-bar by a single hip-to-foot fictitious spring as its free length and physical properties would be unknown, let alone modeling of feet slipping effects and predicting the unknown constrained stance and flight phases of the legs. It is believed that for robots such as MinIAQ, modeling the legs by kinematic analysis of closed-chain mechanisms with well-defined planar and spatial constraints can be a better approach.

The lack of thorough understanding of gaits often leads to employ force sensing devices to measure forces and adopt inverse dynamic techniques [77]. However,

this is both infeasible and impractical for small-scale robots where production cost, payload capacity, power, and availability of proper sensing devices are all very limited. For this reason, a reliable model to estimate the ground reaction forces is required. Since SLIP is not easily applicable to MinIAQ’s legs, the friction and contact theory models are thoroughly investigated for an appropriate solution. The result of these efforts is a 3D full body model of a quadruped robot with modifiable gait, able to accurately predict trends in locomotion on flat terrain as shown in Chapters 5 and 6. To the best knowledge of the author, a model of an underactuated robot with passive closed kinematic-chain legs, as developed in this work, does not exist in literature. It is expected that the model presented herein for a miniature quadruped robot can be easily extended and utilized for any similar multi-legged robot.

4.2 Assumptions

The following assumptions are made for the formulation of this model:

1. Legs are modeled as four-bar linkages with rigid links and ideal pin joints, with care for the link shapes. A folded leg of MinIAQ is a flexure based compliant mechanism whose kinematic analysis require solving complex nonlinear large deflection beam theories which is computationally heavy. Furthermore, the legs are considered to remain always parallel to the body and retain their shapes during contact, despite the fact that compliant mechanisms can slightly be deflected laterally.
2. The foot-ground interactions are very challenging to predict and depend on the terrain on which the robot traverse. Here, the assumption made is that the locomotion takes place on a solid flat surface. It is also assumed that the feet make contact with the ground at a single point attached to their tips. This also eliminates the need to model torsional friction at the feet as the contact radius is zero. This is a valid assumption considering the nature of MinIAQ, which is made out of a 0.1 mm thick PET sheet with the leg

links being hollow triangular beams (Figure 2.3), contacting the ground at a tiny segment of the edge of the sheet.

3. Legs are taken to be massless and the entire mass of the robot is uniformly distributed within its main frame. This can also be verified considering the fact that the robot structure, in the absence of actuators and electronics, composes 3.5 g of the net 23 g mass. This implies that all four legs are about 1 g combined which is less than five percent of the total weight. In addition, the majority of the mass is concentrated in the main body which comprises the actuators, the sensors, the PCBs, and the battery, making up to more than 80 percent of the weight. The main frame of is considered to be a rigid rectangular box, with the center of mass located at its centroid, which eliminates the need to consider the forces acting between individual mass elements.
4. Flexure damping and bending energy are comparably negligible as shown by [78]. As the mechanical joints are of flexure type rather than regular pin joints, bending of the flexure joints results in storage of elastic energy in them, according to large angle deflection beam theories [36–38]. It is further assumed here that no buckling occurs at the flexure joints and thus the four-bar leg mechanisms retain 1-DOF.
5. The motors are assumed to be running in a controlled manner at constant speed, keeping the relative phase offset between the legs corresponding to the desired type of gait. While this is easily modifiable in the dynamic equations to study gait pattern alterations during walking, it is taken as so to resemble the actual robot tests, maintaining a single gait.

Additional minor assumptions are pointed out throughout the text.

4.3 Kinematic Analysis of a Leg

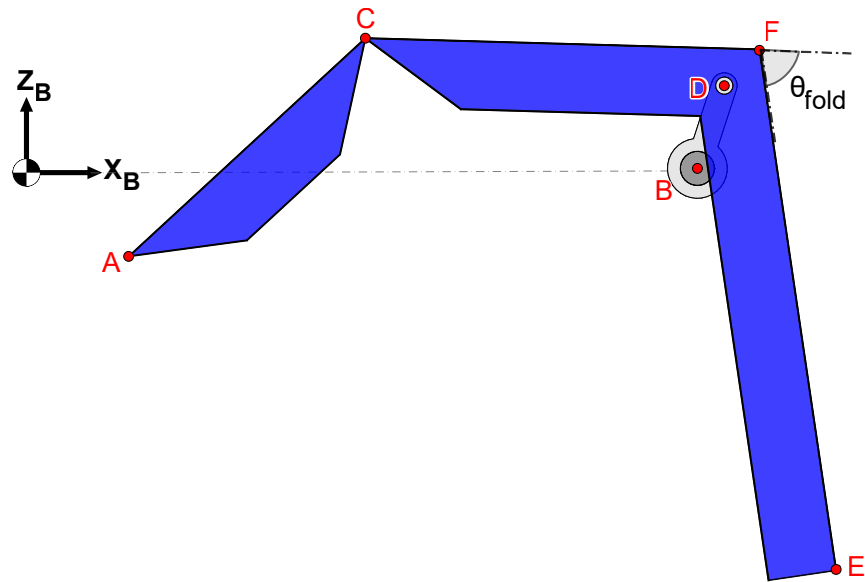
4.3.1 Position Analysis

The kinematic analysis of the four-bar leg linkages begins with position equations. Figure 4.1 shows a schematic diagram of the actual folded leg shape of MinIAQ-II, together with the generalized four-bar model. Since the mechanism is planar and is assumed to remain always parallel to the body frame, the kinematic equations are written with respect to a body-fixed coordinate frame. This body-attached frame is denoted by subscript $\mathcal{B} : \{X_B, Y_B, Z_B\}$ and is located at the center of mass of the robot, at the centroid of the main frame inline with the motors.

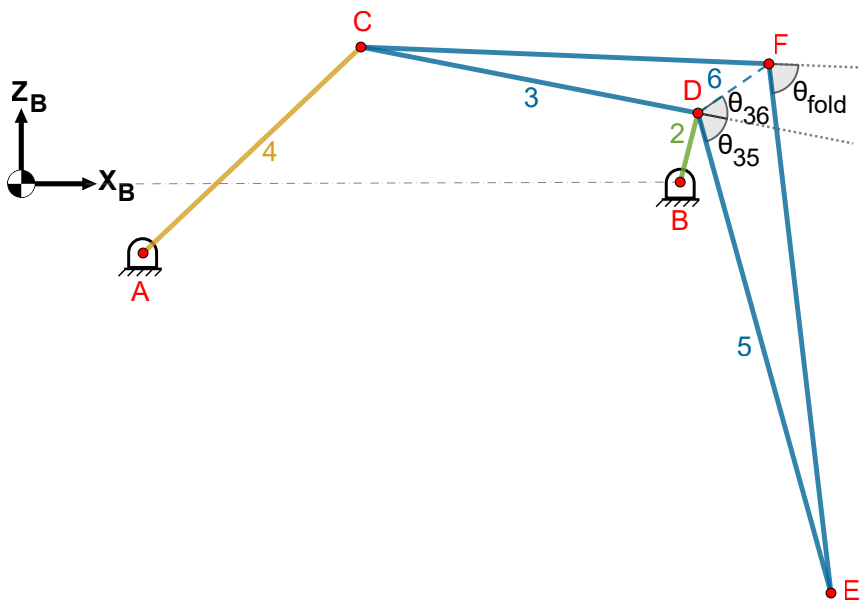
Note that due to the selection of such coordinate system, the direction of Y_B axis is into the plane in Figure 4.1(b). This implies that a clockwise (CW) rotation or angle must be positive and a counter clockwise rotation is negative. However, for the sake of simplicity and to follow the regular notation in a planar mechanism analysis, the four-bar is treated as if it lies in a virtual XY plane. The position kinematic equations are initially solved with respect to this virtual XY plane. At the very last, the angles are negated to match with the aforementioned convention and 3D position vectors defining the joint locations with respect to the body-fixed frame are determined.

The generalized four-bar mechanism shown in Figure 4.1(b) can be used to solve for kinematics of both MinIAQ-I and MinIAQ-II. By setting the knee-shaped link fold-angle to zero, $\theta_{fold} = 0$, and adjusting a few more design parameters, MinIAQ-I legs are obtained. However, for the sake of brevity, the analysis is only shown for MinIAQ-II in this section. The position analysis requires knowing the $ABCD$ linkage dimensions. By the time the crease pattern of MinIAQ-II was designed, examination of the geometry of the legs was not done which resulted in slightly varying link lengths in the compliant folded mechanism compared to the optimized four-bar. These geometrical considerations were addressed at the modeling stage in order to minimize the errors in the model (Figure 4.2). In this regard, the procedure explained in Appendix A.2 is followed. It explicitly

explains how to determine the unknown dimensions of a four-bar with pin joints from the known dimensions of a compliant mechanism.



(a)



(b)

Figure 4.1: (a) A representation of the actual folded leg shape of MinIAQ-II. (b) A schematic diagram of MinIAQ's generalized four-bar leg mechanism with geometrical consideration for the coupler link.

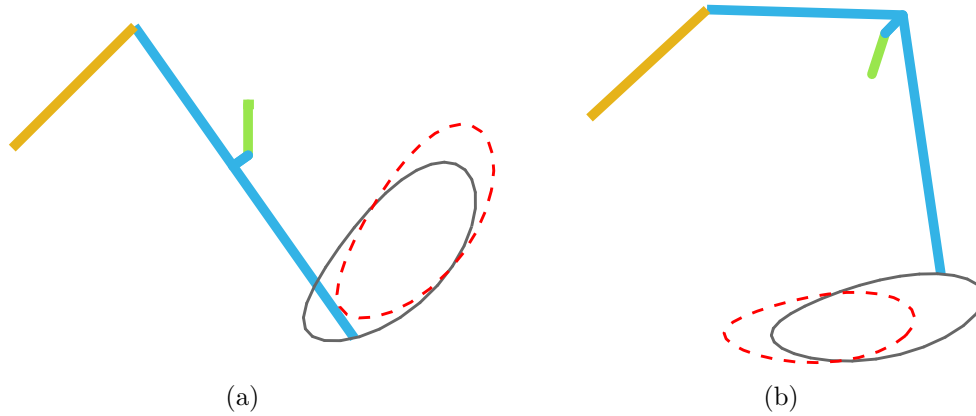


Figure 4.2: Trajectory of the foot with and without geometrical considerations for the knee-shaped link, shown by black solid and red dashed lines, respectively, for (a) MinIAQ-I and (b) MinIAQ-II.

The trajectory of both MinIAQ versions are considerably influenced by accounting for the compliant mechanism geometry as shown in Figure 4.2. This significant error shows the importance of geometrical considerations both in designing and modeling of the compliant legs. Table 4.1 lists the constant link lengths and fixed-angles between link 3 and auxiliary links 5 and 6. Note that the kinematic analysis of the $ABCD$ four-bar leads to determination of planar coordinates of joints C and D . Then, by considering the $CDFE$ knee-shaped link geometry defined by the constants in the table, the nodes E and F are found.

Table 4.1: Constant kinematic parameters for MinIAQ-I and MinIAQ-II.

Robot	l_2 (mm)	l_3 (mm)	l_4 (mm)	l_5 (mm)	l_6 (mm)	θ_{35} (deg)	θ_{36} (deg)	θ_{fold} (deg)
MinIAQ-I	6.00	20.26	20.35	24.95	2.18	11.2	96.2	0
MinIAQ-II	5.10	21.21	18.85	29.15	2.96	69.5	53.4	80

In Table 4.1, l_k denotes the length of the k^{th} link shown in Figure 4.1(b), and θ_k is the corresponding angle of each link measured in the positive CCW direction in the XY virtual plane. To determine the coordinates of the rest of the joints, the input crank angle must be known. Since the model aims to study gaits, the relative phase difference between the crank angles determine the type of gait.

The crank angle (θ_2) is thus defined as a function of time (t) and its constant angular speed ω_2 with an initial constant phase (β_0), set to maintain the desired gait.

$$\theta_{2_j}(t) = \omega_{2_j} \cdot t + \beta_{0_j} \quad (4.1)$$

The subscript j , which denotes the motor or leg number throughout the chapter: $j = \{1, 2, 3, 4\}$, emphasizes the fact that each motor has its own degree of freedom and can run in any direction and at any speed. To clarify this point, consider the case where all motors are running at 3 Hz with $\beta_0 = \{0^\circ, 180^\circ, 180^\circ, 0^\circ\}$ for each motor, respectively. This corresponds to a running with a trot gait at 3 Hz stride frequency. At any given time, for a known input crank angle, the planar coordinates of the joint D in the virtual XY plane are given by,

$$x_D = x_B + l_2 \cos(\theta_2) \quad (4.2)$$

$$y_D = y_B + l_2 \sin(\theta_2) \quad (4.3)$$

The unknown coordinates of the joint C can also be found using the Pythagorean theorem and the fact that links 3 and 4 have fixed lengths.

$$(x_C - x_A)^2 + (y_C - y_A)^2 = l_4^2 \quad (4.4)$$

$$(x_C - x_D)^2 + (y_C - y_D)^2 = l_3^2 \quad (4.5)$$

As expected from position analysis of a four-bar mechanism, these equations are nonlinear and should be solved by an analytical or numerical nonlinear method. The nonlinearity only appears in the position analysis of a four-bar, and not in the velocity or acceleration equations. To speed up the simulation, these coupled equations are further expanded to the following form,

$$\left(x_A \pm \sqrt{l_4^2 - (y_C - y_A)^2} - x_D \right)^2 + (y_C - y_D)^2 - l_3^2 = 0 \quad (4.6)$$

so that a numerical nonlinear technique such as Newton-Raphson method or MATLAB's `fsolve` function can be used to solve for the unknown: y_C . The plus-minus sign in Equation (4.6) indicates that the mechanism has two closures, open and crossed configuration. By looking at Figure 4.1(b), it is trivial that the positive term should be taken, corresponding to the solution with higher y_C value which is the open assembly configuration. x_C is then found from Equation (4.5).

During simulation of the model, it was observed that more than 70 percent of the run time was allocated to solving the nonlinear Equation (4.6). Since this single variable nonlinear equation is, implicitly, a function of θ_2 , it is initially solved for a discrete domain of 10^6 points for the interval $[0^\circ, 360^\circ]$. Then, using this generated lookup table, the solution to any intermediate angle within the domain is found by high order spline interpolation. This approach led to remarkably speed up the solution from order of minutes to a few seconds, at a cost of introducing a negligible error in the order of 10^{-12} mm and less.

Having determined the planar coordinates of the $ABCD$ four-bar joints, all the link angles can be found as follows,

$$\theta_3 = \text{atan2}(y_D - y_C, x_D - x_C) \quad (4.7)$$

$$\theta_4 = \text{atan2}(y_C - y_A, x_C - x_A) \quad (4.8)$$

$$\theta_5 = \theta_3 - \theta_{35} \quad (4.9)$$

$$\theta_6 = \theta_3 + \theta_{36} \quad (4.10)$$

and the location of the coupler point E (tip of the foot) and the folded joint F are determined by,

$$x_E = x_D + l_5 \cos(\theta_5) \quad (4.11)$$

$$y_E = y_D + l_5 \sin(\theta_5) \quad (4.12)$$

The famous $\text{atan2}(y, x)$ function is the arc tangent of the two variables x and y ($\arctan(x/y)$) which computes the correct polar angle of a vector by considering its quadrant. The position analysis outlined above is based on the analysis of the forelegs in MinIAQ-II. The analysis of the hind legs and that of MinIAQ-I's are not presented for brevity, as they only differ by a few sign changes and minimal modifications.

Since the position kinematics of the leg mechanism is done in a virtual XY plane, the solutions found above must be corrected for the actual 3D body-attached coordinate frame, shown in Figure 4.1. As per the assumption that the legs always remain parallel to the robot's frame, all the rotations of the legs links take place in $X_B Z_B$ body-fixed plane. The link angles must then be measured about

the body-fixed Y_B axis which correspond to a positive CW rotation sense in the $X_B Z_B$ plane. As a result, all the θ_k link angles values (Equations (4.7) to (4.10)) are negated to be consistent. Finally, the 3D position vectors for all the joints must be defined with respect to the body-attached frame (see Figure 4.3). These position vectors, \mathbf{rK}_{B_j} , that are given by,

$$\mathbf{rK}_{B_j} = \begin{bmatrix} x_{K_j} \\ \Delta d_j \\ y_{K_j} \end{bmatrix} \quad (4.13)$$

are used later for body transformations in the global world frame. In the above equation, $K = \{A, B, C, D, E, F\}$ corresponds to the leg joints names, j indicates the leg number, and subscript B emphasizes that the position vector is measured with respect to the body origin. x_K and y_K denote the previously found planar coordinates of the joints in the virtual XY plane; and Δd is the constant distance between each leg plane to the $X_B Z_B$ plane, measured along Y_B axis.

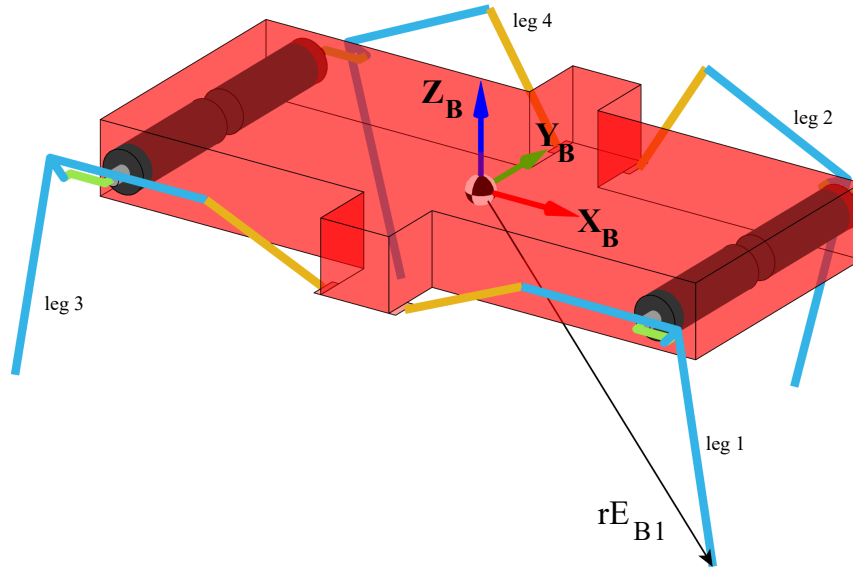


Figure 4.3: A schematic representation of the 3D model of MinIAQ-II, showing the body-fixed reference frame and a position vector to the tip of the right foreleg (leg 1). This is in fact the leg whose kinematic analysis is presented in this section.

4.3.2 Velocity and Acceleration Analyses

Having determined the position kinematics of the four-bar legs in the body-fixed frame, the velocity and acceleration of each joint or link at any instance can be easily calculated. This is relatively straightforward as the velocity and acceleration relations are linear, as opposed to position equations. Since it is assumed that the motors are turning at constant frequencies of f_j , the rotational velocity vector of the crank links in body-fixed frame are given by $\boldsymbol{\omega}_{2\mathbf{B}_j} = \begin{bmatrix} 0 & 2\pi f_j & 0 \end{bmatrix}^\top$. The linear speed of joint D is given by,

$$\mathbf{vD} = \mathbf{vB} + \boldsymbol{\omega}_2 \times \mathbf{r}_{\mathbf{BD}} \quad (4.14)$$

where $\mathbf{vB} = \mathbf{0}$ as the motors are fixed within the body and $\mathbf{r}_{\mathbf{BD}} = \mathbf{rD} - \mathbf{rB}$. Notice that the subscripts B : emphasizing variable being calculated in the body-fixed frame, and j : indicating the leg number, are omitted from the equations for simplification as it is trivial that in this section, every calculation is made with respect to the body frame, for each leg.

To calculate the speed of joint C , the rotational speed of link 3 or 4 is required (see Figure 4.1(b)):

$$\mathbf{vC} = \mathbf{vD} + \boldsymbol{\omega}_3 \times \mathbf{r}_{\mathbf{DC}} \quad (4.15)$$

$$\mathbf{vC} = \mathbf{vA} + \boldsymbol{\omega}_4 \times \mathbf{r}_{\mathbf{AC}} \quad (4.16)$$

where $\mathbf{vA} = \mathbf{0}$ as the joint A is fixed to the robot frame, $\mathbf{r}_{\mathbf{DC}} = \mathbf{rC} - \mathbf{rD}$, and $\mathbf{r}_{\mathbf{AC}} = \mathbf{rC} - \mathbf{rA}$. Subtracting the two equations yields,

$$\mathbf{vD} + \boldsymbol{\omega}_3 \times \mathbf{r}_{\mathbf{DC}} - \boldsymbol{\omega}_4 \times \mathbf{r}_{\mathbf{AC}} = \mathbf{0} \quad (4.17)$$

which can be rewritten as a system of two linear equations by considering the fact that $\boldsymbol{\omega}_3 = \begin{bmatrix} 0 & \omega_{3y} & 0 \end{bmatrix}^\top$ and $\boldsymbol{\omega}_4 = \begin{bmatrix} 0 & \omega_{4y} & 0 \end{bmatrix}^\top$. Thus, expanding the cross products gives,

$$\begin{bmatrix} rDC_z & -rAC_z \\ -rDC_x & rAC_x \end{bmatrix} \begin{bmatrix} \omega_{3y} \\ \omega_{4y} \end{bmatrix} = - \begin{bmatrix} vD_x \\ vD_z \end{bmatrix} \quad (4.18)$$

that can easily be solved to determine links 3 and 4 rotational speed vectors, $\boldsymbol{\omega}_3$ and $\boldsymbol{\omega}_4$, and accordingly find the speed of joint C : \mathbf{vC} . Finally, the linear speeds

of the tip of the foot E and the fixed-fold joint F can be determined by,

$$\mathbf{vE} = \mathbf{vD} + \boldsymbol{\omega}_3 \times \mathbf{r}_{DE} \quad (4.19)$$

$$\mathbf{vF} = \mathbf{vD} + \boldsymbol{\omega}_3 \times \mathbf{r}_{DF} \quad (4.20)$$

Note that even though nodes E and F are connected by auxiliary links 5 and 6 to the joint D in Figure 4.1(b), they are fixed to the coupler (link 3) of the four-bar and thus rotate at the same angular speed of $\boldsymbol{\omega}_3$.

Determination of the speeds of all the links and joints allow performing kinematic acceleration analysis at this point. As per the assumption of having massless legs, the acceleration of the links are not required to be known. However, the equations are presented in brief for the sake of completeness. Since the motors are taken to be running at constant speed, the angular acceleration of the crank links are equal to zero, $\boldsymbol{\alpha}_2 = \dot{\boldsymbol{\omega}}_2 = \mathbf{0}$. Noting that the motors are also fixed in the body ($\mathbf{aB} = 0$), the linear acceleration of the joint D with respect to the body-attached frame can be found by the following vector triple product,

$$\mathbf{aD} = \boldsymbol{\omega}_2 \times (\boldsymbol{\omega}_2 \times \mathbf{r}_{BD}) \quad (4.21)$$

Writing the linear acceleration of the joint C in terms of the unknown rotational accelerations $\boldsymbol{\alpha}_3$ and $\boldsymbol{\alpha}_4$ gives,

$$\mathbf{aC} = \mathbf{aD} + \boldsymbol{\alpha}_3 \times \mathbf{r}_{DC} + \boldsymbol{\omega}_3 \times (\boldsymbol{\omega}_3 \times \mathbf{r}_{DC}) \quad (4.22)$$

$$\mathbf{aC} = \mathbf{aA} + \boldsymbol{\alpha}_4 \times \mathbf{r}_{AC} + \boldsymbol{\omega}_4 \times (\boldsymbol{\omega}_4 \times \mathbf{r}_{AC}) \quad (4.23)$$

Since node A is fixed ($\mathbf{aA} = 0$) and that the angular accelerations of the links are of the form $\boldsymbol{\alpha}_3 = \begin{bmatrix} 0 & \alpha_{3y} & 0 \end{bmatrix}^\top$ and $\boldsymbol{\alpha}_4 = \begin{bmatrix} 0 & \alpha_{4y} & 0 \end{bmatrix}^\top$, the above equations can be expanded to yield the following system of linear equations,

$$\begin{bmatrix} rDC_z & -rAC_z \\ -rDC_x & rAC_x \end{bmatrix} \begin{bmatrix} \alpha_{3y} \\ \alpha_{4y} \end{bmatrix} = \begin{bmatrix} -aD_x + rDC_x \cdot \omega_{3y}^2 - rAC_x \cdot \omega_{4y}^2 \\ -aD_z + rDC_z \cdot \omega_{3y}^2 - rAC_z \cdot \omega_{4y}^2 \end{bmatrix} \quad (4.24)$$

which can be solved to determine $\boldsymbol{\alpha}_3$ and $\boldsymbol{\alpha}_4$, and accordingly calculate \mathbf{aC} . Finally, the acceleration of the feet and folded joints are found using,

$$\mathbf{aE} = \mathbf{aD} + \boldsymbol{\alpha}_3 \times \mathbf{r}_{DE} + \boldsymbol{\omega}_3 \times (\boldsymbol{\omega}_3 \times \mathbf{r}_{DE}) \quad (4.25)$$

$$\mathbf{aF} = \mathbf{aD} + \boldsymbol{\alpha}_3 \times \mathbf{r}_{DF} + \boldsymbol{\omega}_3 \times (\boldsymbol{\omega}_3 \times \mathbf{r}_{DF}) \quad (4.26)$$

4.4 Dynamic Analysis

In this section, the equations of motion describing the 3D 6-DOF rigid body dynamics are presented. Dynamic modeling of mechanical structures are often very complex and require certain techniques for derivation of the equations of motion. In manipulators and open chain mechanisms in general, the underlying kinematic and dynamic equations are often defined using the Denavit–Hartenberg approach [79–81]. However, Newtonian and Lagrangian mechanics are the two primary methods used in deriving dynamic equations of a system. The former is best suited to describe dynamics with vector quantities in rectangular (Cartesian) coordinates and the latter is based on energy principles, scalar quantities, used in conjunction with a set of generalized coordinates [82].

For a rigid body in a three dimensional Cartesian space, Lagrange’s equations require local parameterization for the configuration space to define rotations. Such derivation of the equations of motion would hold locally as singularities can appear at certain configurations [81]. For this reason, to derive the dynamics of MinIAQ, the classical Newton-Euler method is utilized which is well suited to global characterization of a rigid body dynamics subject to external forces and moments in Cartesian coordinates. The notation used in representing the Euler angle transformations and defining the vector quantities are in accordance with the aerodynamics conventions [83–86].

Two sets of coordinate systems are chosen to describe the motion of the robot as shown in Figure 4.4, an inertial (global or world) reference frame fixed in space (denoted by $\mathcal{I} : \{X_I, Y_I, Z_I\}$) and a body-attached frame moving and rotating with the robot (denoted by $\mathcal{B} : \{X_B, Y_B, Z_B\}$). The body-fixed axes, located at the center of gravity of the robot, coincide with the principal axes of the robot’s body, which is assumed to be a rectangular prism with uniform mass distribution. This convention simplifies the moment equations as it makes the product of inertia elements zero and accordingly makes the inertia tensor constant and diagonal with respect to the body-fixed frame. The equations of motion are thus developed in the body frame originally.

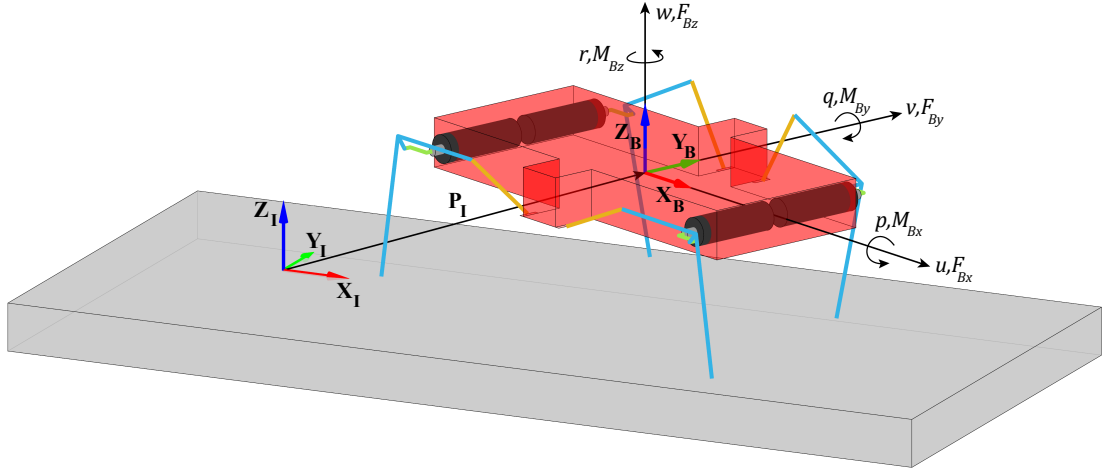


Figure 4.4: A schematic representation of the **B**ody-attached and the **I**ntertial (global or world) reference frames used in deriving the dynamic equations. Unless otherwise stated, subscripts B and I are used throughout the text to emphasize the variables being measured with respect to these coordinate frames. The vectors shown are described in detail throughout this section.

The six degrees of freedom in the body-fixed frame correspond to translation along and rotation about the body axes, denoted by \mathbf{V}_B and $\mathbf{\Omega}_B$, respectively:

$$\mathbf{V}_B = \begin{bmatrix} u \\ v \\ w \end{bmatrix}, \quad \mathbf{\Omega}_B = \begin{bmatrix} p \\ q \\ r \end{bmatrix}$$

The sum of all external forces \mathbf{F}_B and moments \mathbf{M}_B about the body axes, as shown in Figure 4.4, are represented by,

$$\mathbf{F}_B = \begin{bmatrix} F_{Bx} \\ F_{By} \\ F_{Bz} \end{bmatrix}, \quad \mathbf{M}_B = \begin{bmatrix} M_{Bx} \\ M_{By} \\ M_{Bz} \end{bmatrix}$$

The equations of motion describing the body position, orientation, translation, and rotation in the space are developed first, followed by the estimation of external forces and moments. Determination of the forces, which are primarily due to contact of the feet with the ground, requires an in-depth discussion, presented in Section 4.5.

4.4.1 Translational Equations of Motion

Using Newton-Euler formulation, the translational equations of motions in the body frame can be written. It is important to note that body-attached frame is fixed to the robot and moves with it in the world frame. However, Newton's second law ($\sum \mathbf{F} = m\dot{\mathbf{V}}$) is only valid if \mathbf{F} and \mathbf{V} are defined in an inertial coordinate system: that is a coordinate system that does not accelerate or rotate in space. As a result, the Coriolis theorem must be utilized to determine the absolute time rate of change of a moving vector [81, 84]. When working out the acceleration vector, the Coriolis theorem takes into account the contributions to it from both linear velocities (u, v, w) as well as the contributions due to rotation rates (p, q, r) about the body axes. It is important to note that in developing the following equations, a virtual inertial frame coincident with the body-attached axes but fixed in the space is assumed. Therefore, by Newton's second law and Coriolis theorem, we have,

$$\begin{aligned}
 \mathbf{F}_{\mathbf{B}} &= \frac{d(m\mathbf{V}_{\mathbf{B}})}{dt} + \boldsymbol{\Omega}_{\mathbf{B}} \times (m\mathbf{V}_{\mathbf{B}}) \\
 \mathbf{F}_{\mathbf{B}} &= m\dot{\mathbf{V}}_{\mathbf{B}} + \dot{m}\mathbf{V}_{\mathbf{B}} + \boldsymbol{\Omega}_{\mathbf{B}} \times (m\mathbf{V}_{\mathbf{B}}) \\
 \mathbf{F}_{\mathbf{B}} &= m\dot{\mathbf{V}}_{\mathbf{B}} + m(\boldsymbol{\Omega}_{\mathbf{B}} \times \mathbf{V}_{\mathbf{B}}) \\
 \dot{\mathbf{V}}_{\mathbf{B}} &= \frac{1}{m}\mathbf{F}_{\mathbf{B}} - (\boldsymbol{\Omega}_{\mathbf{B}} \times \mathbf{V}_{\mathbf{B}})
 \end{aligned} \tag{4.27}$$

where m is the constant mass of the robot. Equation (4.27) is a first-order ordinary differential equation (ODE) describing the time rates of change of the body-fixed coordinates in an inertial frame instantaneously coincident with the body axes. Since, the equations are time dependent and coupled, it is common practice to expand the ODEs into the following form,

$$\begin{pmatrix} \dot{u} \\ \dot{v} \\ \dot{w} \end{pmatrix} = \frac{1}{m} \begin{pmatrix} F_{Bx} \\ F_{By} \\ F_{Bz} \end{pmatrix} - \begin{pmatrix} qw - rv \\ ru - pw \\ pv - qu \end{pmatrix} \tag{4.28}$$

for ease of numerically solving.

4.4.2 Rotational Equations of Motion

A similar approach is taken in writing the rotational equations of motion. From rigid body dynamics, the time rate of change of the angular momentum equation is equal to the sum of external moments. Thus, to determine the absolute time rate of change of the angular velocities, the rotational version of Newton's second law and the Coriolis theorem for moving frames must be applied together,

$$\mathbf{M}_B = \frac{d(\mathbf{I}_G \boldsymbol{\Omega}_B)}{dt} + \boldsymbol{\Omega}_B \times (\mathbf{I}_G \boldsymbol{\Omega}_B) \quad (4.29)$$

where \mathbf{I}_G is the mass moment of inertia tensor defined by,

$$\mathbf{I}_G = \begin{bmatrix} I_{xx} & -I_{xy} & -I_{xz} \\ -I_{yx} & I_{yy} & -I_{yz} \\ -I_{zx} & -I_{zy} & I_{zz} \end{bmatrix} \quad (4.30)$$

that should be calculated about the body-fixed coordinate axes. As discussed, the body-attached reference frame is selected such that its coordinate axes coincide with the principal axes of the robot rigid body. Note that since legs are assumed to be massless and body is rigid, the inertia matrix becomes constant with respect to the body-attached coordinate axes. Moreover, the non-diagonal inertia values (products of inertia) become zero due to symmetry of the body with respect to the principal axes. For a rectangular prism (MinIAQ's rigid body), the inertia tensor reduces to a diagonal matrix where its elements are calculated by,

$$\begin{aligned} I_{xx} &= \frac{m}{12} (\Delta W^2 + \Delta H^2) \\ I_{yy} &= \frac{m}{12} (\Delta L^2 + \Delta H^2) \\ I_{zz} &= \frac{m}{12} (\Delta L^2 + \Delta W^2) \end{aligned} \quad (4.31)$$

where $\Delta L \approx 88$ mm, $\Delta W \approx 36$ mm, and $\Delta H \approx 10$ mm are the dimensions of the rectangular prism along X_B , Y_B , and Z_B axes, respectively. Since the inertia tensor is constant, Equation (4.29) can be written as a first-order vector ODE,

$$\begin{aligned} \mathbf{M}_B &= \mathbf{I}_G \dot{\boldsymbol{\Omega}}_B + \boldsymbol{\Omega}_B \times (\mathbf{I}_G \boldsymbol{\Omega}_B) \\ \dot{\boldsymbol{\Omega}}_B &= \mathbf{I}_G^{-1} (\mathbf{M}_B - \boldsymbol{\Omega}_B \times (\mathbf{I}_G \boldsymbol{\Omega}_B)) \end{aligned} \quad (4.32)$$

which gives the rotational equations of motion of the robot in an inertial frame instantaneously coincident with the body-fixed axes. Notice that Equation (4.32) is nonlinear due to the Coriolis effect and can be expanded into the following form:

$$\begin{pmatrix} \dot{p} \\ \dot{q} \\ \dot{r} \end{pmatrix} = \begin{pmatrix} \frac{M_{Bx} - (I_{zz} - I_{yy})qr}{I_{xx}} \\ \frac{M_{By} - (I_{xx} - I_{zz})rp}{I_{yy}} \\ \frac{M_{Bz} - (I_{yy} - I_{xx})pq}{I_{zz}} \end{pmatrix} \quad (4.33)$$

4.4.3 Position and Orientation Equations

Up to this point, the rotational and translational equations of motion are derived for the body-attached frame: $\mathcal{B} : \{X_B, Y_B, Z_B\}$. However, for determination of forces as well solving the system of ODEs, the robot's position and orientation in the inertial world frame $\mathcal{I} : \{X_I, Y_I, Z_I\}$ must be known. As shown in Figure 4.5, the position of the robot's center of gravity at any instance is given by the vector

$$\mathbf{P}_I = \begin{bmatrix} P_{Ix} \\ P_{Iy} \\ P_{Iz} \end{bmatrix}$$

where the subscript I is only used to emphasize that the position of the body is measured with respect to the inertial frame. Any two coordinate systems in space can be related to each other through a sequence of three rotations and a translation [86]. In this context, \mathbf{P}_I defines the translational vector between the two reference axes, and to define the rotations, a common approach is to use the Euler angles: roll ϕ , pitch θ , and yaw ψ . In short, roll corresponds to rotation about X_B , pitch defines rotation about Y_B , and yaw is the rotation about Z_B axes (Figure 4.5). Therefore, at any instance, the robot (rigid body) in space can be defined by position vector \mathbf{P}_I and the orientation vector $\mathbf{\Gamma}$, where

$$\mathbf{\Gamma} = \begin{bmatrix} \phi \\ \theta \\ \psi \end{bmatrix}$$

To develop the relations between the body-attached and the inertial reference frames, a convention for the coordinate transformation through the Euler angles must be established. Based on the convention mostly used in aerodynamics, the rotation sequence for Euler angles is yaw-pitch-roll (ZYX) [86]. In other words, if the inertial reference frame is to be rotated to obtain the body-fixed frame orientation, first it must rotate about Z axis by yaw (ψ) amount, then the resulting frame should be rotated by pitch (θ) angle about the intermediate Y' axis, followed by a rotation of roll (ϕ) about the final X'' axis.

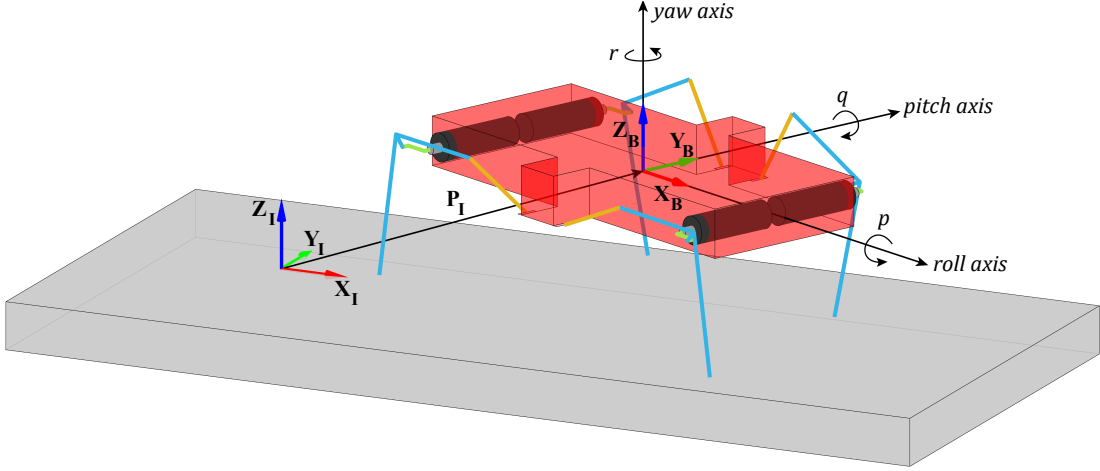


Figure 4.5: A schematic of the position \mathbf{P}_I and orientation $\mathbf{\Gamma}$ definitions: roll (ϕ), pitch (θ), and yaw (ψ) axes on the robot. The rotational speed of the body is also represented by (p, q, r) , as discussed in the previous section.

The basic rotations for roll, pitch, and yaw are defined by,

$$\mathbf{R}_\phi = \begin{bmatrix} 1 & 0 & 0 \\ 0 & c\phi & -s\phi \\ 0 & s\phi & c\phi \end{bmatrix}, \quad \mathbf{R}_\theta = \begin{bmatrix} c\theta & 0 & s\theta \\ 0 & 1 & 0 \\ -s\theta & 0 & c\theta \end{bmatrix}, \quad \mathbf{R}_\psi = \begin{bmatrix} c\psi & -s\psi & 0 \\ s\psi & c\psi & 0 \\ 0 & 0 & 1 \end{bmatrix}$$

where c and s are abbreviations for \cos and \sin , respectively. Thus, any vector defined in the inertial frame can be rotated to the body frame by multiplying it with the following rotation matrix:

$$\mathbf{R}_{I \rightarrow B} = \mathbf{R}_\phi \mathbf{R}_\theta \mathbf{R}_\psi \quad (4.34)$$

$$\mathbf{R}_{\mathbf{I} \rightarrow \mathbf{B}} = \begin{bmatrix} c\theta c\psi & c\theta s\psi & -s\theta \\ s\theta s\phi c\psi - s\psi c\phi & s\theta s\phi s\psi + c\psi c\phi & c\theta s\phi \\ s\theta c\phi c\psi + s\psi s\phi & s\theta c\phi s\psi - c\psi s\phi & c\theta c\phi \end{bmatrix} \quad (4.35)$$

where for any rotation matrix, the notation \mathbf{R} is used throughout this chapter and $\mathbf{I} \rightarrow \mathbf{B}$ denotes that any vector defined in the inertial frame can be represented in the body-attached reference by multiplying with the above rotation matrix. However, the reverse is generally more desired where a vector defined in the body-fixed frame is to be moved to the inertial coordinate axes. Since $\mathbf{R}_{\mathbf{I} \rightarrow \mathbf{B}}$ is an orthogonal rotation matrix, its inverse is equal to its transpose,

$$[\mathbf{R}_{\mathbf{B} \rightarrow \mathbf{I}}] = [\mathbf{R}_{\mathbf{I} \rightarrow \mathbf{B}}]^{-1} = [\mathbf{R}_{\mathbf{I} \rightarrow \mathbf{B}}]^\top \quad (4.36)$$

Having defined the basis of coordinate transformations, the ODEs for position and orientation can now be derived. Since the position vector $\mathbf{P}_{\mathbf{I}}$ is defined in the inertial frame, the body-attached translational velocity $\mathbf{V}_{\mathbf{B}}$ should also be expressed in the inertial frame using the above rotation matrix to write the position ODE as follows,

$$\begin{aligned} \dot{\mathbf{P}}_{\mathbf{I}} &= \mathbf{V}_{\mathbf{I}} \\ \dot{\mathbf{P}}_{\mathbf{I}} &= \mathbf{R}_{\mathbf{B} \rightarrow \mathbf{I}} \mathbf{V}_{\mathbf{B}} \end{aligned} \quad (4.37)$$

which can also be represented as three separate ODEs by

$$\begin{bmatrix} \dot{P}_{Ix} \\ \dot{P}_{Iy} \\ \dot{P}_{Iz} \end{bmatrix} = \begin{bmatrix} c\theta c\psi & s\theta s\phi c\psi - s\psi c\phi & s\theta c\phi c\psi + s\psi s\phi \\ c\theta s\psi & s\theta s\phi s\psi + c\psi c\phi & s\theta c\phi s\psi - c\psi s\phi \\ -s\theta & c\theta s\phi & c\theta c\phi \end{bmatrix} \begin{bmatrix} u \\ v \\ w \end{bmatrix} \quad (4.38)$$

To derive the ODE expressing the rate of change of the Euler angles ($\dot{\mathbf{\Gamma}}$), they should be related to the body-fixed angular velocity vector $\boldsymbol{\Omega}_{\mathbf{B}}$ (see Figure 4.5). This can be done by resolving the Euler rates into the body-fixed coordinate frame as discussed by the ZYX rotation sequence convention,

$$\begin{bmatrix} p \\ q \\ r \end{bmatrix} = \begin{bmatrix} \dot{\phi} \\ 0 \\ 0 \end{bmatrix} + \begin{bmatrix} 1 & 0 & 0 \\ 0 & c\phi & s\phi \\ 0 & -s\phi & c\phi \end{bmatrix} \begin{bmatrix} 0 \\ \dot{\theta} \\ 0 \end{bmatrix} + \begin{bmatrix} 1 & 0 & 0 \\ 0 & c\phi & s\phi \\ 0 & -s\phi & c\phi \end{bmatrix} \begin{bmatrix} c\theta & 0 & -s\theta \\ 0 & 1 & 0 \\ s\theta & 0 & c\theta \end{bmatrix} \begin{bmatrix} 0 \\ 0 \\ \dot{\psi} \end{bmatrix}$$

which yields the following vector ODE equation for the orientation rates,

$$\dot{\Gamma} = \mathbf{J}\Omega_{\mathbf{B}} \quad (4.39)$$

where the matrix \mathbf{J} is defined as

$$\mathbf{J} = \begin{bmatrix} 1 & \sin \phi \tan \theta & \cos \phi \tan \theta \\ 0 & \cos \phi & -\sin \phi \\ 0 & \frac{\sin \phi}{\cos \theta} & \frac{\cos \phi}{\cos \theta} \end{bmatrix} \quad (4.40)$$

This vector equation can also be expanded to represent a set of three distinct orientation ODEs for the pitch, roll, and yaw rates:

$$\begin{pmatrix} \dot{\phi} \\ \dot{\theta} \\ \dot{\psi} \end{pmatrix} = \begin{pmatrix} p + (q \sin \phi + r \cos \phi) \tan \theta \\ q \cos \phi - r \sin \phi \\ \frac{q \sin \phi + r \cos \phi}{\cos \theta} \end{pmatrix} \quad (4.41)$$

4.5 Estimation of Ground Reaction Forces

4.5.1 Contact Mechanics Literature

In order to solve for the system of ordinary differential equations, the input to the system, which is the net external force and moment in the body-attached frame, must be determined. However, the characterization of the ground reaction forces generated due to contact of the feet requires analysis within the inertial reference frame. Studying the contact theory models can give an insight into developing a framework for estimation of the impact and friction forces at the feet.

The study of contact mechanics dates back to 1882 with the fundamental contact theory model presented by Hertz, who studied elastic contact between two curved surfaces. Hertzian contact model established the foundation for modern contact mechanics problems [87]. Due to the assumption of elastic contact in Hertz model

that does not take into account energy loss, many researchers developed linear and nonlinear contact theories to account for energy dissipation. One of the primary examples of dissipative contact models is Kelvin-Voigt's which considers a linear spring in conjunction with a linear damping [88,89]. While this early work has been satisfactory for approximation of the viscoelastic nature of the contact, it is proven not to be suitable for contacts with relatively high impact velocities due to its linear behavior [90].

One of the most established models describing the contact physics is the model presented by Hunt and Crossley [91]. They demonstrated in their work that the loading and unloading energy transfer rates during an impact exhibits a nonlinear behavior. Hunt and Crossley's model represents the contact force by a nonlinear viscous-elastic spring damper element defined by

$$F_N = K\delta^n + D\dot{\delta}$$

Where F_N is the normal contact force, K denotes the generalized spring stiffness, n is the nonlinear exponent, D represents the damping coefficient, and δ and $\dot{\delta}$ are the deformation/penetration depth and rate, respectively. The damping coefficient in this model is expressed as a function of penetration, which makes it more physically realistic. More importantly, Hunt and Crossley's model does not present discontinuities at the initial and termination phases of impact which is crucial in solving ODEs with numerical techniques [90]. Other linear and nonlinear models, from point contact models to hyper-volumetric approaches, are generally based upon the above models [89,90].

In MinIAQ, the contact between the feet and the ground is not a pure impact case but a case of impact with friction. That is, during foot contact, not only a normal force is generated due to impact but also the tangential velocity of the foot vary continuously causing the associated friction force to constantly change magnitude and direction. Study of collision with friction have also been investigated by researchers in [92–97].

4.5.2 Foot Contact Determination

The analysis of the contact begins with the determination of the leg position in the global axis. From kinematics analysis of a leg (Section 4.3), recall that the position vectors to the nodes E_j , representing the tips the foot, are obtained in the body-fixed frame (see Figure 4.3). These position vectors, denoted by $\mathbf{r}_{\mathbf{E}_{B_j}}$, are obviously a function of time only in the body axes. However, since the ground reaction forces occur at the interface of contact, the absolute position vectors to the feet in the inertial reference frame must be known in order to identify whether contact is made between the leg and the ground. This is achieved by a sequence of rotation and translation from body-attached frame to the inertial axes; the coordinates of the feet in the inertial frame are thus given by

$$\mathbf{r}_{\mathbf{E}_{I_j}} = \mathbf{R}_{\mathbf{B} \rightarrow \mathbf{I}} \mathbf{r}_{\mathbf{E}_{B_j}} + \mathbf{P}_{\mathbf{I}} \quad (4.42)$$

where j denotes the leg number, $\mathbf{P}_{\mathbf{I}}$ is the position of the robot's center of gravity (body-attached frame origin), and $\mathbf{R}_{\mathbf{B} \rightarrow \mathbf{I}}$ is given by Equation (4.36). The initiation of contact phase of each foot can easily be determined by checking whether Z_I coordinate of the joint E becomes negative as shown in Figure 4.6. In addition to the interpenetration (position), the impact and friction forces are related to the rate of foot penetration and sliding speeds, respectively. The speeds of the legs with respect to the body-attached frame are estimated by the kinematic analyses of the four-bars and the speed of the body with respect to the inertial axes is defined by the dynamic equations of motion. To determine the absolute velocity of the feet in the global or world frame, one can first consider evaluating the velocity of the feet with respect to an inertial frame instantaneously coincident with the body axes:

$$\widehat{\mathbf{v}}_{\mathbf{E}_j} = \mathbf{v}_{\mathbf{E}_{B_j}} + \mathbf{V}_{\mathbf{B}} + \boldsymbol{\Omega}_{\mathbf{B}} \times \mathbf{r}_{\mathbf{E}_{B_j}}$$

then, apply coordinate transformation to obtain the absolute velocity of the feet with respect to the world frame.

$$\mathbf{v}_{\mathbf{E}_{I_j}} = \mathbf{R}_{\mathbf{B} \rightarrow \mathbf{I}} \widehat{\mathbf{v}}_{\mathbf{E}_j} \quad (4.43)$$

Note that $\mathbf{v}_{\mathbf{E}_{B_j}}$ in the above formulation is given by Equation (4.19). Therefore, at any given time, the absolute position and velocity of the j^{th} leg ($j = \{1, 2, 3, 4\}$)

in the inertial world frame is given by \mathbf{rE}_{I_j} and \mathbf{vE}_{I_j} , respectively. Since in derivation of the feet position and speed, the orientation, position, translation, and rotational speed of the robot appeared, it can be inferred that the ground reaction forces are implicit functions of all system states.

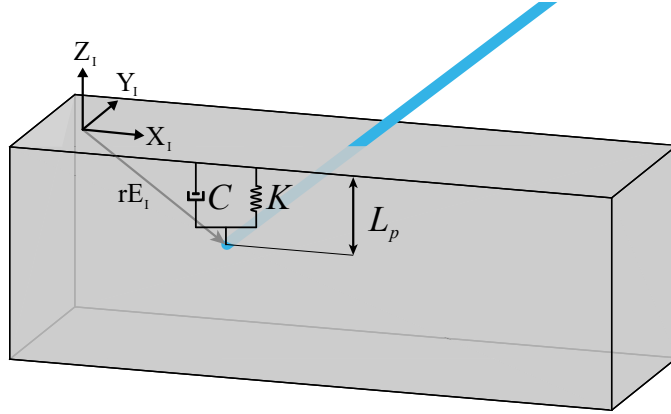


Figure 4.6: Close-up schematic of the interpenetration between a foot and the ground during contact. Analysis of the impact must be done in the inertial axis, leading to the estimation of the normal force along Z_I , and analysis of the friction is done in $X_I Y_I$ plane.

4.5.3 Impact Force Model

The impact model utilized in estimation of the normal ground reaction force is based on Hunt and Crossley's contact theory model [91], with modifications made to avoid discontinuities in the functions. Defining the model with smooth continuous functions and continuous derivatives is crucial as it ensures numerical stability when solving the ODEs. The model presented is based on [93,94] which is originally adapted from [97]. For a leg penetrated into the ground, a normal force is generated as a function of a nonlinear spring stiffness (K) and displacement based damping (C).

$$F_N(L_p, V_p, K, C, e) = \begin{cases} 0 & L_p \leq 0 \\ K(L_p)^e - CV_p & L_p > 0 \end{cases} \quad (4.44)$$

where $C(L_p, c_{max}, d) = STEP(L_p, 0, 0, d, c_{max})$

Note that L_p is the penetration depth and V_p is the absolute foot penetration rate, where both are measured from the tip of the foot to the ground level along the inertial z-axis, Z_I (see Figure 4.6). Equivalently, L_p for each leg is given by negating the third coordinate of $\mathbf{r}\mathbf{E}_{\mathbf{I}_3}$ and V_p by the positive of $\mathbf{v}\mathbf{E}_{\mathbf{I}_3}$ third element. K is the stiffness of the contact boundary, e is the nonlinear force exponent, c_{max} is the maximum damping coefficient, and d is the smallest penetration depth at which maximum damping is applied. The *STEP* function is a smooth cubic approximation to a step of a random variable x , rising at (x_1, y_1) on the horizontal axis and leveling off at (x_2, y_2) :

$$STEP(x, x_1, y_1, x_2, y_2) = \begin{cases} y_1 & x \leq x_1 \\ y_1 + (y_2 - y_1)(\hat{x}^2)(3 - 2\hat{x}) & x_1 < x < x_2 \\ y_2 & x \geq x_2 \end{cases} \quad (4.45)$$

$$\text{where } \hat{x} = \frac{x - x_1}{x_2 - x_1}$$

In selection of the dynamic parameters of the model, it is important to note that the contact boundary stiffness K is not the regular stiffness of a material but a function of both geometry and material properties. Since the material used to fabricate MinIAQ, cellulose acetate sheets, is not a common structural material, its mechanical properties for such models do not exist. Thus, the selected parameters are taken from [97] for a similar plastic material. In addition, it is suggested to select a force exponent of $e > 1.5$, a maximum damping value such that $10^{-3}K < c_{max} < 10^{-4}K$, and the d value as $0.01 < d < 0.1$ mm.

As can be seen from Figure 4.7, selection of $e < 1$ leads to a discontinuity at the derivative of the force at the initiation of contact which is undesired. Furthermore, for a set of reasonable dynamic properties, the penetration is expected to be in the order of tenth or a few hundredth of a millimeter. For such a range of indentation, a higher nonlinear exponent is preferred [97]. The selected dynamic properties for the impact model are tabulated in the next section, in Table 4.2.

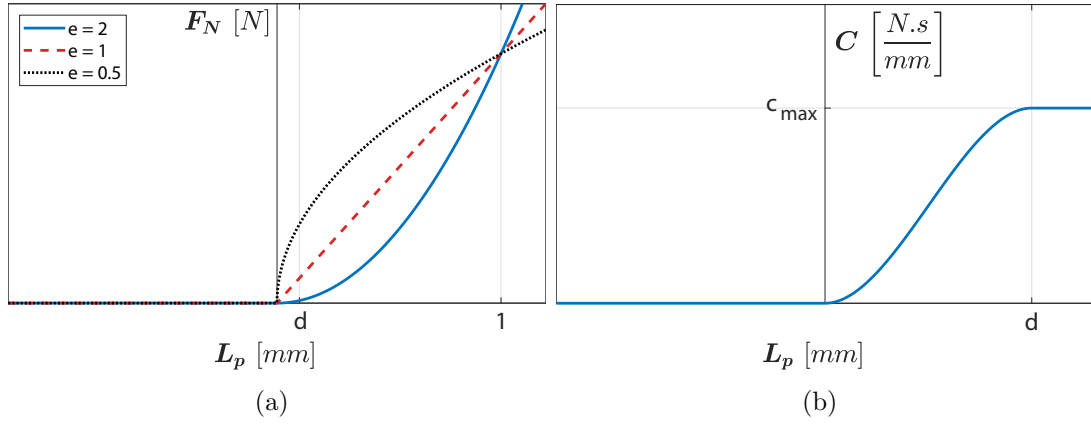


Figure 4.7: (a) Variation of the impact force model with nonlinear exponent and penetration depth and (b) the displacement based damping.

4.5.4 Pseudo-Coulomb Friction Model

The tangential component of the ground reaction force which is characterized as friction is represented in terms of a pseudo-Coulomb dry friction model given by [93]. This friction model is also a continuous function where the assumption is that pure stiction does not occur, but that the bodies in contact continuously move relative to each other at a negligibly small velocity for stiction phase. The direction of the friction force is defined based on the the relative movement of the feet on the ground and its magnitude depends on the pseudo friction coefficient, the normal impact force, and nonlinearly on the relative velocity. The pseudo-Coulomb friction coefficient denoted by μ is given by

$$\begin{aligned} \mu(V_{rel}, \mu_s, \mu_d, V_s, V_d) = & STEP(V_{rel}, -V_d, \mu_d, -V_s, \mu_s) + \\ & STEP(V_{rel}, -V_s, \mu_s, V_s, -\mu_s) + \\ & STEP(V_{rel}, V_s, -\mu_s, V_d, -\mu_d) \end{aligned} \quad (4.46)$$

where V_{rel} is the relative velocity between the feet and the ground, μ_s and μ_d are static and dynamic coefficients of friction, and V_s and V_d are static and dynamic transition velocities, respectively. By definition, μ_s and μ_d are $\in [0, 1]$, typically $\mu_s > \mu_d$, and $V_s < V_d$. The magnitude of the tangential friction force is estimated by multiplying the pseudo coefficient μ with the impact force

$$F_T = \mu F_N \quad (4.47)$$

Calculation of V_{rel} requires further consideration of the instantaneous direction and magnitude of the sliding velocity of the foot which is discussed in the following section. Figure 4.8 conceptually illustrates the approximated continuous Coulomb dry friction model and Table 4.2 lists the dynamic parameters of the contact models used in simulating MinIAQ, most of which are adapted from [97, 98]. It is clearly seen from the figure that the friction pseudo-coefficient, μ , is in the opposite direction of the relative velocity, as expected. This implies that during contact of a foot with the ground, the direction of friction can instantaneously change as the direction and magnitude of the relative sliding velocity changes, and a near-stiction phase occurs where V_{rel} becomes negligibly small.

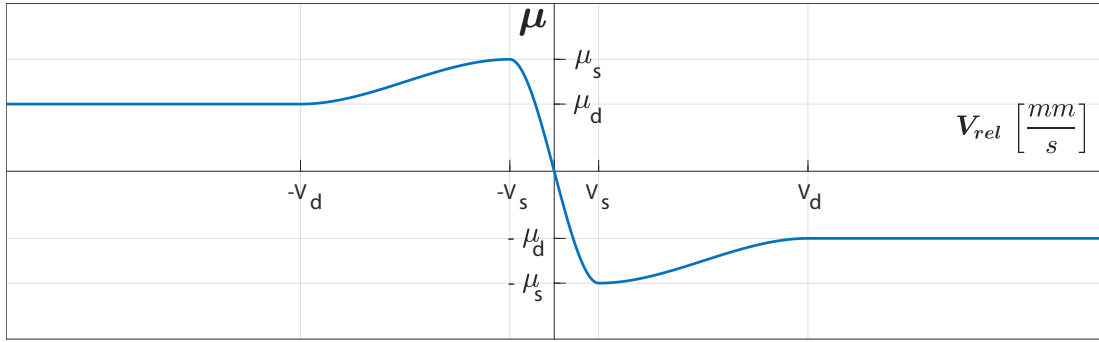


Figure 4.8: Pseudo-Coulomb dry friction model.

Table 4.2: Constant dynamic parameters used in simulation of MinIAQ for the impact and friction force models.

K ($\frac{N}{mm^e}$)	e	c_{max} ($\frac{Ns}{mm}$)	d (mm)	μ_s	μ_d	V_s ($\frac{mm}{s}$)	V_d ($\frac{mm}{s}$)
1150	2.0	0.588	0.1	0.4	0.3	1.0	10

4.5.5 Net Force and Moment Calculation

The aforementioned impact and friction models (Equations (4.44) and (4.47)) provide the basis of estimating the normal and tangential contact forces at each foot. Since the impact model is a function of penetration depth (L_p) and rate (V_p), it is explicitly dependent on the absolute position \mathbf{rE}_{I_j} and velocity \mathbf{vE}_{I_j} of the foot, in the inertial reference frame. In addition, the pseudo friction coefficient

μ is also dependent on the sliding velocity V_{rel} , which makes it a function of $\mathbf{vE}_{\mathbf{I}_j}$. If we denote $\mathbf{rE}_{\mathbf{I}_j}$ and $\mathbf{vE}_{\mathbf{I}_j}$ by $\begin{bmatrix} r_{1j} & r_{2j} & r_{3j} \end{bmatrix}^\top$ and $\begin{bmatrix} v_{1j} & v_{2j} & v_{3j} \end{bmatrix}^\top$, respectively, then for each leg

$$L_{p_j} = -r_{3j} \quad (4.48)$$

$$V_{p_j} = v_{3j} \quad (4.49)$$

$$V_{rel_j} = \sqrt{v_{1j}^2 + v_{2j}^2} \quad (4.50)$$

Equations (4.44) and (4.47) are next calculated to determine the magnitudes of the normal force (F_{N_j}) and the tangential force (F_{T_j}), at each foot. Thus, the contact force for each leg can be written in vector form with respect to the inertial frame as such:

$$\mathbf{F}_{\mathbf{I}_j} = F_{N_j} \begin{bmatrix} 0 \\ 0 \\ 1 \end{bmatrix} + \frac{F_{T_j}}{V_{rel_j}} \begin{bmatrix} v_{1j} \\ v_{2j} \\ 0 \end{bmatrix} \quad (4.51)$$

Note that the tangential force or friction, which is a single force with an arbitrary direction on the $X_I Y_I$ plane (ground surface), is decomposed into its components. Recall that the whole point of the force estimation scheme is to determine the net external force and moment in the body-attached frame (input to the equations of motion, i.e. Equations (4.27) and (4.32)). This initially requires calculating the contact force for each foot in the body-fixed frame by,

$$\mathbf{F}_{\mathbf{B}_j} = \mathbf{R}_{\mathbf{I} \rightarrow \mathbf{B}} \mathbf{F}_{\mathbf{I}_j} \quad (4.52)$$

If we denote the weight in the inertial frame by $\mathbf{W}_{\mathbf{I}} = \begin{bmatrix} 0 & 0 & -mg \end{bmatrix}^\top$, where m is the mass of robot and g is the gravitational acceleration, then the net external force and moment in the body-fixed frame can be evaluated as follows:

$$\mathbf{F}_{\mathbf{B}} = \mathbf{R}_{\mathbf{I} \rightarrow \mathbf{B}} \mathbf{W}_{\mathbf{I}} + \sum_{j=1}^4 \mathbf{F}_{\mathbf{B}_j} \quad (4.53)$$

$$\mathbf{M}_{\mathbf{B}} = \sum_{j=1}^4 \mathbf{rE}_{\mathbf{B}_j} \times \mathbf{F}_{\mathbf{B}_j} \quad (4.54)$$

where recall that $\mathbf{rE}_{\mathbf{B}_j}$ is the position vector of each foot with respect to the body-attached frame, found from kinematics (Equation (4.13)).

4.6 Solving the System of Stiff ODEs

Thus far, the kinematics of the legs, the equations of motion, as well as the procedure to estimate the input to the system of equations (the net external force and moment) are presented. The dynamics of the robot is given by a system of 12 highly nonlinear ordinary differential equations, describing the translation (Equation (4.27)), rotation (Equation (4.32)), position (Equation (4.37)), and orientation (Equation (4.39)) rates in either the body-fixed axes or the inertial frame. If we denote the states by $\mathbf{X} = \left[\mathbf{P}_I^\top \quad \Gamma^\top \quad \mathbf{V}_B^\top \quad \Omega_B^\top \right]^\top$ or equivalently

$$\mathbf{X} = \left[P_{Ix} \quad P_{Iy} \quad P_{Iz} \quad \phi \quad \theta \quad \psi \quad u \quad v \quad w \quad p \quad q \quad r \right]^\top$$

then, the system of ODEs can be represented as follows

$$\dot{\mathbf{X}} = \begin{pmatrix} \dot{P}_{Ix} \\ \dot{P}_{Iy} \\ \dot{P}_{Iz} \\ \dot{\phi} \\ \dot{\theta} \\ \dot{\psi} \\ \dot{u} \\ \dot{v} \\ \dot{w} \\ \dot{p} \\ \dot{q} \\ \dot{r} \end{pmatrix} = \begin{pmatrix} (c\theta c\psi)u + (s\theta s\phi c\psi - s\psi c\phi)v + (s\theta c\phi c\psi + s\psi s\phi)w \\ (c\theta s\psi)u + (s\theta s\phi s\psi + c\psi c\phi)v + (s\theta c\phi s\psi - c\psi s\phi)w \\ (-s\theta)u + (c\theta s\phi)v + (c\theta c\phi)w \\ p + (q \sin \phi + r \cos \phi) \tan \theta \\ q \cos \phi - r \sin \phi \\ \frac{q \sin \phi + r \cos \phi}{\cos \theta} \\ \frac{F_{Bx}}{m} - (qw - rv) \\ \frac{F_{By}}{m} - (ru - pw) \\ \frac{F_{Bz}}{m} - (pv - qu) \\ \frac{M_{Bx} - (I_{zz} - I_{yy})qr}{I_{xx}} \\ \frac{M_{By} - (I_{xx} - I_{zz})rp}{I_{yy}} \\ \frac{M_{Bz} - (I_{yy} - I_{xx})pq}{I_{zz}} \end{pmatrix} \quad (4.55)$$

where recall that c and s are abbreviations for cos and sin terms, respectively, m denotes the mass of the robot, and $\{I_{xx}, I_{yy}, I_{zz}\}$ represent the mass moments of inertia of the robot's rigid body calculated by Equation (4.31). Also note that $\begin{bmatrix} F_{Bx} & F_{By} & F_{Bz} \end{bmatrix}^\top$ and $\begin{bmatrix} M_{Bx} & M_{By} & M_{Bz} \end{bmatrix}^\top$ are the components of the net external force (Equation (4.53)) and moment (Equation (4.54)) vectors along the body-attached axes, respectively. Since the contact forces are implicit functions of all 12 states, they cannot be express explicitly in the above equation and their derivation is discussed in detail in Section 4.5.

In order to solve for the system of ODEs, the initial condition to the system, that is the initial states $\mathbf{X}_0 = \mathbf{X}(\mathbf{0})$ must be known. For a given initial state vector, preferably corresponding to no contact between the legs and the ground for stability issues, the solution to the system of ODEs can be obtained using a nonlinear solution technique. However, it is very important to note that the standard numerical nonlinear methods, such as Euler or Runge-Kutta, can exhibit instability in the solutions, unless the step size is taken to be extremely small. This is investigated to be due to the sharp increase in the contact force at the instance of penetration of a foot into the ground. Since the contact force is dependent on all state variables, a very small change in one of the states can cause a massive resultant force. This behavior in ODEs is described as stiffness that is often characterized by an event that takes place at a much smaller time scale than the time for the motion of the body. The discrepancy in the time scale is what makes for very rapid variation in the solution [99]. Problems involving mechanical collisions are typical types of stiff ODE problems stiff.

The system of ODEs is formulated in MATLAB environment and a built-in stiff integration technique, `ode15s`, to solve for the system. This solver is based on formulations for variable-step variable-order numerical differentiation of orders 1 to 5 [100] and is originally based on the well-known Gear's method [101]. Utilizing a stiff solver (`ode15s`) in comparison to a non-stiff solver (`ode45`, Runge-Kutta method) have proven to exhibit an increase in stability and a significant decrease in simulation time. Since `ode15s` is a variable-step solver, it takes extremely short time steps at the initiation of a foot contact where state variables change sharply

and takes regular steps for the times the forces are more balanced and the system is behaving more stably.

Chapter 5

Model Verification

5.1 Simulation GUI and Experimentation

In order to perform systematic case studies using the derived dynamic model, an interactive GUI (graphical user interface) is carefully designed in MATLAB as shown in Figure 5.1. Prior to running a case study, the GUI enables modifying the dynamic and kinematic settings, choosing from a set of pre-defined robot versions, and selecting a gait pattern. Once the simulation is started, the results at every successful iteration are numerically printed and the plot is updated. The simultaneous visualization and numerical tabulation of the results served well in both debugging the model as well as validating many of the assumptions.

Using the simulation user interface, multiple cases are run for which experimental data of the actual robot exists. At the initial designing phases of MinIAQ, the strategy employed was to develop a control algorithm to resemble an ideal trot gait pattern. This resulted in primarily experimenting MinIAQ-I under trotting with nominal medium speeds, most of which were done at 3 Hz stride frequency. In addition, to characterize the maneuverability capabilities of a miniature robot with independent leg actuation, in-place turning tests were also performed by alternating the direction of rotation of the motors on one side. By the time the

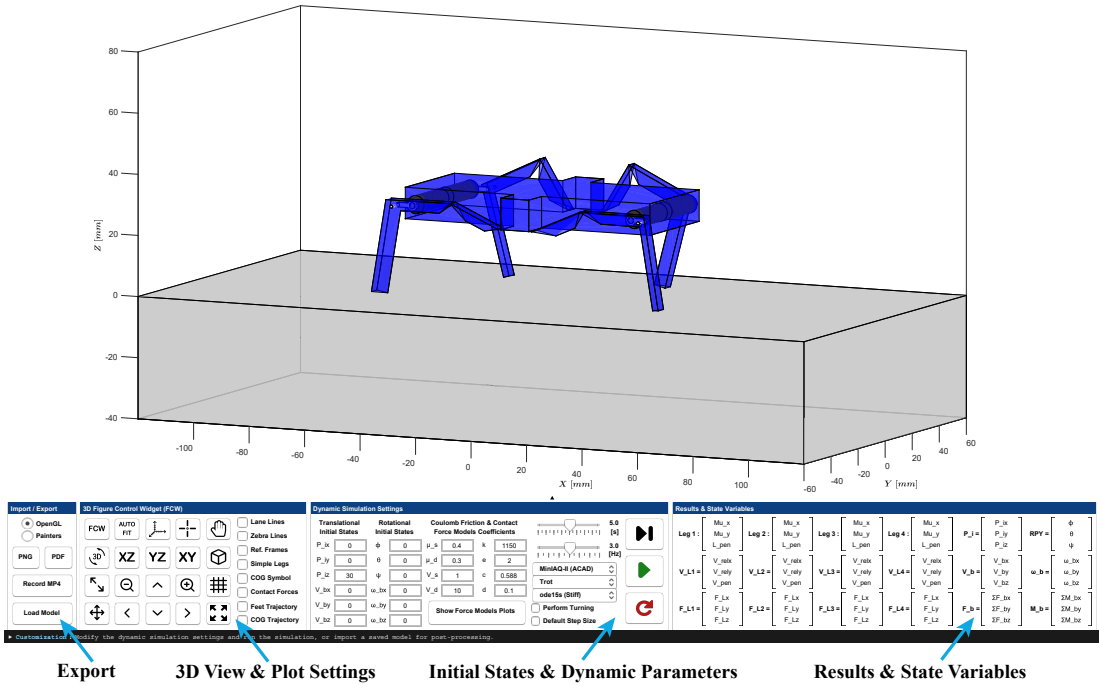


Figure 5.1: An interactive GUI designed for simulating MinIAQ in MATLAB with four control panel toolbars. The 3D view figure control widget is used to interact with the simulation window and modify plot settings. The initial states and dynamic parameters panel is used to select the robot version, adjust gaits and motor frequency, modify the initial state or dynamic variables, and to run, pause or terminate the simulation. The results panel prints the dynamic properties of the system as well as the solution to the current state variables at every successful iteration in time. Finally, the export toolbar enables video recording, screen capturing, and saving the solution or loading an existing model for post processing.

new version of the robot, MinIAQ-II, was introduced, the aim was to demonstrate the performance improvements over its predecessor. Consequently, most of the existing experimental data for MinIAQ-II include the same testing scheme of regular speed trot and zero radius turns.

Since MinIAQ has no sensing device on board, except for motor-encoder IR sensors, the identification of the state variables is not easily done. The existing experiments are in the form of raw video shots of multiple runs for each robot. In manual shooting of a scene, many factors such as poor viewing angle or low FPS (frame per second) recording can aggregate the challenges in experimental data

extraction. Thus, out of more than 20 tests, trot and in-place turning, carried out for each robot, a selective set of those shot in slow-motion (high FPS) with better viewing angle and more realistic results were selected for data extraction.

A MATLAB program was written to read the videos frame by frame where in each one, orientation and position data were extracted manually. Specifically, for trot locomotion, the position of the approximate center of gravity and variations of pitch angle are estimated from the side views, and the rolling effect of the robot is tracked from frontal shots. In turning experiments where the videos are shot from top view, the yaw angle variation corresponding to turning speed of the robot is measured, together with tracking of the position of the robot's frame center. Note that out of all the system's state variables for position, orientation, translation, and rotation rates, manual extraction of position and orientation are possible and estimation of instantaneous translational and rotational speeds would be very difficult and unreliable. These data are compared with the results from simulation for each robot to validate the proposed mathematical model. Outputs from the simulation include a full representation of the state variables and contact forces, however, only results for which experimental validation exist are provided. Note that in the figures provided in this chapter, MinIAQ-I results are shown in red color whereas for MinIAQ-II blue is used.

5.2 Verification of Trot Gait Locomotion

5.2.1 Roll, Pitch, and COG Trajectory Verification

Figures 5.2 and 5.3 show the simulation and experimental results for roll angle variation over five seconds at 3Hz and 2.5Hz for MinIAQ-I and MinIAQ-II, respectively. While the experimental data for MinIAQ-I is extracted from a video with higher FPS, it is clear that the model estimates the rolling effect for both robots reasonably well. Though, there are many factors that contribute to the variations of the experimental data over time, including but not limited

to the errors in data extraction, uncertainties in controller performance for gait synchronization, and the non-ideal interaction of the feet with the ground. Also, it should be pointed out that the results imply a periodic behavior of $\pm 10^\circ$ for MinIAQ-II and $\pm 20^\circ$ for MinIAQ-I, which verifies the superiority of the new version robot.

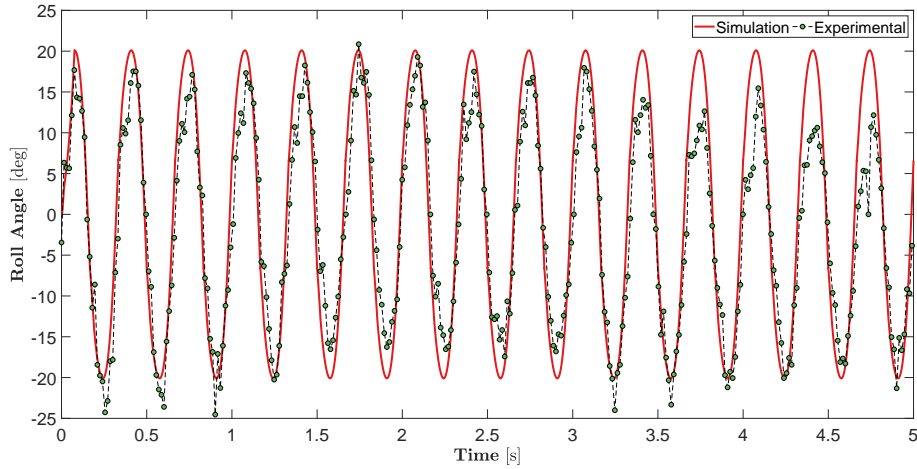


Figure 5.2: Trot gait roll angle verification for MinIAQ-I at 3 Hz.

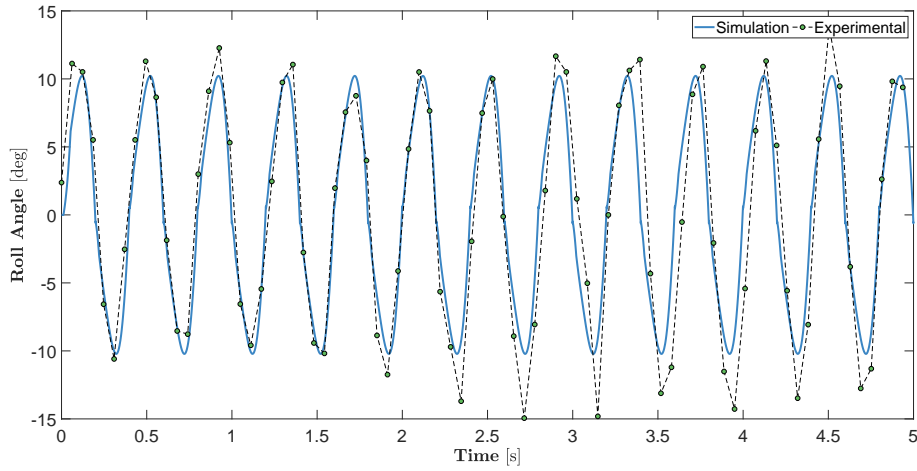


Figure 5.3: Trot gait roll angle verification for MinIAQ-II at 2.5 Hz.

The corresponding pitch angle results are presented in Figures 5.4 and 5.5. Firstly, note that since pitch is measured about the body-attached Y_B axis (see Figure 4.5), a heads-down motion should correspond to a positive pitch and a heads-up effect to a negative pitch. However, the simulation results are negated in sign

to be more physically sensible, where the positive pitch angles represent the front side of the robot to have a higher level than its back side.

Comparison of the simulation and experimental results shows that for half the cycle, the pitch is estimated better than for the other half. Note that every two consecutive peaks corresponds to one full motor cycle. As implied by the symmetric periodicity trend in the simulated data, it is expected to observe a symmetric pitch variation the in experimental data as well, when right and left side legs alternate. This can be justified by the fact that trot is a symmetric gait pattern and must exhibit a symmetric behavior in ideal condition. Yet, by examining the original experimentation videos and the extracted test results in Figure 5.4, it is observed that the robot tends to fall onto one side during locomotion faster than it does on the other side. This behavior, which can be seen more clearly in case of MinIAQ-I’s results, can be attributed to an imbalance in the body. Reasoning for this assumption can be given based upon the fact that the PCB which is mounted on top of the robot is generally shifted towards one side due to assembly reasons. Furthermore, the battery, which composes nearly 25% of the net weight, is placed inside the frame with the help of a hatch opening underneath the robot. Small shift in placement of the battery means a shift in the actual center of mass of the robot. An investigation into this scenario is presented shortly. Regardless of this matter, both simulation and experiments suggest a decrease in maximum pitch angle of MinIAQ-II compared to MinIAQ-I.

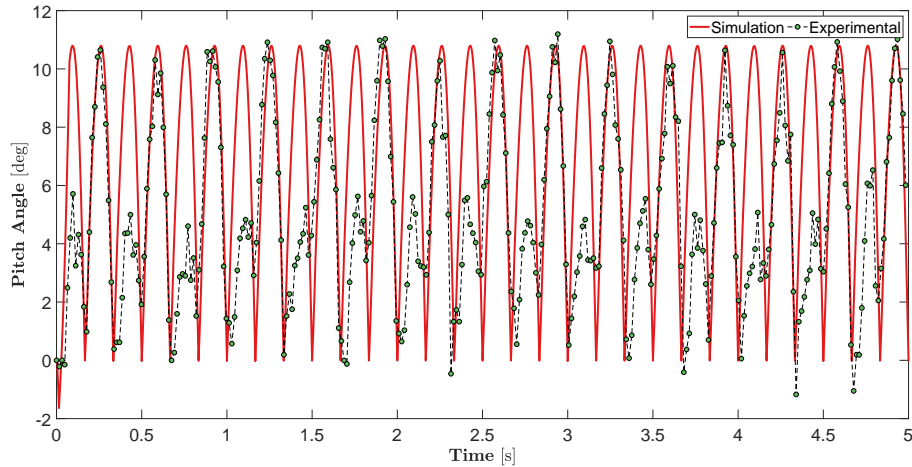


Figure 5.4: Trot gait pitch angle verification for MinIAQ-I at 3 Hz.

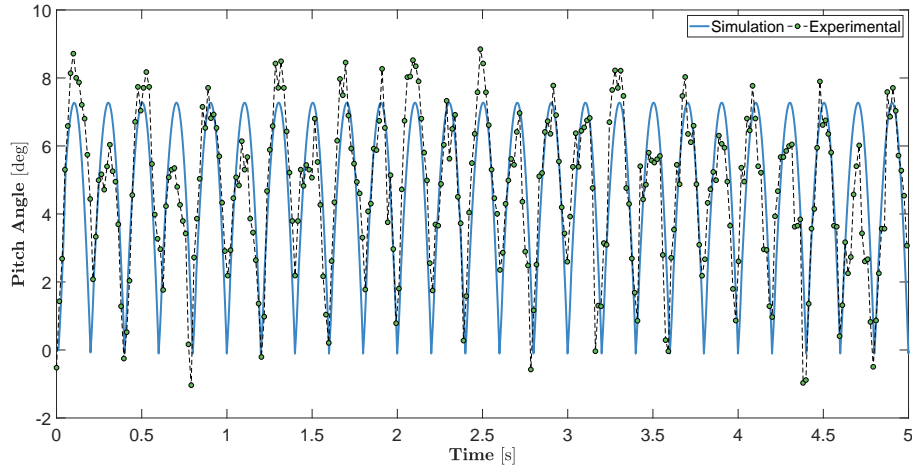


Figure 5.5: Trot gait pitch angle verification for MinIAQ-II at 2.5 Hz.

Finally the simulation and experimental results for tracking the position of the robot over five seconds are shown in Figures 5.6 and 5.7. Since extracting the exact centroid location of the body was difficult from the videos, a point on the side but very close to the COG was tracked and the simulation results are also provided for the same point. It is clear that the model fails to predict the test results in case of MinIAQ-I, whereas the results for MinIAQ-II are in better agreement with the experiments. In the simulated version, MinIAQ-I is found to exhibit a much higher feet slide on the ground, as opposed to the actual experiments where it moves forward at a much faster pace. In spite of this underestimation of the model to predict the forward velocity of the robot, the overall trend in variation of the trajectory along Z_I axis is close. In order to examine the cause for this behavior, the position of the COG in the model is altered as observed from the pitch angle results.

In regard to the trot gait locomotion speed tests, MinIAQ-II traverse on average about 400 mm in five seconds at a stride frequency of 2.5 Hz. This is equivalent to about 0.7 bodylengths per second and by observing Figure 5.7, it can be seen that the robot walks slightly faster at the beginning of the track than towards the end. On the other hand, even at a faster motor speed of 3 Hz, MinIAQ-I covers smaller distance of about 380 mm or equivalently 0.6 bodylengths per second.

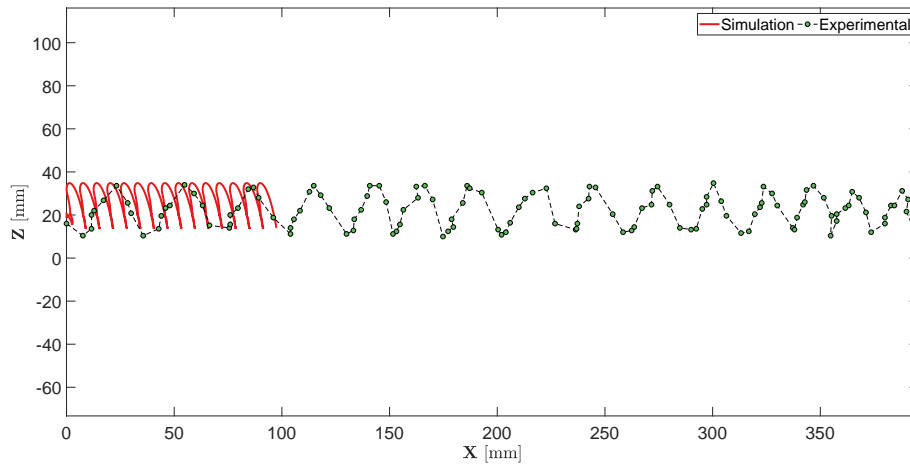


Figure 5.6: Trot gait position trajectory verification for MinIAQ-I at 3 Hz.

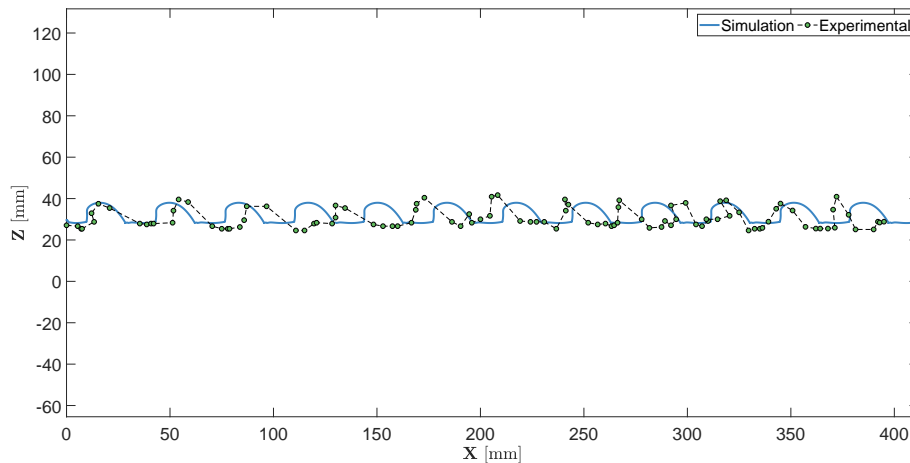


Figure 5.7: Trot gait position trajectory verification for MinIAQ-II at 2.5 Hz.

5.2.2 Effect of Imbalance Verification

As per the observations of the imbalanced behavior of MinIAQ-I in tests, the dynamic model is modified to take into account for a shift in the center of gravity. The location of the COG is moved by 10 mm towards the front and by 2 mm to the left, the former being as a cause of (heavier) battery placement and the latter due to the (lighter) PCB misalignment, illustrated in Figure 5.8. Without altering any other parameter of the system, a 3 Hz trot gait simulation is done for the imbalanced robot and its results are plotted against the experimental data.

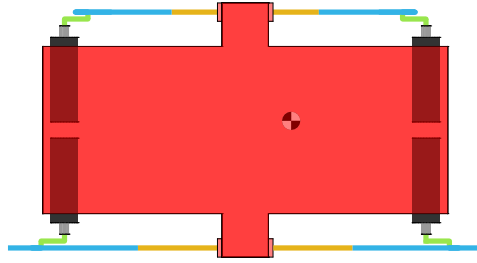


Figure 5.8: A top view schematic of the shift in the COG of MinIAQ-I.

This possible small shift in the COG position of the robot is verified to be the major factor in having the original simulation results not matching with the experiments. The results of the imbalanced model, shown in Figures 5.9 to 5.11, closely match with the experimental data and effectively resembles the shape and trend of the actual curves. Notice that the simulation results for the first one or two cycles should not be considered as they correspond to a non-periodic transient behavior due to the selected initial conditions. Once the periodic stabler phase is reached, the results become very good in agreement. An interesting interpretation of the results, made by comparing Figure 5.6 with Figure 5.11, is that a small imbalance in the COG position can significantly improve the forward movement of the robot by more than three times. The adverse effect would most probably hold too where an imbalance in the opposite sense could make the robot perform poorly. Despite the uncertainties in the actual testing environment, the model serves well in predicting trot gait locomotion trends on flat terrain.

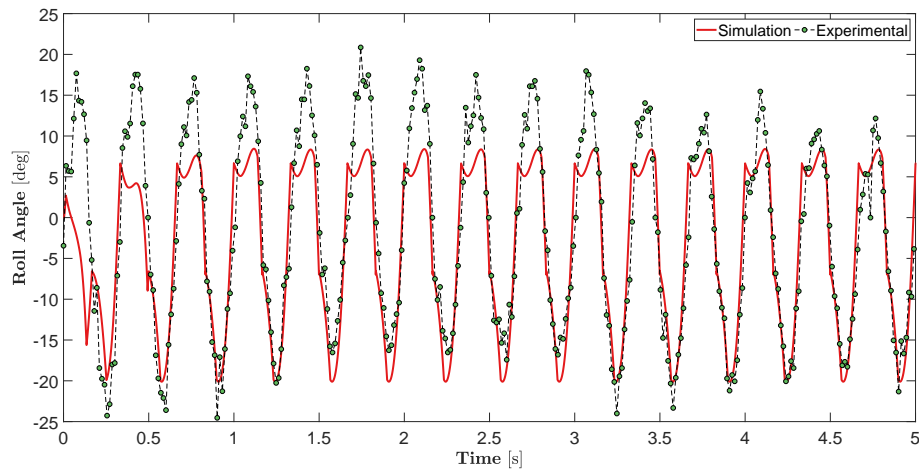


Figure 5.9: Trot gait roll angle for imbalanced MinIAQ-I at 3 Hz.

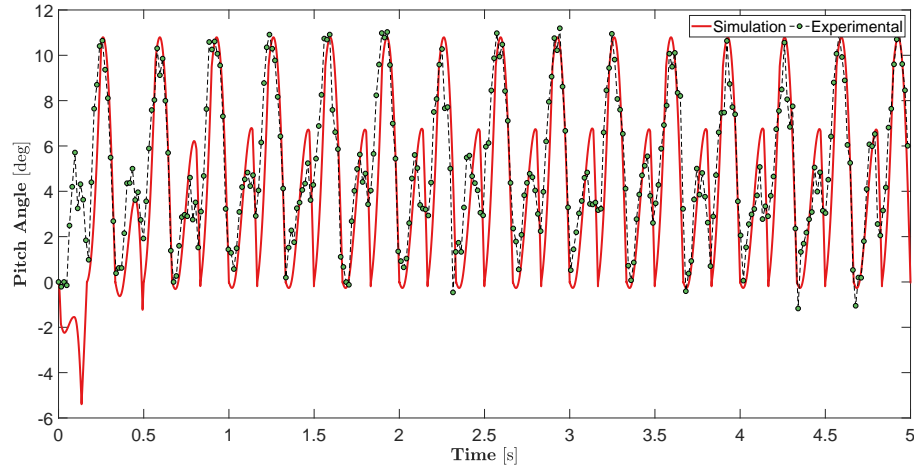


Figure 5.10: Trot gait pitch angle for imbalanced MinIAQ-I at 3 Hz.

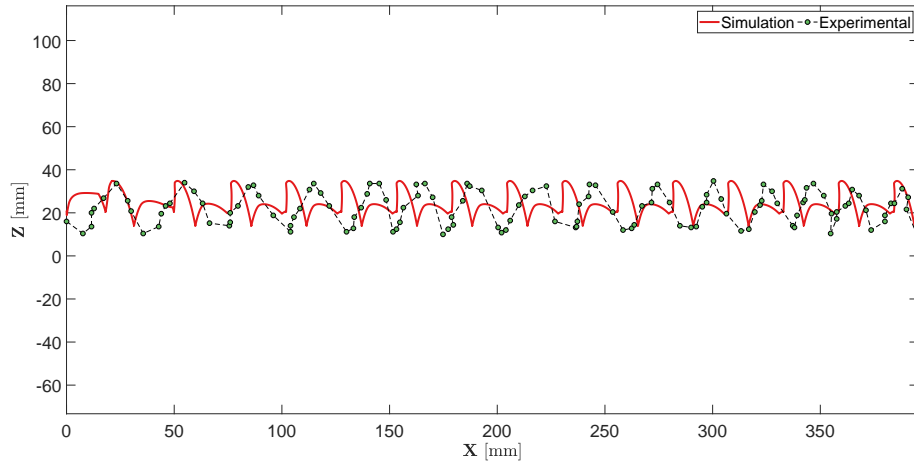


Figure 5.11: Trot gait position trajectory for imbalanced MinIAQ-I at 3 Hz.

5.3 Verification of In-Place Turning

5.3.1 COG Tracking and Turning Speed Verification

In performing zero radius turns, the experiments are carried out by reversing the direction of the motors on one side of the robot while keeping the speeds of all constant. In an ideal case, under this condition, a robot should turn about its COG without displacing in space. Figures 5.12 and 5.13 show the simulation and experimental results for tracking MinIAQ-I and MinIAQ-II's COG position

during 2.5 Hz turning, respectively. The results imply that the uncertainties in the experiments are difficult to predict or model such as the irregular movement of the actual robot for a short period of time in Figure 5.13. However, it is fairly acceptable to regard the simulation as a good measure of predicting the actual position, as the overall trend in turning behavior agrees between the two. It can also be inferred from the simulations that neither robot performs a zero-radius turn but a turning with relatively small radius of curvature.

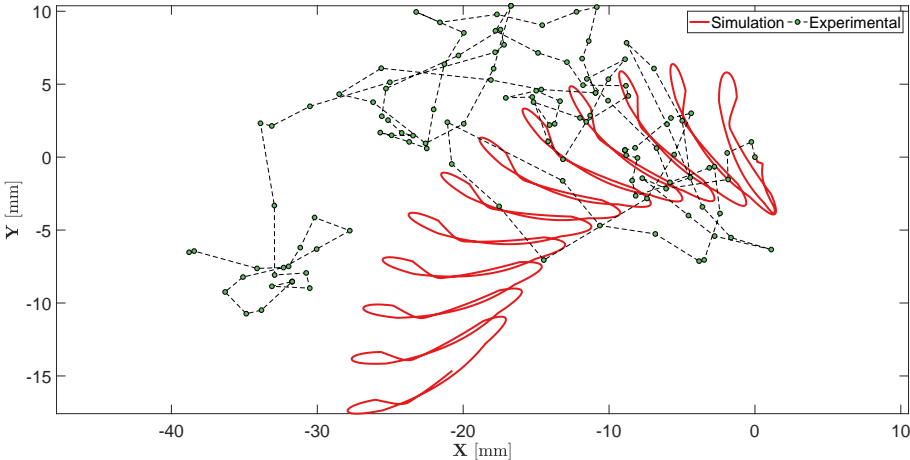


Figure 5.12: In-place turning trajectory verification for MinIAQ-I at 2.5 Hz.

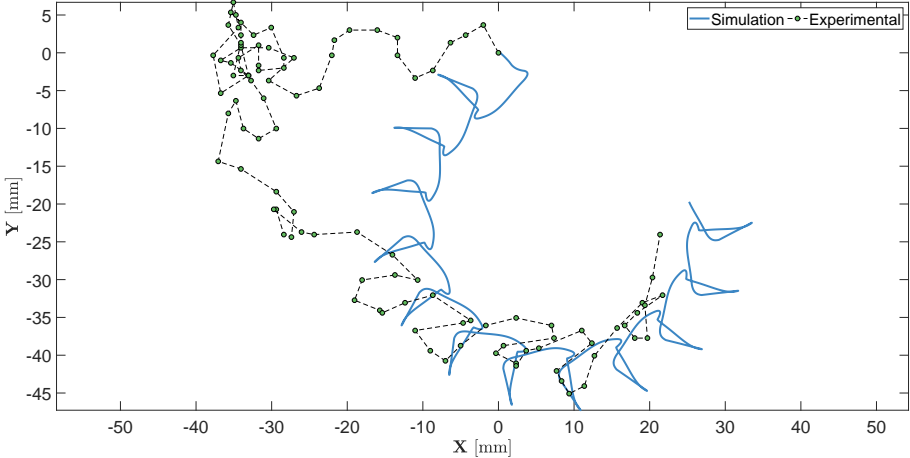


Figure 5.13: In-place turning trajectory verification for MinIAQ-II at 2.5 Hz.

The speed of rotation in turning tests can simply be measured from the variations in yaw angle, presented in Figures 5.14 and 5.15. The simulation results for both

robots closely match with the extracted yaw angles and the nearly linear trends in the plots suggest that the robots are capable of performing in-place turns at relatively constant speeds. The simulation and experimental data verify that MinIAQ-II is superior over its predecessor in almost every aspect, including in-place turning where it turns at a rate of more than 50 degrees per second, as opposed to MinIAQ-I which roughly turns at 20 degrees per second, for a motor speed of 2.5 Hz.

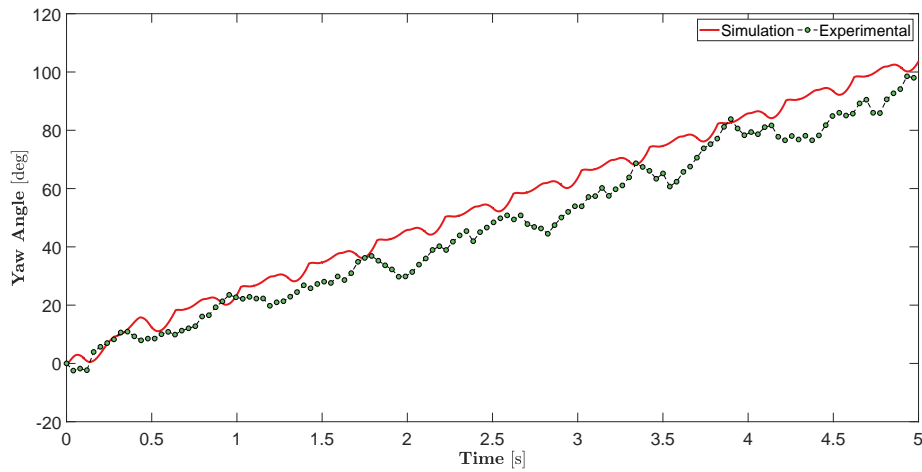


Figure 5.14: Yaw angle variation during in-place turning for MinIAQ-I at 2.5 Hz.

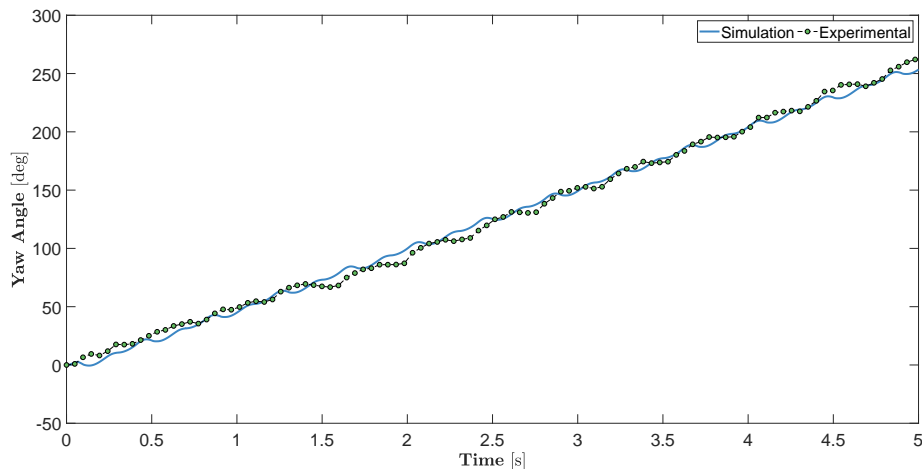


Figure 5.15: Yaw angle variation during in-place turning for MinIAQ-II at 2.5 Hz.

Chapter 6

Gait Analysis

6.1 The Gait Coordination Problem

The study of biological legged morphologies have led to realization that animals select their gaits, patterns of leg movement, according to speed. It is a proven fact that there is no general gait that can be employed for all locomotion speeds as efficient gaits for walking are extremely inefficient for running and vice versa [102]. Attracted to this phenomenon, many researchers have thoroughly investigated the locomotion transition patterns in creatures, most of which concern quadrupedal gaits inspired by four-legged animals [103]. These biological studies prepared the ground to seek for mathematical models and simulation tools in order to reveal the gait generation or transition behavior [104,105]. The findings of [106] led to understanding the underlying locomotive pattern generator in animals which is done through the so-called CPG (Central Pattern Generator) neural network. Since then, design of quadruped robots with modifiable locomotion patterns and spontaneous gait transition has widely been influenced by CPG controllers, examples of which are [107–111]. However, most of these works have addressed robots in large scale where identification of states and sensing the working environment through leg loading feedback [112] are more attainable.

A more comprehensive explanation to gaits is given by [113] where a gait is defined by “the time and the location of the placing and lifting of each foot, coordinated with the motion of the body in its six degrees of freedom, in order to move the body from one place to another”. The key concept in this definition is the coordination of a gait with the body motion. This means that for proper gait planning, the legs must be controlled for proper foot placement and lifting with respect to how the body is moving and interacting with the ground. The absence of any of these two factors, i.e. control on foot placement and/or realization of body movements, can lead to an unplanned walking in a robot, potentially with a different gait than intended. In small scale robotic platforms where actuation, sensing, and power are limited, gait planning through foot placement control is neither cost effective nor easily attainable. Thus, even though a desired gait is envisioned at the design phase, it is not known whether it is optimum or works as expected, once the robot is walking.

6.2 Envisioned Gait Performance

Figure 6.1 shows the convention used in numbering and labeling of MinIAQ’s legs. In order to investigate how closely the actual locomotion matches with the intended gait, gait diagrams for the validated trot and turning cases are presented for MinIAQ-II. In these diagrams (Figures 6.2 to 6.4), a forward force is shown with green color and a backward force is shown by red. Each gait diagram represents an ideal gait pattern along with an actual gait pattern. The gait diagram given in Figure 6.2 shows the pattern for gaits for 5 seconds of simulation. Note that as expected, the actual gait has a periodic repeating trend for each cycle. Due to this reason, examining the results for a single cycle is more practical and understandable.

In general, a gait diagram is used to describe the gait sequence of a multi-legged robot or animal [46]. The horizontal axis represents a normalized cycle time representation from 0 to 100%. The length of each horizontal bar defines the duty factor, which is the duration that a leg is in contact with the ground over

one stride cycle. In simple terms, if a leg is always dragged on the ground the duty cycle for that particular leg is 100%. Furthermore, the initiation of contact for each leg is called the relative phase and indicates the moment of touch-down.

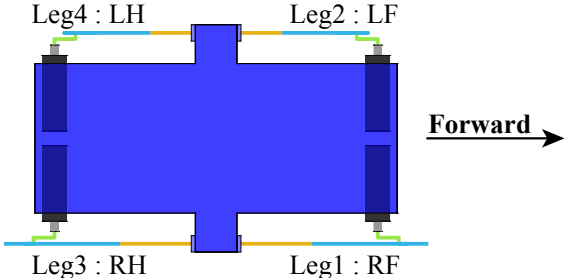


Figure 6.1: A schematic showing the convention used in labeling the legs. *R*, *L*, *F*, and *H* are abbreviations for Right, Left, Foreleg and Hind leg, respectively.

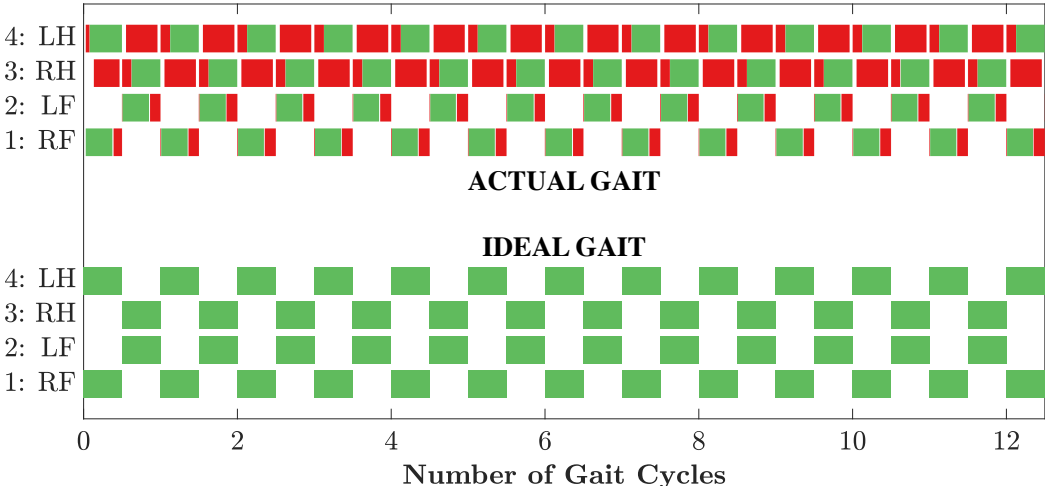


Figure 6.2: A complete trot gait diagram for MinIAQ-II, for a simulation of five seconds at 2.5 Hz, equivalent to 12.5 stride cycles. Since the actual gait is symmetric and periodic in time, representation of a single cycle would be enough.

Gaits are classified into two categories of walking or running patterns [103]. The distinction between the two groups is made by the duty factor. Walks are gait patterns where the duty factors are greater than 0.5 and for runs, this is less than 0.5. An ideal trot gait is defined by a duty factor of exactly 0.5 with each diagonal leg pair being in phase, and 180° phase apart with respect to each other. This is clearly shown by the ideal gait representation in Figure 6.3. Note that since ideally a robot does not want to drag its force on the ground to generate

a negative backward dissipative force, the ideal gait is represented by full green color.

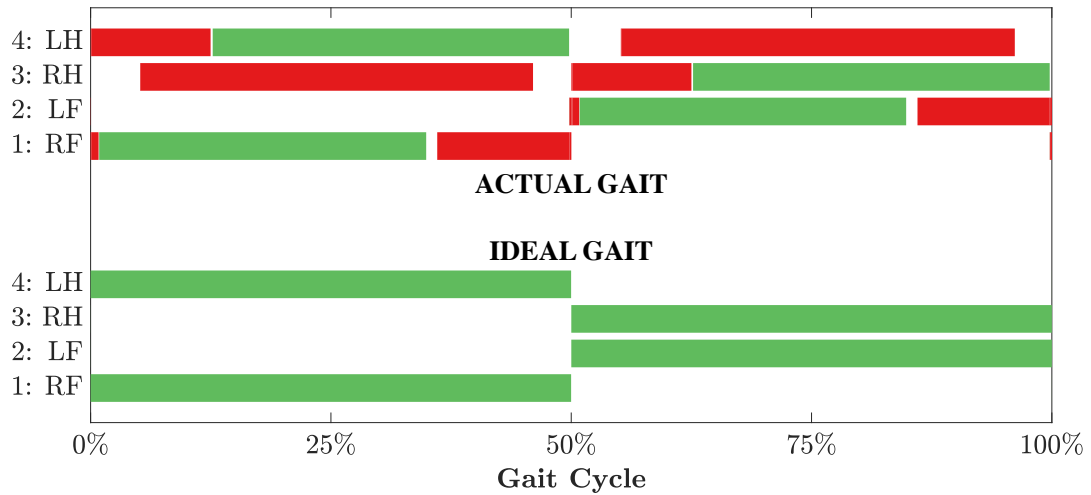


Figure 6.3: A single cycle trot gait diagram for MinIAQ-II, simulated at a motor speed of 2.5 Hz.

Recall that originally we envisioned the robot to trot, and designed the initial control algorithm to synchronize the legs based on an ideal trot gait sequence. However, despite the fact that MinIAQ-II performs fine in actual trot tests, it was clearly observed the robot does not conform to an ideal trot gait. As can be seen from the simulated gait diagram (Figure 6.3), the hind legs spend a lot of time being dragged on the surface as shown by red color. In fact, they barely ever leave the ground and the red portions are appearing mostly at points where they are supposed to be in the flight phase. Thus, it is very clearly shown how the model can predict the locomotion of the actual robot and signify the flaws in the gait diagram. Since MinIAQ is underactuated and has absolutely no control for foot placement, the model can serve as a tool to seek for a commanded gait pattern that can minimize the red regions.

Another interpretation from the plot can be made from counting the simultaneous number of legs touching. It is very clear that almost over the entire cycle, the robot is running on three legs, as opposed to the ideal trot gait where this is supposed to be only two at any instance. This observation suggests that the

robot is behaving more like a walking gait pattern with duty factor of greater than 0.5 where there are moments with touchdown of three legs. As a result, just for the proof of concept, a lateral slow walk (amble) gait pattern was selected and simulated at the same frequency of 2.5 Hz. Amble, which is a more efficient slow-pace gait pattern for walking in animals, is defined by an initial phase shift of $\begin{bmatrix} 0 & 0.5 & 0.75 & 0.25 \end{bmatrix}^\top$, whereas trot is defined by $\begin{bmatrix} 0 & 0.5 & 0.5 & 0 \end{bmatrix}^\top$ [103]. The simulation results highlighted the fact that a nearly 50% larger distance was covered by the lateral walk gait pattern than trot, at the same locomotion speed.

Figure 6.4 shows the ideal and actual turning gait diagrams for a motor frequency of 2.5 Hz. As can be seen, in the turning case where the direction of rotation of the motors on one side are reversed, it is ideally required to have the right legs generate a forward force and the left hand legs generate a negative force (of equal magnitude) along the body. This makes the robot to have no net force but a resulting moment causing it to rotate in place. Comparing the ideal and actual cases implies that the robot is again having three legs touching down at most of the times one of which is at least creating an undesired force. The result of this is of course a degradation in performance of turning as the undesired force causes the rotation effect to decelerate.

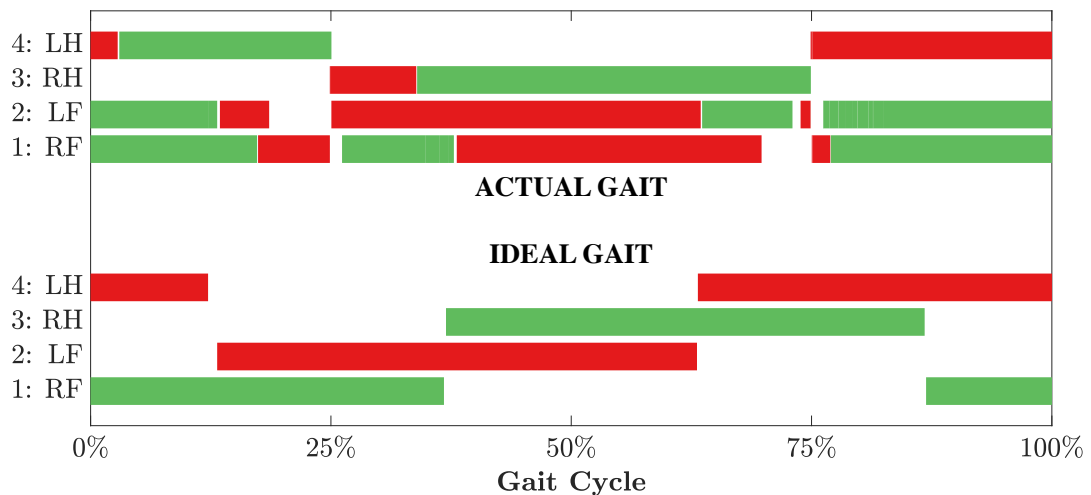


Figure 6.4: A single cycle turning gait diagram for MinIAQ-II, simulated at a motor speed of 2.5 Hz.

6.3 Quadrupedal Gaits Comparison

Following the analysis on the actual gaits used on the robot, a comprehensive investigation on the performance of alternative quadrupedal gaits, employed by animals, is done using the dynamic model. The gaits under study are shown in Table 6.1 which are ordered from slow walking gaits to fast running ones [111,114]. The tabulated values show the relative phase difference between the legs (motors) where the reference leg is taken as the right foreleg (RF). These gaits are run at 0 to 15 Hz motor speeds for MinIAQ-II and the robot’s locomotion performance is observed. The intended gaits, especially if they are slow gaits such as walk or trot, tend to fail at high speeds and make the robot rotate and behave unpredictably. Such a case is shown in Figure 6.5. In Figure 6.5(a), trot gait makes the robot move forward as desired at 2.5 Hz motor speed, however, the same gait makes the robot rotate and behave unstably at 11.5 Hz (Figure 6.5(b)).

Table 6.1: Motor Phases for Intended Quadrupedal Gaits of MinIAQ-II.

Gait	Right Foreleg	Left Foreleg	Right Hind-leg	Left Hind-leg
Walk	0°	180°	270°	90°
Trot	0°	180°	180°	0°
Pace	0°	180°	0°	180°
Canter	0°	288°	288°	180°
Pronk	0°	0°	0°	0°
Bound	0°	0°	180°	180°

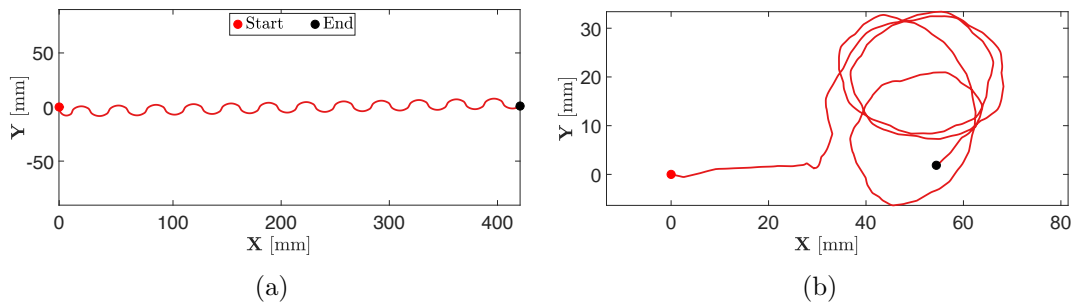


Figure 6.5: Trot gait simulation samples. Data shown is the center of gravity of the robot recorded from a top view at (a) 2.5 Hz and (b) 11.5 Hz motor speeds.

In order to compare the performances of different gaits run at different motor speeds, the speed along the inertial (global) x-direction is considered. The robot initially points to the x-direction and all the envisioned gaits are trying to move the robot forward. Therefore a high speed in x-direction would mean that the intended gait, even though it might not be the same as the actual gait, makes the robot move forward; hence, it is working. The simulations similar to the one shown in Figure 6.5(b) are removed from the data and the corresponding results are displayed in Figure 6.6.

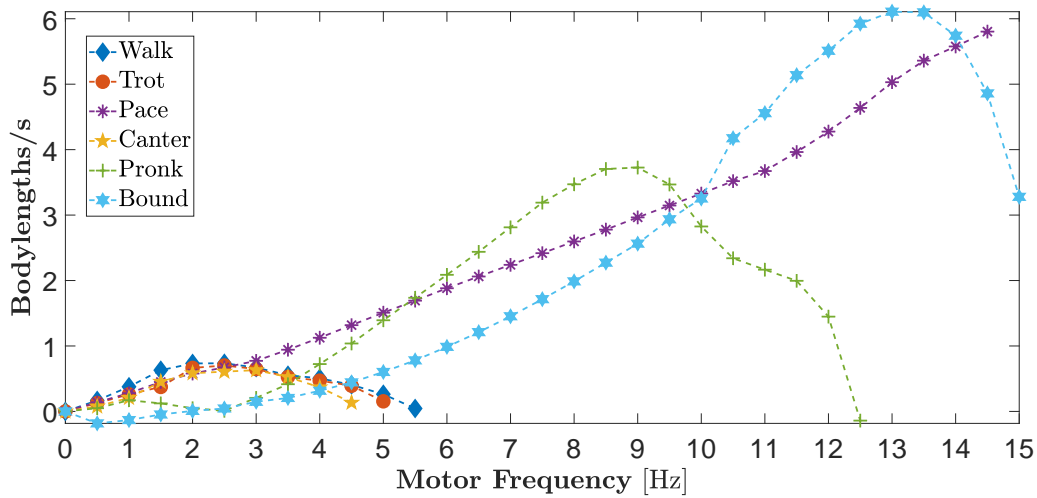


Figure 6.6: MinIAQ-II’s simulated locomotion performance on flat terrain for different intended quadrupedal gaits at different motor speeds.

The results show that slower pace gaits such as walk and trot dominate the slow speed locomotion, with walk being slightly better than the rest. These slow intended gaits work with a similar performance, up to approximately 5 Hz motor speed in MinIAQ-II with the best performance around 2.5 Hz. 4 Hz-9 Hz motor speed region is dominated by the pronk gait and after 9 Hz, bound gait tends to work the best. The pace gait works very well across all motor speeds; however, it should be noted here that the simulations are run for MinIAQ-II on flat terrain and some of the intended gaits (especially the pace gait) actually make the robot move with a stick-slip type motion where the feet never leaves the ground. So even though pace gait was very consistent, it might not be the most ideal gait for a robot under different terrain conditions.

The results presented here are a proof of concept for demonstrating how a gait can be interpreted in a miniature robot where there is no control on foot placement. It is important to state that the possibility of following an inverse approach in gait modification of these robots can be beneficial in optimizing the locomotion. That is, the validated dynamic model can be utilized to systematically analyze and optimize gaits specific to a robot, through an evolutionary optimization scheme, such as Genetic algorithm. However, this is still not properly done for MinIAQ as the gait analysis of the robot is at its preliminary stage.

Chapter 7

Conclusion and Future Work

This thesis is an overall study of designing, controlling, dynamic modeling, and analyzing gaits in an origami-inspired miniature quadruped robot. The robot under study is called MinIAQ which utilizes origami-inspired fabrication, exhibits high structural integrity, and enables performing gait analysis due to having four independent actuators (one per each leg). MinIAQ can serve as a paradigm for designing complex foldable structures and helps modulate and extend the design standards of origami robots. More importantly, since robots with high degrees of freedom do not exist much in miniature scale, it can be used as a platform to properly study and examine locomotion behaviors at small scale. The dimensional synthesis of the four-bar leg mechanism of MinIAQ is proven to be a reliable optimization technique for compliant mechanisms. The optimized version of the robot walks faster and exhibits much better stability compared to its predecessor. This is simply achieved by altering the coupler link of the robot into a knee-shaped link whose novel unfolded crease pattern can be utilized in design of other foldable robots. The proposed dynamic model of the robot can closely predict the actual locomotion trends of MinIAQ on flat terrain. This model can be used to extract the missing elements for gait studies in miniature robotics where there is generally no control on feet placement or realization of the system states. Examining the gait diagrams obtained from the model gives an insight into selecting better gait patterns.

While there are many ways to extend the work presented herein, it should be pointed out that the gait analysis framework is still in its infancy phase. One possible approach to studying gaits in miniature robots can be to utilize the model in conjunction with evolutionary algorithm techniques, such as Genetic Algorithm, to inversely seek for an optimized gait pattern. Alternatively, one can use the simulation GUI to explore the performance of existing quadruped gaits for a conceptual design of a robot; so as to determine a proper locomotion pattern prior to designing the actual robot. Other means of extending the work can be to develop the dynamic model further to account for large angle beam theories in modeling of compliant mechanisms. Also, prediction of the motion of a robot on rough terrain is another interesting field of research that can be easily done through modifying the model.

Bibliography

- [1] C. Karakadioğlu, M. Askari, and O. Özcan, “Design and operation of miniaq: An untethered foldable miniature quadruped with individually actuated legs,” in *2017 IEEE International Conference on Advanced Intelligent Mechatronics (AIM)*, pp. 247–252, IEEE, 2017.
- [2] M. Askari, C. Karakadioğlu, F. Ayhan, and O. Özcan, “Miniaq-ii: A miniature foldable quadruped with an improved leg mechanism,” in *2017 IEEE International Conference on Robotics and Biomimetics (ROBIO)*, IEEE, 2017.
- [3] O. Ozcan, A. T. Baisch, D. Ithier, and R. J. Wood, “Powertrain selection for a biologically-inspired miniature quadruped robot,” in *2014 IEEE International Conference on Robotics and Automation (ICRA)*, pp. 2398–2405, IEEE, 2014.
- [4] A. M. Mehta and D. Rus, “An end-to-end system for designing mechanical structures for print-and-fold robots,” in *2014 IEEE International Conference on Robotics and Automation (ICRA)*, pp. 1460–1465, IEEE, 2014.
- [5] E. Shimada, J. Thompson, J. Yan, R. Wood, and R. Fearing, “Prototyping millirobots using dextrous microassembly and folding,” *Proc. ASME IMECE/DSCD*, vol. 69, no. 2, pp. 933–940, 2000.
- [6] P. Birkmeyer, K. Peterson, and R. S. Fearing, “Dash: A dynamic 16g hexapedal robot,” in *Intelligent Robots and Systems, 2009. IROS 2009. IEEE/RSJ International Conference on*, pp. 2683–2689, IEEE, 2009.

- [7] R. Wood, S. Avadhanula, R. Sahai, E. Steltz, and R. Fearing, “Microrobot design using fiber reinforced composites,” *Journal of Mechanical Design*, vol. 130, no. 5, p. 052304, 2008.
- [8] A. M. Hoover, E. Steltz, and R. S. Fearing, “Roach: An autonomous 2.4 g crawling hexapod robot,” in *Intelligent Robots and Systems, 2008. IROS 2008. IEEE/RSJ International Conference on*, pp. 26–33, IEEE, 2008.
- [9] A. O. Pullin, N. J. Kohut, D. Zarrouk, and R. S. Fearing, “Dynamic turning of 13 cm robot comparing tail and differential drive,” in *Robotics and Automation (ICRA), 2012 IEEE International Conference on*, pp. 5086–5093, IEEE, 2012.
- [10] K. L. Hoffman and R. J. Wood, “Myriapod-like ambulation of a segmented microrobot,” *Autonomous Robots*, vol. 31, no. 1, p. 103, 2011.
- [11] A. T. Baisch, O. Ozcan, B. Goldberg, D. Ithier, and R. J. Wood, “High speed locomotion for a quadrupedal microrobot,” *The International Journal of Robotics Research*, vol. 33, no. 8, pp. 1063–1082, 2014.
- [12] Y. Sun, S. Song, X. Liang, and H. Ren, “A miniature soft robotic manipulator based on novel fabrication methods,” *IEEE Robotics and Automation Letters*, vol. 1, no. 2, pp. 617–623, 2016.
- [13] J. E. Rajkowski, A. P. Gerratt, E. W. Schaler, and S. Bergbreiter, “A multi-material milli-robot prototyping process,” in *Intelligent Robots and Systems, 2009. IROS 2009. IEEE/RSJ International Conference on*, pp. 2777–2782, IEEE, 2009.
- [14] R. S. Pierre and S. Bergbreiter, “Gait exploration of sub-2 g robots using magnetic actuation,” *IEEE Robotics and Automation Letters*, vol. 2, pp. 34–40, Jan 2017.
- [15] J. Rossiter and S. Sareh, “Kirigami design and fabrication for biomimetic robotics,” in *SPIE Smart Structures and Materials+ Nondestructive Evaluation and Health Monitoring*, pp. 90550G–90550G, International Society for Optics and Photonics, 2014.

- [16] C. D. Onal, R. J. Wood, and D. Rus, “Towards printable robotics: Origami-inspired planar fabrication of three-dimensional mechanisms,” in *Robotics and Automation (ICRA), 2011 IEEE International Conference on*, pp. 4608–4613, IEEE, 2011.
- [17] R. MacCurdy, R. Katzschmann, Y. Kim, and D. Rus, “Printable hydraulics: a method for fabricating robots by 3d co-printing solids and liquids,” in *Robotics and Automation (ICRA), 2016 IEEE International Conference on*, pp. 3878–3885, IEEE, 2016.
- [18] A. M. Hoover and R. S. Fearing, “Fast scale prototyping for folded millirobots,” in *Robotics and Automation, 2008. ICRA 2008. IEEE International Conference on*, pp. 886–892, Ieee, 2008.
- [19] M. Salerno, K. Zhang, A. Menciassi, and J. S. Dai, “A novel 4-dof origami grasper with an sma-actuation system for minimally invasive surgery,” *IEEE Transactions on Robotics*, 2016.
- [20] E. Vander Hoff, D. Jeong, and K. Lee, “Origamibot-i: A thread-actuated origami robot for manipulation and locomotion,” in *2014 IEEE/RSJ International Conference on Intelligent Robots and Systems*, pp. 1421–1426, IEEE, 2014.
- [21] Y. Mulgaonkar, B. Araki, J.-s. Koh, L. Guerrero-Bonilla, D. M. Aukes, A. Makineni, M. T. Tolley, D. Rus, R. J. Wood, and V. Kumar, “The flying monkey: A mesoscale robot that can run, fly, and grasp,” in *2016 IEEE International Conference on Robotics and Automation (ICRA)*, pp. 4672–4679, IEEE, 2016.
- [22] C. D. Onal, R. J. Wood, and D. Rus, “An origami-inspired approach to worm robots,” *IEEE/ASME Transactions on Mechatronics*, vol. 18, no. 2, pp. 430–438, 2013.
- [23] K. Zhang, C. Qiu, and J. S. Dai, “Helical kirigami-enabled centimeter-scale worm robot with shape-memory-alloy linear actuators,” *Journal of Mechanisms and Robotics*, vol. 7, no. 2, p. 021014, 2015.

- [24] C. D. Onal, M. T. Tolley, R. J. Wood, and D. Rus, “Origami-inspired printed robots,” *IEEE/ASME Transactions on Mechatronics*, vol. 20, no. 5, pp. 2214–2221, 2015.
- [25] M. Agheli, S. G. Faal, F. Chen, H. Gong, and C. D. Onal, “Design and fabrication of a foldable hexapod robot towards experimental swarm applications,” in *2014 IEEE International Conference on Robotics and Automation (ICRA)*, pp. 2971–2976, IEEE, 2014.
- [26] S. T. Kalat, S. G. Faal, U. Celik, and C. D. Onal, “Tribot: A minimally-actuated accessible holonomic hexapedal locomotion platform,” in *Intelligent Robots and Systems (IROS), 2015 IEEE/RSJ International Conference on*, pp. 6292–6297, IEEE, 2015.
- [27] S. Felton, M. Tolley, E. Demaine, D. Rus, and R. Wood, “A method for building self-folding machines,” *Science*, vol. 345, no. 6197, pp. 644–646, 2014.
- [28] Z. Zhakypov and J. Paik, “Design methodology for constructing multimaterial origami robots and machines,” *IEEE Transactions on Robotics*, vol. 34, no. 1, pp. 151–165, 2018.
- [29] K. L. Hoffman, “Design and locomotion studies of a miniature centipede-inspired robot,” 2013.
- [30] S. G. Faal, F. Chen, W. Tao, M. Agheli, S. Tasdighikalat, and C. D. Onal, “Hierarchical kinematic design of foldable hexapedal locomotion platforms,” *Journal of Mechanisms and Robotics*, vol. 8, no. 1, p. 011005, 2016.
- [31] L. L. Howell, *Compliant mechanisms*. John Wiley & Sons, 2001.
- [32] L. U. Odhner and A. M. Dollar, “The smooth curvature flexure model: An accurate, low-dimensional approach for robot analysis,” *Proc. Robot.: Sci. Syst. VI*, pp. 137–144, 2010.
- [33] C. Sung and D. Rus, “Foldable joints for foldable robots,” *Journal of Mechanisms and Robotics*, vol. 7, no. 2, p. 021012, 2015.

- [34] E. Söylemez, *Mechanisms*. Middle East Technical University, 1979.
- [35] J. J. Uicker, G. R. Pennock, J. E. Shigley, *et al.*, *Theory of machines and mechanisms*, vol. 1. Oxford University Press New York, NY, 2011.
- [36] K. Bisshopp and D. Drucker, “Large deflection of cantilever beams,” *Quarterly of Applied Mathematics*, vol. 3, no. 3, pp. 272–275, 1945.
- [37] K. Mattiasson, “Numerical results from large deflection beam and frame problems analysed by means of elliptic integrals,” *International journal for numerical methods in engineering*, vol. 17, no. 1, pp. 145–153, 1981.
- [38] A. Zhang and G. Chen, “A comprehensive elliptic integral solution to the large deflection problems of thin beams in compliant mechanisms,” *Journal of Mechanisms and Robotics*, vol. 5, no. 2, p. 021006, 2013.
- [39] J. Cabrera, A. Simon, and M. Prado, “Optimal synthesis of mechanisms with genetic algorithms,” *Mechanism and Machine theory*, vol. 37, no. 10, pp. 1165–1177, 2002.
- [40] A. Kunjur and S. Krishnamurty, “Genetic algorithms in mechanism synthesis,” *Journal of Applied Mechanisms and Robotics*, vol. 4, no. 2, pp. 18–24, 1997.
- [41] A. Shinde, S. Kulkarni, and S. Shete, “Dimensional synthesis of mechanism using genetic algorithm,” *International Journal of Current Engineering and Technology*, 2017.
- [42] K. Manickavelan, B. Singh, and N. Sellappan, “Design, fabrication and analysis of four bar walking machine based on chebyshev’s parallel motion mechanism,” *European International Journal of Science and Technology*, vol. 3, no. 8, 2014.
- [43] W.-B. Shieh, L.-W. Tsai, and S. Azarm, “Design and optimization of a one-degree-of-freedom six-bar leg mechanism for a walking machine,” *Journal of Robotic systems*, vol. 14, no. 12, pp. 871–880, 1997.
- [44] N. Lokhande and V. Emche, “Mechanical spider by using klann mechanism,” *IJMCA*, vol. 1, no. 5, pp. 013–016, 2013.

- [45] R. H. Byrd, M. E. Hribar, and J. Nocedal, “An interior point algorithm for large-scale nonlinear programming,” *SIAM Journal on Optimization*, vol. 9, no. 4, pp. 877–900, 1999.
- [46] S. Kajita and B. Espiau, “Legged robots,” in *Springer handbook of robotics*, pp. 361–389, Springer, 2008.
- [47] R. L. Boylestad, L. Nashelsky, and L. Li, *Electronic devices and circuit theory*, vol. 11. Prentice Hall Englewood Cliffs, NJ, 2002.
- [48] G. Casiez, N. Roussel, and D. Vogel, “1€ filter: a simple speed-based low-pass filter for noisy input in interactive systems,” in *Proceedings of the SIGCHI Conference on Human Factors in Computing Systems*, pp. 2527–2530, ACM, 2012.
- [49] I. Bilinskis, *Digital alias-free signal processing*. John Wiley & Sons, 2007.
- [50] G. F. Franklin, J. D. Powell, A. Emami-Naeini, and J. D. Powell, *Feedback control of dynamic systems*, vol. 3. Addison-Wesley Reading, MA, 1994.
- [51] R. C. Dorf and R. H. Bishop, *Modern control systems*. Pearson, 2011.
- [52] P. Holmes, R. J. Full, D. Koditschek, and J. Guckenheimer, “The dynamics of legged locomotion: Models, analyses, and challenges,” *SIAM review*, vol. 48, no. 2, pp. 207–304, 2006.
- [53] D. I. Goldman, T. S. Chen, D. M. Dudek, and R. J. Full, “Dynamics of rapid vertical climbing in cockroaches reveals a template,” *Journal of Experimental Biology*, vol. 209, no. 15, pp. 2990–3000, 2006.
- [54] R. J. Full and M. S. Tu, “Mechanics of a rapid running insect: two-, four- and six-legged locomotion,” *Journal of Experimental Biology*, vol. 156, no. 1, pp. 215–231, 1991.
- [55] R. J. Full, R. Blickhan, and L. Ting, “Leg design in hexapedal runners,” *Journal of Experimental Biology*, vol. 158, no. 1, pp. 369–390, 1991.

- [56] R. Blickhan and R. Full, “Similarity in multilegged locomotion: bouncing like a monopode,” *Journal of Comparative Physiology A*, vol. 173, no. 5, pp. 509–517, 1993.
- [57] L. Ting, R. Blickhan, and R. J. Full, “Dynamic and static stability in hexapedal runners.,” *Journal of Experimental Biology*, vol. 197, no. 1, pp. 251–269, 1994.
- [58] D. L. Jindrich and R. J. Full, “Many-legged maneuverability: dynamics of turning in hexapods,” *Journal of experimental biology*, vol. 202, no. 12, pp. 1603–1623, 1999.
- [59] D. L. Hu, B. Chan, and J. W. Bush, “The hydrodynamics of water strider locomotion,” *Nature*, vol. 424, no. 6949, p. 663, 2003.
- [60] A. Parness, D. Soto, N. Esparza, N. Gravish, M. Wilkinson, K. Autumn, and M. Cutkosky, “A microfabricated wedge-shaped adhesive array displaying gecko-like dynamic adhesion, directionality and long lifetime,” *Journal of the Royal Society Interface*, pp. rsif-2009, 2009.
- [61] S. Hu, S. Lopez, P. H. Niewiarowski, and Z. Xia, “Dynamic self-cleaning in gecko setae via digital hyperextension,” *Journal of The Royal Society Interface*, vol. 9, no. 76, pp. 2781–2790, 2012.
- [62] M. P. Murphy and M. Sitti, “Waalbot: An agile small-scale wall-climbing robot utilizing dry elastomer adhesives,” *IEEE/ASME transactions on Mechatronics*, vol. 12, no. 3, pp. 330–338, 2007.
- [63] G. A. Lynch, J. E. Clark, P.-C. Lin, and D. E. Koditschek, “A bioinspired dynamical vertical climbing robot,” *The International Journal of Robotics Research*, vol. 31, no. 8, pp. 974–996, 2012.
- [64] T. Madani and A. Benallegue, “Backstepping sliding mode control applied to a miniature quadrotor flying robot,” in *IEEE Industrial Electronics, IECON 2006-32nd Annual Conference on*, pp. 700–705, IEEE, 2006.
- [65] H. S. Park, S. Floyd, and M. Sitti, “Dynamic modeling and analysis of pitch motion of a basilisk lizard inspired quadruped robot running on water,” in

- Robotics and Automation, 2009. ICRA '09. IEEE International Conference on*, pp. 2655–2660, IEEE, 2009.
- [66] Y. S. Song and M. Sitti, “Surface-tension-driven biologically inspired water strider robots: Theory and experiments,” *IEEE Transactions on robotics*, vol. 23, no. 3, pp. 578–589, 2007.
- [67] M. M. Bohra and M. R. Emami, “An evolutionary approach to feline rover gait planning,” in *Robotics and Biomimetics (ROBIO), 2014 IEEE International Conference on*, pp. 767–772, IEEE, 2014.
- [68] M. H. Raibert, *Legged robots that balance*. MIT press, 1986.
- [69] U. Saranlı, Ö. Arslan, M. M. Ankaralı, and Ö. Morgül, “Approximate analytic solutions to non-symmetric stance trajectories of the passive spring-loaded inverted pendulum with damping,” *Nonlinear Dynamics*, vol. 62, no. 4, pp. 729–742, 2010.
- [70] U. Saranlı, W. J. Schwind, and D. E. Koditschek, “Toward the control of a multi-jointed, monoped runner,” in *Robotics and Automation, 1998. Proceedings. 1998 IEEE International Conference on*, vol. 3, pp. 2676–2682, IEEE, 1998.
- [71] A. Sato and M. Buehler, “A planar hopping robot with one actuator: design, simulation, and experimental results,” in *Intelligent Robots and Systems, 2004. (IROS 2004). Proceedings. 2004 IEEE/RSJ International Conference on*, vol. 4, pp. 3540–3545, IEEE, 2004.
- [72] U. Saranlı, M. Buehler, and D. E. Koditschek, “Rhex: A simple and highly mobile hexapod robot,” *The International Journal of Robotics Research*, vol. 20, no. 7, pp. 616–631, 2001.
- [73] A. Spröwitz, A. Tuleu, M. Vespignani, M. Ajallooeian, E. Badri, and A. J. Ijspeert, “Towards dynamic trot gait locomotion: Design, control, and experiments with cheetah-cub, a compliant quadruped robot,” *The International Journal of Robotics Research*, vol. 32, no. 8, pp. 932–950, 2013.

- [74] S.-H. Hyon and T. Mita, “Development of a biologically inspired hopping robot-” kenken”,” in *Robotics and Automation, 2002. Proceedings. ICRA ’02. IEEE International Conference on*, vol. 4, pp. 3984–3991, IEEE, 2002.
- [75] I. Poulakakis, J. A. Smith, and M. Buchler, “Experimentally validated bounding models for the scout ii quadrupedal robot,” in *Robotics and Automation, 2004. Proceedings. ICRA’04. 2004 IEEE International Conference on*, vol. 3, pp. 2595–2600, IEEE, 2004.
- [76] D. Gong, P. Wang, S. Zhao, L. Du, and Y. Duan, “Bionic quadruped robot dynamic gait control strategy based on twenty degrees of freedom,” *IEEE/CAA Journal of Automatica Sinica*, vol. 5, no. 1, pp. 382–388, 2018.
- [77] M. Bennani and F. Giri, “Dynamic modelling of a four-legged robot,” *Journal of Intelligent and Robotic Systems*, vol. 17, no. 4, pp. 419–428, 1996.
- [78] E. Steltz, M. Seeman, S. Avadhanula, and R. S. Fearing, “Power electronics design choice for piezoelectric microrobots,” in *Intelligent Robots and Systems, 2006 IEEE/RSJ International Conference on*, pp. 1322–1328, IEEE, 2006.
- [79] K. S. Fu, R. Gonzalez, and C. G. Lee, *Robotics: Control Sensing. Vis.* Tata McGraw-Hill Education, 1987.
- [80] J. J. Craig, *Introduction to robotics: mechanics and control*, vol. 3. Pearson/Prentice Hall Upper Saddle River, NJ, USA:, 2005.
- [81] M. W. Spong and M. Vidyasagar, *Robot dynamics and control*. John Wiley & Sons, 2008.
- [82] P.-B. Wieber, R. Tedrake, and S. Kuindersma, “Modeling and control of legged robots,” in *Springer handbook of robotics*, pp. 1203–1234, Springer, 2016.
- [83] B. L. Stevens, F. L. Lewis, and E. N. Johnson, *Aircraft control and simulation: dynamics, controls design, and autonomous systems*. John Wiley & Sons, 2015.

- [84] D. A. Caughey, “Introduction to aircraft stability and control course notes for m&ae 5070,” *Sibley School of Mechanical & Aerospace Engineering, Cornell University, Ithaca, New York*, pp. 14853–7501, 2011.
- [85] B. Etkin and L. D. Reid, *Dynamics of flight: stability and control*, vol. 3. Wiley New York, 1996.
- [86] L. V. Schmidt, *Introduction to aircraft flight dynamics*. American Institute of Aeronautics and Astronautics, 1998.
- [87] H. Hertz, “Über die berührung fester elastischer körper. on the contact of elastic solids, reine und angewandte mathematik. london:(instruction anglaise dans miscellaneous papers by h. hertz) eds jones et schaott,” 1896.
- [88] W. Goldsmith, *The Theory and Physical Behaviour of Colliding Solids*. Dover Publ., 1999.
- [89] M. S. Shourijeh and J. McPhee, “Foot–ground contact modeling within human gait simulations: from kelvin–voigt to hyper-volumetric models,” *Multibody System Dynamics*, vol. 35, no. 4, pp. 393–407, 2015.
- [90] P. Flores and H. M. Lankarani, *Contact force models for multibody dynamics*, vol. 226. Springer, 2016.
- [91] K. H. Hunt and F. R. E. Crossley, “Coefficient of restitution interpreted as damping in vibroimpact,” *Journal of applied mechanics*, vol. 42, no. 2, pp. 440–445, 1975.
- [92] W. J. Stronge, “Rigid body collisions with friction,” *Proc. R. Soc. Lond. A*, vol. 431, no. 1881, pp. 169–181, 1990.
- [93] M. Wojtyra, “Multibody simulation model of human walking,” *Mechanics Based Design of Structures and Machines*, 2003.
- [94] S. Frimpong and M. Thiruvengadam, “Contact and joint forces modeling and simulation of crawler-formation interactions,” *J. Powder Metall. Min.*, vol. 4, p. 135, 2015.

- [95] J. Keller, “Impact with friction,” *Journal of applied Mechanics*, vol. 53, no. 1, pp. 1–4, 1986.
- [96] W. Stronge, “Smooth dynamics of oblique impact with friction,” *International journal of impact engineering*, vol. 51, pp. 36–49, 2013.
- [97] D. Negrut and A. Dyer, “Adams/solver primer,” *MSC. Software Documentation, Ann Arbor*, 2004.
- [98] E. O. Filippova, A. V. Filippov, and I. A. Shulepov, “Experimental study of sliding friction for pet track membranes,” in *IOP Conference Series: Materials Science and Engineering*, vol. 125, p. 012020, IOP Publishing, 2016.
- [99] E. Hairer and G. Wanner, “Solving ordinary differential equations ii: Stiff and differential-algebraic problems second revised edition with 137 figures,” *Springer Series in Computational Mathematics*, vol. 14, 1996.
- [100] L. F. Shampine and M. W. Reichelt, “The matlab ode suite,” *SIAM journal on scientific computing*, vol. 18, no. 1, pp. 1–22, 1997.
- [101] C. W. Gear, “The numerical integration of ordinary differential equations,” *Mathematics of Computation*, vol. 21, no. 98, pp. 146–156, 1967.
- [102] M. Hildebrand, “Symmetrical gaits of horses,” *Science*, vol. 150, no. 3697, pp. 701–708, 1965.
- [103] R. M. Alexander, “The gaits of bipedal and quadrupedal animals,” *The International Journal of Robotics Research*, vol. 3, no. 2, pp. 49–59, 1984.
- [104] S. Ito, H. Yuasa, Z.-w. Luo, M. Ito, and D. Yanagihara, “A mathematical model of adaptive behavior in quadruped locomotion,” *Biological cybernetics*, vol. 78, no. 5, pp. 337–347, 1998.
- [105] S. Aoi, T. Yamashita, and K. Tsuchiya, “Hysteresis in the gait transition of a quadruped investigated using simple body mechanical and oscillator network models,” *Physical Review E*, vol. 83, no. 6, p. 061909, 2011.

- [106] M. L. Shik, “Control of walking and running by means of electrical stimulation of the midbrain,” *Biophysics*, vol. 11, pp. 659–666, 1966.
- [107] K. Tsujita, K. Tsuchiya, and A. Onat, “Adaptive gait pattern control of a quadruped locomotion robot,” in *Intelligent Robots and Systems, 2001. Proceedings. 2001 IEEE/RSJ International Conference on*, vol. 4, pp. 2318–2325, IEEE, 2001.
- [108] S. Rutishauser, A. Sprowitz, L. Righetti, and A. J. Ijspeert, “Passive compliant quadruped robot using central pattern generators for locomotion control,” in *Biomedical Robotics and Biomechanics, 2008. BioRob 2008. 2nd IEEE RAS & EMBS International Conference on*, pp. 710–715, IEEE, 2008.
- [109] Y. Fukuoka and H. Kimura, “Dynamic locomotion of a biomorphic quadruped ‘tekken’ robot using various gaits: walk, trot, free-gait and bound,” *Applied Bionics and Biomechanics*, vol. 6, no. 1, pp. 63–71, 2009.
- [110] C. P. Santos and V. Matos, “Gait transition and modulation in a quadruped robot: A brainstem-like modulation approach,” *Robotics and Autonomous Systems*, vol. 59, no. 9, pp. 620–634, 2011.
- [111] D. Owaki and A. Ishiguro, “A quadruped robot exhibiting spontaneous gait transitions from walking to trotting to galloping,” *Scientific reports*, vol. 7, no. 1, p. 277, 2017.
- [112] Y. Fukuoka, Y. Habu, and T. Fukui, “A simple rule for quadrupedal gait generation determined by leg loading feedback: a modeling study,” *Scientific reports*, vol. 5, p. 8169, 2015.
- [113] S.-M. Song and K. J. Waldron, *Machines that walk: the adaptive suspension vehicle*. MIT press, 1989.
- [114] J. J. Collins and I. N. Stewart, “Coupled nonlinear oscillators and the symmetries of animal gaits,” *Journal of Nonlinear Science*, vol. 3, no. 1, pp. 349–392, 1993.

Appendix A

Geometrical Considerations in Foldable Mechanism Design

In designing origami robots, close examination of the correlations between 2D unfolded structure and final 3D geometry is a necessity. It is very important how a planar mechanism with ideal pin joints is transformed to a foldable compliant mechanism, and vice versa. This requires careful consideration of the crease pattern geometry and failure to do so can result in a poor final design.

In the following sections, two opposite cases are presented regarding geometrical considerations in designing and modeling of MinIAQ-II. It should be emphasized that a similar approach can be generalized to the analysis of any other planar foldable mechanism. In Appendix A.1, it is assumed that a four-bar mechanism with a non-straight link (optimized MinIAQ-II leg: Section 2.4.1), needs to be transformed into an unfolded 2D design. In the second case scenario, the opposite is studied; where Appendix A.2 outlines the procedure to convert an already designed foldable linkage into a planar mechanism with ideal pin joints, which can come in handy for kinematic modeling of an existing robot's leg (Section 4.3).

Note that the schematic representations of MinIAQ-II's leg geometry, shown in Figures A.1 and A.2, are commonly used for the in-depth analysis of both cases.

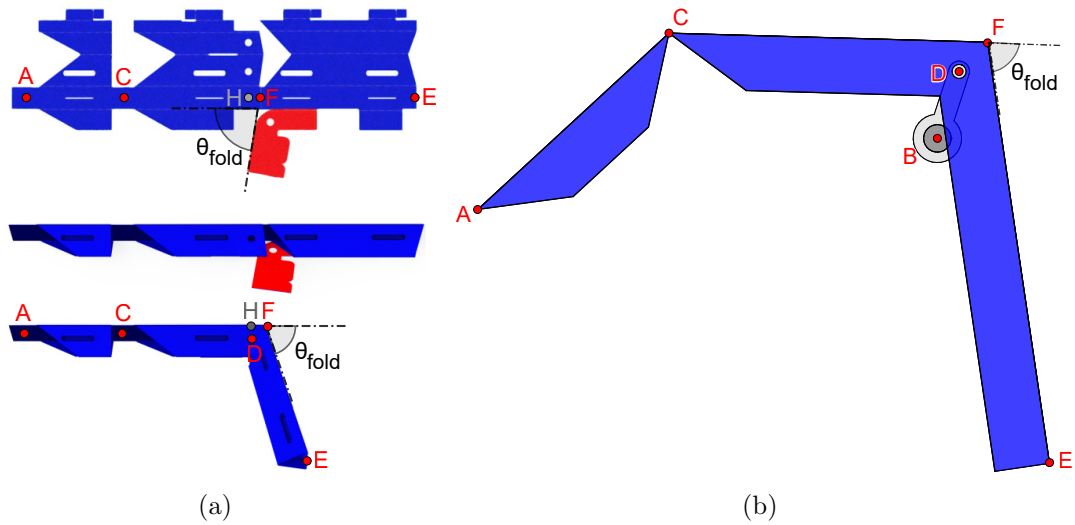


Figure A.1: (a) Unfolded MinIAQ-II compliant mechanism where link lengths are measured between the midpoints of the flexure joints (b) Assembled leg.

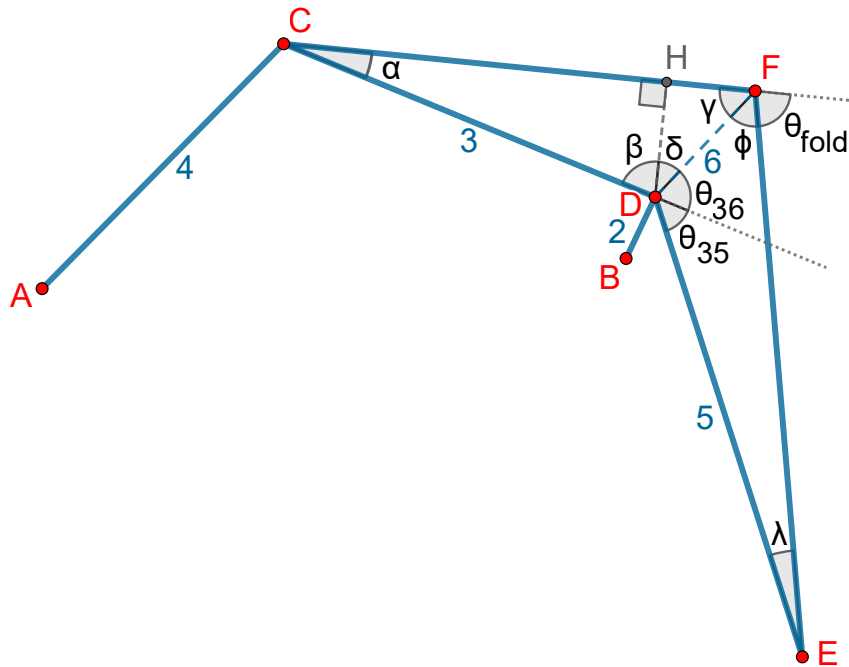


Figure A.2: Schematic diagram of a fully assembled leg with detail analysis of the non-straight knee-shaped link geometry. $ABCD$ is the actual actuating four-bar. Point E , which is fixed to the coupler link CD (link 3), is the tip of the foot whose trajectory is optimized for proper walking. The knee-shaped link is not drawn to scale for better visualization.

A.1 Ideal Mechanism to Foldable Leg Design

This section presents the procedure to design the crease pattern based on an ideal four-bar mechanism with revolute joints. Following a similar approach to optimization of a four-bar leg linkage discussed in Section 2.4.1, an optimum solution can be found. This solution is basically defined in terms of the planar coordinates of the joints: A , B , C , D , and E , for one particular instantaneous configuration of the mechanism (see Figure A.2). In other words, the known geometric parameters are the link lengths: l_2 , l_3 , l_4 , l_5 , and the fixed angle between links 3 and 5, θ_{35} . When designing the compliant leg mechanism, the designer is free to choose reasonable values for DH and HF lengths, such as in MinIAQ-II where these are selected as 2.5 mm and 2.0 mm, respectively.

Known Parameters: BD , AC , CD , DE , DH , HF , θ_{35}

Goal: To find the fixed-lock folding angle θ_{fold} (Figure A.1).

$$DF = \sqrt{DH^2 + HF^2}$$

$$\alpha = \arcsin\left(\frac{DH}{CD}\right)$$

$$\delta = \arctan\left(\frac{HF}{DH}\right)$$

$$\beta = 90^\circ - \alpha$$

$$\gamma = 90^\circ - \delta$$

$$\theta_{36} = 180^\circ - \beta - \delta$$

Using sine and cosine rules in $\triangle DEF$,

$$FE^2 = DE^2 + DF^2 - 2 \cdot DE \cdot DF \cdot \cos(\theta_{35} + \theta_{36})$$

$$\frac{DE}{\sin(\phi)} = \frac{FE}{\sin(\theta_{35} + \theta_{36})} = \frac{DF}{\sin(\lambda)}$$

We have,

$$FE = \sqrt{DE^2 + DF^2 - 2 \cdot DE \cdot DF \cdot \cos(\theta_{35} + \theta_{36})}$$

$$\phi = \arcsin\left(\frac{\sin(\theta_{35} + \theta_{36})}{FE} \cdot DE\right)$$

$$\theta_{fold} = 180^\circ - \phi - \gamma$$

A.2 Mechanism Modeling from a Foldable Leg

In this section, it is assumed that a foldable leg is designed initially without enough care for the errors that are introduced by disregarding the geometrical constraints of foldable structures. Alternatively, this can be thought of as a case where a crease pattern of a mechanism, such as MinIAQ-II's leg in Figure A.1(a), is given; and the idea is to model its actual four-bar linkage by taking geometrical considerations into account (Section 4.3). One can simply identify the known parameters by looking at Figure A.1. In the previous section, the actual four-bar ($ABCD$) dimensions were known with the fixed angle θ_{35} , whereas in this case, the known parameters are the compliant mechanism ($ACFE$) dimensions, the crank link length BD , and the compliant fixed-lock folding angle, θ_{fold} .

Known Parameters: BD , AC , CF , FE , DH , HF , θ_{fold}

Goal: To find the actual four-bar missing dimensions CD , DE , θ_{35} (Figure A.1).

$$\begin{aligned}
 DF &= \sqrt{DH^2 + HF^2} \\
 \alpha &= \arctan\left(\frac{DH}{CF - HF}\right) \\
 \delta &= \arctan\left(\frac{HF}{DH}\right) \\
 \beta &= 90^\circ - \alpha \\
 \gamma &= 90^\circ - \delta \\
 \theta_{36} &= 180^\circ - \beta - \delta \\
 \phi &= 180^\circ - \theta_{fold} - \gamma
 \end{aligned}$$

Using sine and cosine rules in $\triangle DEF$, we have,

$$\frac{DE}{\sin(\phi)} = \frac{FE}{\sin(\theta_{35} + \theta_{36})} = \frac{DF}{\sin(\lambda)}$$

$$DE = \sqrt{DF^2 + FE^2 - 2 \cdot DF \cdot FE \cdot \cos(\phi)}$$

$$\lambda = \arcsin\left(\frac{\sin(\phi)}{DE} \cdot DF\right)$$

$$\theta_{35} = 180^\circ - \phi - \gamma - \theta_{36}$$